Mapping Plasmon Excitations in Gold Nanostructures Using Electron Energy Loss Spectroscopy

Liam Wright

MSci, PGCert

Submitted in fulfilment of the requirements for the

Degree of Doctor of Philosophy

School of Physics and Astronomy

College of Science and Engineering

University of Glasgow

7^{th} September 2020

Lìonar beàrn mhór le clachan beaga

DECLARATION

This thesis has been written by myself and details the research I carried out within the Materials and Condensed Matter Physics group under the supervision of Dr Donald A MacLaren and in the school of Physics and Astronomy at the University of Glasgow from 2016 - 2020. The work described is my own except where otherwise stated. This thesis has not previously been submitted for a higher degree.

DEDICATION

To Mum, Gran, Granda, Josh, and Alison.

In memory of my Dad, James, and my Granny Babs.

ACKNOWLEDGEMENTS

First and foremost I would like to thank my supervisor Dr. Donald MacLaren for his guidance and encouragement throughout my PhD. We have shared some fantastic times during my PhD (not including the 6 am microscope sessions) and it has been an absolute pleasure working with you. Special thanks go to Dr Gary Paterson for all his help, advice, and putting up with some terrible jokes. I would also like to thank Dr Sam McFadzean, Colin How, and Billy Smith for all their training and support during my PhD (and my sincerest apologies for all the breakages and tripped vacuums). Thanks also go to the pub-goers, coffee-drinkers, and all of the members of the MCMP group for playing their part in making my PhD an enjoyable experience.

To my Mum, Brother, Gran, and Granda, I will forever be thankful for your continuous support and words of wisdom throughout my doctorate. There have been some highs and some lows along the road but the encouragement from my family has remained constant,

and I will forever be indebted to you all for it. Special mentions go to Shane "Wee Shaney" McCartan, Trevor "BDT" Almeida, and Jack "Jack" Brennan for the endless amounts of chatting, laughing, and ‘socialising’. We have shared many memorable nights (a few forgettable ones as well) and it was a an honour getting to know you all. Finally I would like to thank Alison Cowan for making my time as a PhD student more enjoyable than I could ever have imagined. From our first limp handshake in the James Watt South to our departure to London to begin our next chapter, I will endlessly be thankful for the joy you bring me in my life.

Sláinte

CONTENTS

LIST OF FIGURES

LIST OF TABLES

ABSTRACT

In this work we present the plasmonic properties of simulated and fabricated Au nanostructures using an electron beam as a source of excitation. The motivation for the this work comes from the applications of these nanostructures and the need to understand the physics behind them. We introduce the concept of plasmonics in chapter 1 where we describe the historical significance and fundamentals underpinning the topic. We provide a description of the conditions under which plasmons can be created and highlight some key concepts which are used throughout this thesis. We then outline the experimental and modelling methodology used to probe the plasmonic properties of our nanostructures in chapter 2. Simulated results are generated using the Metallic NanoParticle Boundary Elemental Method software package, which is capable of calculating the plasmonics of nanostructures using an incident excitation. An overview of the calculations and some initial results regarding substrate effects and size-dependent plasmonics are presented. The

experimental procedure is given in this chapter where we describe the fabrication and examination of our Au nanosturctures. In this work we use electron beam lithography as a method of nanofabrication, a description of which is given. We also show some of the optimisation results whilst highlighting some difficulties with this method. Scanning transmission electron microscopy with electron energy loss spectroscopy is the the experimental technique used throughout this thesis and we provide an overview of this method in Chapter 2, detailing some of the optimisation process and data analysis used in this thesis.

In Chapter 3 we study the plasmonics of near field transducers, motivated by their use in heat-assisted magnetic recording (HAMR) as a nanoscale heat source. This work begins by examining and comparing the plasmonic properties of what we call 'nanoraindrop' and 'nanolollipop' geometries, describing the advantages and disadvantages of each. We then review an annular structure that has more tunable plasmon resonances, both energetically and spatially. Using nanodisk and nanoraindrop geometries, we explore this tuning model by controlling the diameter and position of the hole in the annular structures, showing the potential enhancement of the plasmonic properties of nanostructures.

Chapter 4 explores more complex and realistic environmental factors of temperature and the surrounding dielectric environment in Chapter 4. Understanding the effect annealing has on nanostructures is important for HAMR as they transducer is exposed to fluctuating high temperatures during the recording process. We show the effect of annealing on the plasmonic and structural properties of our fabricated structures and hypothesise the potential problems prolonged heating could cause in HAMR applications.

A realistic dielectric encapsulating layer of Ta_2O_5 is introduced to the simulations and experiment. To investigate our samples and emulate the experimental system in HAMR

we devised and carried out an intricate sample preparation using a focused ion beam. We were able to resolve the plasmonics of the encapsulated nanostructures and compared the results to samples with no encapsulating layer.

Finally, in Chapter 5 we examine a different plasmonic system., moving from the purely 2D structures of ealier chapters to considering out of plane coupling of complex dimple systems found in biosensor used in protein detection. The motivation for this work comes from a need to further understand the detection mechanism of these plasmonic sensors, using simulated electron energy loss spectroscopy. Our examination method for this chapter began with breaking down the complex dimple structures into individual solid and aperture components, and simplifying the geometry from a chiral shape to a rod in order to examine the plasmonic coupling in these devices. We then increase the complexity of the model by examining the shuriken structure, building on our understanding gained from the simple rod results, and highlight the coupling mechanism in our dimple models.

CHAPTER 1

INTRODUCTION & BACKGROUND

1.1 History & Motivation

The use of plasmonics has been around for a long time, although the scientific significance of the subject was not understood until the start of the 20^{th} century. An example is the famed (and late) rose windows of Notre Dame cathedral, Paris, completed between 1225 - 1255. Figure 1.1 shows the north rose window, revealing beautiful and vibrant colours when illuminated by the daylight [4]. The mechanism through which these colours are created exploits gold nanoparticles embedded into the glass when blown. Different sizes of Au nanoparticles generate different colours as light is transmitted through the window. Incident sunlight loses energy as it interacts with the nanoparticles to excite *surface plasmon resonances* (SPRs) with energies that are size-dependent, and the transmitted light through the windows will be different, lustrous colours. The religious and spiritual signif-

icance of these windows will not be explored here, but the science behind them will. In

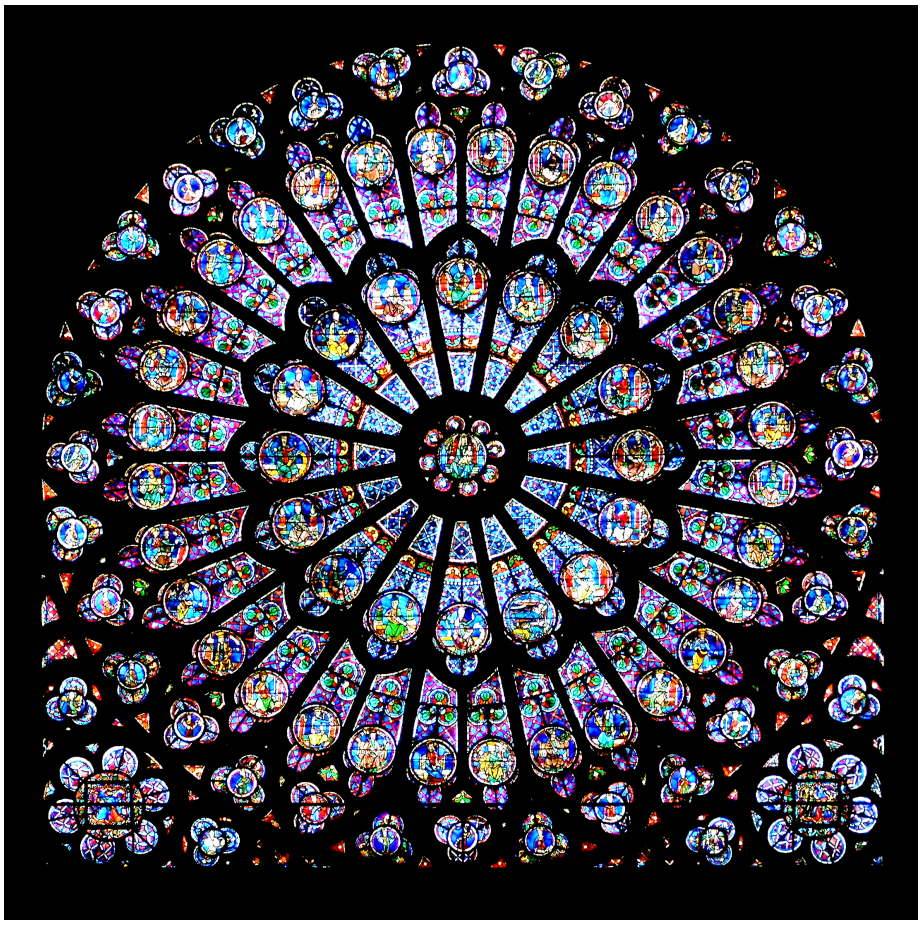

Figure 1.1: *The northern rose window in Notre-Dame, Paris, finished between 1225 and 1255, is a historical example of plasmonics. Colloidal Au was used to generate different coloured glass.*

1902 plasmonic excitations were first documented by Wood when he illuminated a metallic diffraction grating using a polychromatic light source and dark bands were formed in the spectrum of the diffracted light [5], and there was an anomaly in the data. Later, a theoretical formulation of plasmonics was developed by Zenneck and Sommerfield in 1907 as they formed a solution to the experiment using Maxwell's equations of electro-

magnetism [6]. In 1957, Ritchie proposed the idea of surface plasmonics when studying high-losses in thin metallic films [7]. This was verified by Powell and Swan using electron energy loss spectroscopy in 1959 [8,9], which is an experimental technique used to examine the scattering events of an incident electron beam passing through a thin sample (see section 2.4). Transmission electron microscopy married with electron energy loss spectroscopy to this day is seen as a robust method of examination for plasmonics [10,11], and will be the method used throughout this thesis.

In recent years plasmonics has developed into a vibrant research field with a vast number of scientific applications. For example, plasmonics have been applied to molecular identification and biosensing, exploiting the sensitivity of the plasmon resonance energy on the size and geometry of the structures to couple to specific molecular features and allow for the discrimination of bioparticles [12]. Haes and Duyne showcased the sensitivity and selectivity of plasmon resonance biosensors using Ag nanotriangle arrays [13] to detect streptavidin protein. This is made possible due to a biotin monolayer fabricated onto the surface of Ag nanostructures which exhibit redshifts in plasmon resonance energy when the biotin layer bonds with streptavidin. In more recent work, Tullius *et al.* tested the capabilities of chiral plasmonic sensors in detecting supermolecular structures [14]; this is explored further in chapter 5. Plasmonics has also been applied to photovoltaics, where far greater currents are capable of being generated using plasmonic nanostructures in solar cell devices [15,16]. One such plasmon enhanced solar cell works by embedding metallic nanoparticles in a semiconducting material which, when exposed to light, creates more electron-hole pairs due to the evanescent electric field generated by the plasmon resonances, a description of which is given in section 1.2. Here we focus our attention to the

near-field transducer capabilities of plasmonics devices, and the ability to generate intense electric fields well below the diffraction limit. This is of particular interest to the field of magnetic storage and the proposed *heat assisted magnetic recording* devices.

1.1.1 Heat Assisted Magnetic Recording & Near Field Transducer Applications

The main motivation for chapters 3 and 4 presented in this thesis is an emerging technology in magnetic recording data storage devices: heat-assisted magnetic recording (HAMR). The International Data Corporation predicts that by 2025 we will generate 163 zettabytes of data, a substantial increase over the 33 zettabyes generated in 2018 [17]. This shows a clear need for more data storage but the work-horse of today's data storage, the hard disk drive, is already at the limit of data storage density. Conventional magnetic recording devices are reaching their physical capacity whilst still being functional. These devices work by encoding data as the direction of the magnetic moment in a region of granular ferromagnetic thin film. Early versions of these devices used in-plane magnetisation, however modern devices use out-of-plane magnetisation, the direction of which we will call 'up' and 'down' [18], as it leads to an increase in bit density. In current HDD technologies, each data storage bit spans several crystalline grains within a polycrystalline continuous film, forming an isolated magnetic domain. A typical approach to increasing data storage density has simply been to reduce the bit size, reducing the number of crystal grains per bit, however a fundamental limit is set by the superparamagnetic limit. This is a phenomenon found in small ferromagnetic materials (such as our data storage bits) where the magnetisation can randomly flip direction due to temperature fluctuations [19]. This in

turn makes the recording material highly unstable and completely unreliable as a storage device. In order to overcome this issue, and to increase the storage capabilities of HDDs, new magnetic materials (such as FePt [20]) with inherently smaller grains and a smaller superparamagnetic limit must be used. However, due to the small grain size of the proposed material, the recording material has a high anisotropy [21], i.e. a preferred direction of magnetisation due to the crystallographic structure of the material. To overcome this, a high magnetic field is required during data writing to flip the direction of magnetisation. The magnetic field strength needed to reduce the magnetisation of a ferromagnet (in the case of HAMR, this is the data bit) to zero is known as coercivity. However, the coercivity for the proposed high anisotropy magnetic recording materials is larger than the magnetic field capable of being generated by the magnetic recording pole of the storage device. In order to resolve this problem, localised heating can be carried out which will reduce the coercivity of the heated region and allow the magnetisation to be flipped. Optical methods of heating (direct laser light) would not be suffice due to the size of area requiring heat as it is well below the diffraction limit [20]- bit size is less than 50nm [21]. A viable solution to this problem is to use plasmonic nanoantenna as a heat source due to the inherent ability to focus light down well below the diffraction limit.

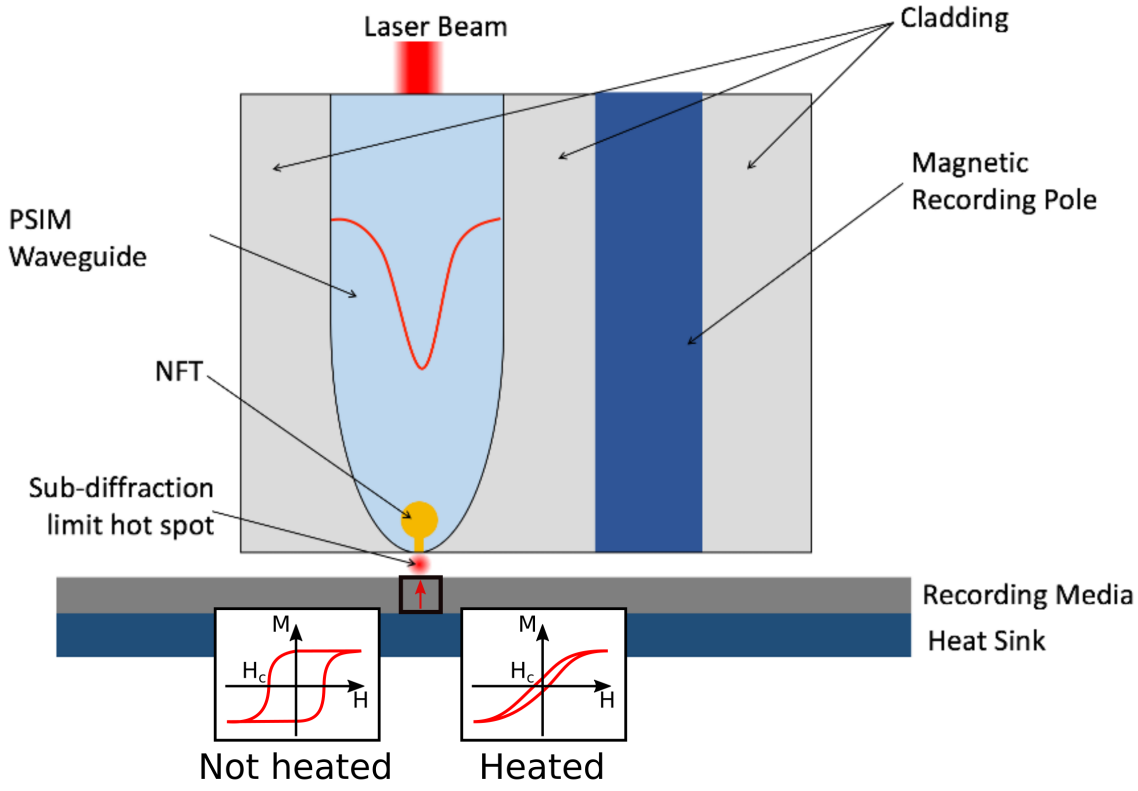

Figure 1.2: *A schematic of a typical heat assisted magnetic recording device. A planar solar immersion waveguide is used to focus laser light onto a near-field transducer (NFT). A surface plasmon resonance is generated in the transducer, emitting an exponentially decaying electric field hot spot, which heats a sub-diffraction limit area on the recording media. This then reduces the coercivity of the magnetic material, allowing for the magnetisation to be easily flipped by the recording pole as shown in the hysteresis loops for both heated and non-heated modes.*

Figure 1.2 shows a schematic of a typical heating system in a HAMR device. Laser light is guided towards a near-field transducer (NFT) using a planar solar immersion waveguide - a parabolic-shaped waveguide with a numerical aperture (NA) value greater than one, and focuses light onto the NFT [20]. The laser light then excites a SPR in the NFT, emitting an exponentially decaying electric field onto the recording medium and

heats the spot size through radiative heating to reduce the coercivity of the medium. This is illustrated in the inset to figure 1.2, where the hysteresis loop for the magnetic bit for both heated and not heated are given. These hysteresis loops show that the coercive field H_C is reduced as the bit is heated from the NFT, allowing for the magnetic recording pole to now flip the magnetisation of the bit. A description of the heating process is laid out in section 1.2. This has a massive advantage over laser heating as the hot spot size in figure 1.2 is determined by the geometry and size of the NFT. As one can imagine, this solution to increasing data storage space would have a large variation in approach by the manufacturers. Geometric effects on the plasmonics of NFTs are explored in chapter 3, where we examine a number of proposed structures.

1.2 Surface Plasmon Polaritons

Much of the theoretical development of plasmonics is eased by considering a plasmon as discrete entity. A plasmon can be considered as a pseudo-particle consisting of oscillating electrons in a conductive material. In an isolated metallic object, such as a Au nanoparticle or the NFTs proposed for HAMR, delocalised outer electrons are constrained by the object's geometric boundaries as they respond to the electric field of incident radiation. It is useful to consider two types of plasmon excitations: bulk and surface plasmons. Bulk plasmons are excitations within the body of the material and resonate at energies defined by material properties including conduction electron densities [22] (roughly $5-30$eV). Surface plasmon polaritons (SPP) are discrete eigenfunction oscillations defined by the boundary conditions imposed by the particle's size and shape. The resonance energies

of SPPs are lower than that of bulk plasmons (roughly $0.6-5$eV), and are easily distinguished in experiment. By defining boundary conditions between a metal and a dielectric, and using these to solve Maxwell's equations, we find that the electric field decays exponentially perpendicular to the interface to produce an evanescent field. Materials in close proximity to the resonances experience this intense field and allows a plasmonic structure to be used in applications like HAMR, where localised heating is required.

In order to understand the conditions for SPP generation, we first derive the general conditions for resonances of an electromagnetic wave in a waveguide. We begin with Maxwell's equations of electromagnetism, given by

$$\nabla \cdot \mathbf{D} = \rho_{ext}, \tag{1.1}$$

$$\nabla \cdot \mathbf{B} = 0, \tag{1.2}$$

$$\nabla \times \mathbf{E} = -\frac{\partial \mathbf{B}}{\partial t}, \tag{1.3}$$

$$\nabla \times \mathbf{H} = \mathbf{J}_{ext} + \frac{\partial \mathbf{D}}{\partial t}, \tag{1.4}$$

where $\mathbf{D}$ and $\mathbf{E}$ are the dielectric displacement and electric field respectively, $\mathbf{H}$ is the magnetic field, and $\mathbf{B}$ is the magnetic flux density. The external charge and current density are given by ρ_{ext} and $\mathbf{J}_{ext}$ but for now we will assume no external excitation, i.e. ρ_{ext} and $\mathbf{J}_{ext} = 0$. We also have used $\mathbf{B} = \mu_o \mu \mathbf{H}$ whilst assuming that the medium is non-magnetic and we set $\mu = 1$. Firstly, we combine equations 1.3 and 1.4 to obtain the expression

$$\nabla \times \nabla \times \mathbf{E} = -\frac{\partial^2 \mathbf{D}}{\partial t^2}. \tag{1.5}$$

Next, we use the vector identities $\nabla \times \nabla \times \mathbf{C} = \nabla(\nabla \cdot \mathbf{C}) - \nabla^2\mathbf{C}$ and $\nabla \cdot (\alpha\mathbf{C}) = \mathbf{C} \cdot \nabla\alpha + \alpha\nabla \cdot \mathbf{C}$ to obtain

$$\nabla\left(\frac{1}{\varepsilon}\mathbf{E} \cdot \nabla\varepsilon\right) - \nabla^2\mathbf{E} = -\mu_o\varepsilon_o\varepsilon\frac{\partial^2\mathbf{E}}{\partial t^2}. \tag{1.6}$$

We simplify this by assuming that the dielectric function is homogeneous in the medium, such that $\nabla\varepsilon = 0$. We also use the relationship $c^2 = 1/\sqrt{\varepsilon_o\mu_o}$ to obtain

$$\nabla^2\mathbf{E} - \frac{\varepsilon}{c^2}\frac{\partial^2\mathbf{E}}{\partial t^2} = 0. \tag{1.7}$$

which is the electromagnetic wave equation written in terms of the electric field. Before progressing further it is worthwhile defining the dielectric function. This describes the electronic interaction between a medium and an incident electromagnetic wave, and is a function of angular frequency, ω. The dielectric function is a complex function, given by $\varepsilon(\omega) = \eta_1 + i\eta_2$ where the real and imaginary parts relate to the refractive index, n, and extinction coefficient, k_e, by $\eta_1 = n^2 - k_e^2$ and $\eta_2 = 2nk_e$. This is the definition of the complex dielectric function used throughout this thesis [23]. Continuing with the derivation,we use a harmonic time-dependent solution, $\mathbf{E}(\mathbf{r},t) = \mathbf{E}(\mathbf{r})e^{-i\omega t}$ which gives

$$\nabla^2\mathbf{E} + k_o^2\mathbf{E} = 0, \tag{1.8}$$

where $k_o = \omega/c$ is the propagating wave vector in a vacuum. Equation 1.8 is known as the Helmholtz equation and will be the basis from which we will derive the conditions for plasmon generation. We continue this derivation by defining a propagation direction of a wave at the interface between two media, shown in figure 1.3. Consider an interface lying

at $z = 0$ (of a large surface where we define large to be much greater than the wavelength of incident radiation), and take the propagation to be solely in the x-direction. We assume this is a one-dimensional problem with no spatial variation in the $y-$direction and the dielectric dependency is purely in the z, i.e. $\varepsilon = \varepsilon(z)$. The propagating wave at the interface is defined as $\mathbf{E} = \mathbf{E}(z)e^{i\beta x}$, where β is the propagation constant [22]. Applying this to equation 1.8 we obtain

$$\frac{\partial^2 \mathbf{E}(z)}{\partial z^2} + \left(k_o^2 + \beta^2\right)\mathbf{E} = 0. \tag{1.9}$$

The next step is to write the explicit vector forms of equations 1.3 and 1.4, and using the harmonic time dependence we obtain

$$\begin{bmatrix} \frac{\partial E_z}{\partial y} - \frac{\partial E_y}{\partial z} \\ \frac{\partial E_x}{\partial z} - \frac{\partial E_z}{\partial x} \\ \frac{\partial E_y}{\partial x} - \frac{\partial E_x}{\partial y} \end{bmatrix} = i\mu_o\omega \begin{bmatrix} H_x \\ H_y \\ H_z \end{bmatrix}, \tag{1.10}$$

$$\begin{bmatrix} \frac{\partial H_z}{\partial y} - \frac{\partial H_y}{\partial z} \\ \frac{\partial H_x}{\partial z} - \frac{\partial H_z}{\partial x} \\ \frac{\partial H_y}{\partial x} - \frac{\partial H_x}{\partial y} \end{bmatrix} = -i\varepsilon_o\varepsilon\omega \begin{bmatrix} Ex \\ Ey \\ Ez \end{bmatrix}. \tag{1.11}$$

We now consider the transverse magnetic (TM) modes in the case where there is no magnetic field in the propagation direction, and only H_y, E_x and E_z components are non-

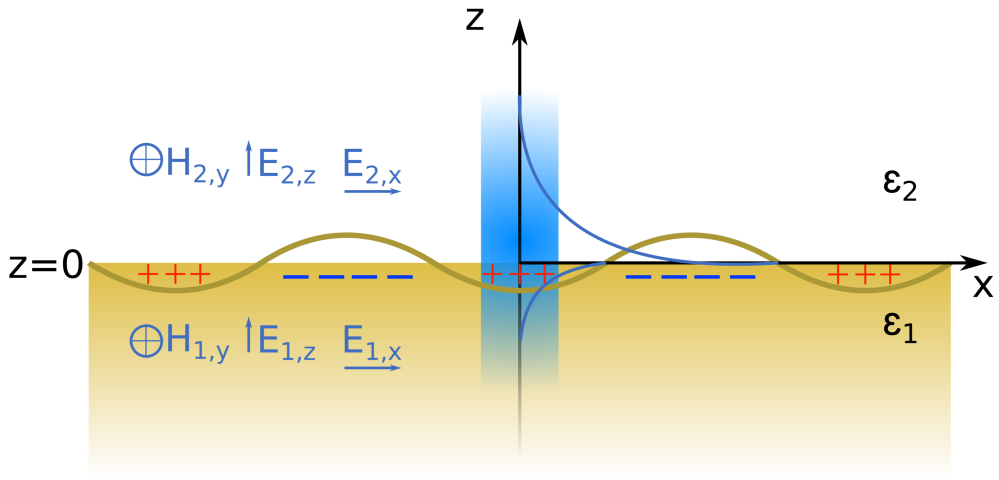

Figure 1.3: *Solutions to Maxwell's equations between the boundary of a dielectric and a metal. There is an evanescent electric field decaying exponentially in the z direction, perpendicular to the surface. Polarisation of surface charge is generated in the x-axis due to the constant propagation of the electric field in this direction.*

zero, as illustrated by figure 1.3. Using these conditions in equation 1.10 we arrive at

$$E_x = -\frac{i}{\omega\varepsilon\varepsilon_o}\frac{\partial H_y}{\partial z}, \tag{1.12}$$

$$E_z = -\frac{\beta}{\omega\varepsilon\varepsilon_o}H_y. \tag{1.13}$$

Applying these to equation 1.11 we obtain

$$\frac{\partial^2 H_y}{\partial z^2} + \left(k_o^2 - \beta^2\right)H_y = 0. \tag{1.14}$$

This is the wave equation for TM modes. In this work we will only present the TM mode solutions, reasons for which are given below.

To continue with the derivation we now specify the conditions for a boundary between two dielectric media characterised by dielectric functions ε_1 and ε_2, and the interface lies at $z = 0$, as shown in figure 1.3. We assign the region $z > 0$ with a positive dielectric constant ε_2, and $z < 0$ with a complex dielectric function ε_1. We assign an exponentially decaying field in the z-direction and a continuous propagation in the x-direction as before. The solution for the medium ε_2 is

$$H_{2,y}(z) = e^{i\beta x}e^{-k_2 z}, \tag{1.15}$$

$$E_{2,x}(z) = -\frac{i}{\omega\varepsilon_o\varepsilon_2}e^{i\beta x}e^{-k_2 z}, \tag{1.16}$$

$$E_{2,z}(z) = -\frac{\beta}{\omega\varepsilon_o\varepsilon}e^{i\beta x}e^{-k_2 z}, \tag{1.17}$$

where E_x, and E_z are derived from equations 1.12 and 1.13 respectively. In the medium

ε_1, for $z < 0$, we derive

$$H_{1,y}(z) = e^{i\beta x} e^{-k_1 z}, \tag{1.18}$$

$$E_{1,x}(z) = \frac{i}{\omega \varepsilon_o \varepsilon_1} e^{i\beta x} e^{-k_1 z}, \tag{1.19}$$

$$E_{1,z}(z) = -\frac{\beta}{\omega \varepsilon_o \varepsilon_1} e^{i\beta x} e^{-k_1 z} \tag{1.20}$$

in the same manner. For continuity at the interface some boundary conditions must be met. At the interface, $z = 0$, we constrain the electric and magnetic field components by setting $H_{1,y} = H_{2,y}$ and $\varepsilon_1 E_{1,z} = \varepsilon_2 E_{2,z}$. This leads to the condition that

$$\frac{k_2}{k_1} = -\frac{\varepsilon_2}{\varepsilon_1}. \tag{1.21}$$

This defines the conditions with which a surface plasmon can be generated. Equation 1.21 requires that the real part of ε_1 is less than 0 if the value of ε_2 is positive, i.e. ε_1 and ε_2 are a metal and insulator respectively. The work presented in this thesis will examine plasmons generated at the interface of gold-vacuum (vacuum dielectric constant of $\varepsilon = 1$) and gold-Si_3N_4 substrate ($\varepsilon = 4.05$ [24]). We can then apply equation 1.15 into the TM wave equation 1.14 for both media we obtain

$$k_1^2 = \beta^2 - k_o^2 \varepsilon_1, \tag{1.22}$$

$$k_2^2 = \beta^2 - k_o^2 \varepsilon_2, \tag{1.23}$$

which, when combined with equation 1.21 gives

$$\beta = k_o \sqrt{\frac{2\varepsilon_1 \varepsilon_2}{\varepsilon_1 + \varepsilon_2}}. \tag{1.24}$$

This is the dispersion relation for a propagating surface plasmon at the interface of two media. The above derivation was carried out for the TM modes of a large, 1D system with no external excitation, resulting in a purely material-based solution where β depends only on ε_1 and ε_2. A similar derivation can be carried out for the transverse electric (TE) modes, not shown here, and would produce a non-physical condition that implies that SPP generation is only possible for TM modes [22]. SPPs can also be created by exposing a metal to an electron beam in a transmission electron microscope [25–28]. When a fast moving electron in the beam passes through the material the conduction electrons are displaced due to Coulombic repulsion. This then leaves a transient positive 'hole' in the wake of the incoming electron [10]. The conduction electrons response to the perturbation is oscillatory, creating regions of differing positive and negative charges. This is discussed in section 2.1 where we describe the methodology of exciting and examining the plasmons generated within our nanostructures.

1.2.1 Localised Surface Plasmon Resonance

We have discussed surface plasmon generation for a large surface (large is defined as the sample size being much greater than the wavelength of the excitation). However, for the work presented throughout this thesis, the dimensionality of the illuminated specimen is of the order of the penetration depth of the incident electromagnetic wave [22, 29]. A

simple schematic is shown in figure 1.4, depicting the interaction between a nanoparticle and an electric field. The delocalised electrons respond to the electric field to polarise the particle. As the incident field oscillates, it creates a bound oscillatory response within the particle [30], known as localised surface plasmon resonance (LSPR). The wavelength of such an excitation is much smaller than that of an electromagnetic field (details given in section 2.3), and will also produce higher order resonance modes within the structure [10]. Throughout this thesis we will refer to the dipole mode, as it can be excited using electromagnetic radiation. Higher order modes for a nanosphere shown in figure 1.4 include quadrupole, hexapole etc resonances, details of which are given in section 2.1. These are referred to as dark modes as they cannot be easily excited through electromagnetic radiation. Derivations of LSPRs for a perfectly spherical nanoparticle are carried out in [22], where a quasi-static approximation solution is employed. The results showed that the plasmon resonances of the perfectly spherical structure are dependent on the cubed radius of the sphere, which is a significant factor and an important result. The solution cannot be solved analytically for more complex geometries, so a numerical solution is required (for our work this is carried out using the software package described in section 2.1). This work shows a direct dependence of the plasmon resonance with the size of the particle, and is a feature utilised in tuning the properties to tailor the structure for a certain application, such as HAMR (discussed in chapter 3) or biosensing (discussed in chapter 5). This is explored further in chapters 2 and 3.

Another, more complex, feature that defines the resonance energy of the bright and dark modes of a nanostructure is the geometry and shape of the particle. The exploration of geometries to suit a particular purpose is very well documented. For instance chiral

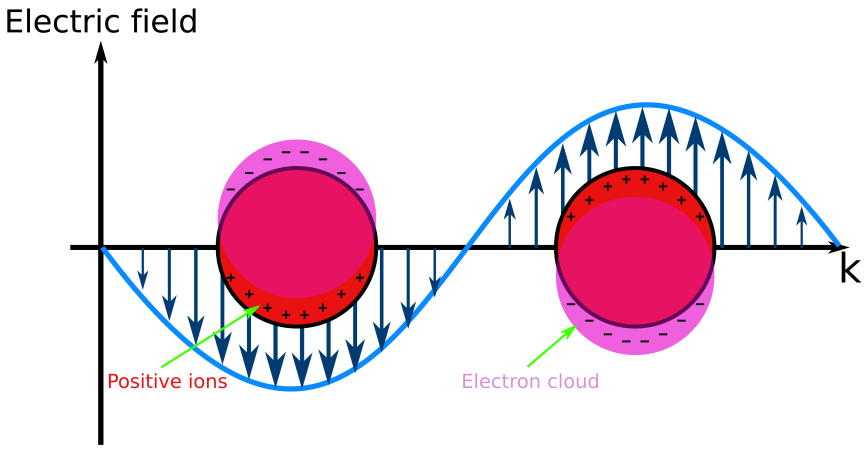

Figure 1.4: *Schematic of the delocalised electron cloud established in an isolated metallic nanoparticle, in response to an oscillating electric field, caused by Coulomb repulsion. The particle is smaller than the excitation wavelength creating a non-propagating standing wave, known as a localised surface plasmon resonance.*

geometries are employed for protein detection due to the circular polarisation of the structure and the molecule it is trying to detect [31]. Even with the advancement of focused electron beam induced deposition, 3D plasmonic structures are being fabricated with relative ease [32]. Geometric effects will be explored further in chapters 3 and 5. These resonances are also not perpetual, but damped due to a number of mechanisms which are explored further in chapter 4.

1.2.2 Hybridisation

Hybridisation is a concept mentioned throughout this thesis, particularly in chapter 5 where it is discussed in reference to chiral plasmonic structures. This is a mechanism for the coupling of local surface plasmon polaritons in adjacent structures first prosed by Prodan [1] who assessed the plasmonic coupling between the dipolar modes of a nanosphere

and a circular aperture of the same diameter as the sphere. Prodan showed that there are two factors dictating hybridisation within a model: charge distribution symmetry and resonance energy matching. This work has been used extensively throughout the field as it is a simple and insightful model for understanding electrostatic coupling and tuneability of plasmonic systems. A schematic showing the proposed model is shown figure 1.5 were we have depicted the dipolar coupling between two nanodisks. This energy diagram depicts the multiple ways in which two adjacent nanoparticles can couple. First, coaxial dipoles can be established with charge distributions that combine in low energy bonding mode and high energy anti-bonding mode, as illustrated. The bonding mode is stabilised by a positive region adjacent to a negative region in the other particle. The anti-bonding mode has two adjacent positive regions side-by-side which accounts for the higher resonance energy. Secondly, the perpendicular dipole modes couple in a similar manner to the coaxial dipoles. The higher energy system have the same charge distributions aligned in parallel whilst the lower energy system has the polarisation flipped dipole mode.

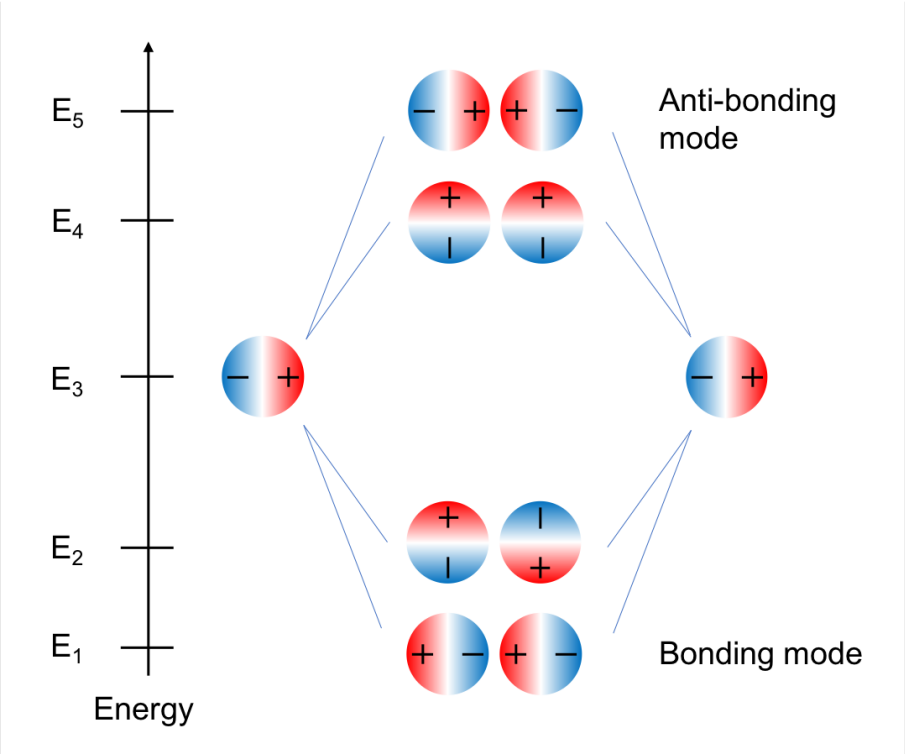

Figure 1.5: *Energy diagram showing the hybridisation model proposed by Prodan [1]. Coupling between two nanodisks produces bonding and anti-bonding modes as well as two non-degenerate perpendicular dipoles.*

The model shown in figure 1.5 is simplified, and shows the response for a highly symmetric, perfect system. In reality, fabricated structures will have imperfections and are very rarely perfectly symmetric. The nature of this model is dependent on the proximity of the structures as well, which is explored in reference [33]. Recent work has applied this model to 3D systems, where out of plane hybridisation has been observed for layered structures [34]. Hybridised systems are examined in chapter 5 where we study the out of plane hybridisation of solid-aperture systems, illustrating the detection mechanism found in chiral biosensors [14].

1.3 Thesis Outline

The main aim of this thesis is to examine the plasmonic properties of Au nanostructures using simulated and experimental techniques in order to understand the geometric and environmental effects on the NFTs plasmonics. In order to meet this we need to explore a number of distinct aspects of research. First, a number of developments were required in fabrication and building simulation models of NFTs, and they are outlined in chapter 2, where we describe the examinations methods used throughout this thesis.

Chapter 3 then focuses on examining a number of NFT geometries in order to spatially and energetically resolve plasmon modes for viable designs. We begin by presenting the plasmonic properties of two possible NFT geometries for HAMR applications, which extends the current understanding of such nanostructures in the field. The next piece of work explored annular NFT geometries as a simple but effective method of energetic tuning and accentuation of the plasmon resonances. This work was inspired by split-ring resonator experiments and theoretical crescent geometry plasmomnics [35] but we have shown this to also be a viable a nanofocusing and tuning method; advancing the state of the art in NFT geometry.

The complexity of the experimental system is increased in chapter 4 by adding a number of practical considerations including encapsulating the NFTs in a dielectric material and studying the effect of annealing on the nanostructures. The former was carried out using a novel experimental technique in which plasmon resonances were mapped for a number of NFTs encapsulated in $Ta_2O_5$and we present the dielectric effect on plasmonics. The latter showed the effect fluctuating temperatures has on the structural and plasmonic properties of NFTs and how this could hamper the coupling efficiency for the nanostruc-

ture in a HAMR device. Finally, in chapter 5 we examine dimple plasmonic structures in order to explore the hybridisation and coupling in such systems. The motivation for this work comes from the need to understand the protein identification mechanism in chiral biodetectors [14]. We carry out this study by creating a number of isolated and coupled systems consisting of solid and aperture structures to inspect the possible hybridisation is the combined models.

CHAPTER 2

METHODOLOGY

In this chapter we will give an overview of the equipment, modelling and processing used throughout this work. It will cover instrumentation including aspects of the acquisition of electron energy loss spectroscopy datasets using scanning transmission electron microscopy, the fabrication of gold nanostructures and the complementary simulations used to analyse the results. The simulation package used here was a toolbox for MATLAB which allows us to simulate the plasmonic response of metallic nanoparticle to an external stimulus such as an incoming fast electron (as in the case of EELS) or EM radiation (as in the case of HAMR technology). This software provides a wealth of information that builds the landscape for us to explore experimentally. In Chapter 3, these simulations are used to determine the trends in spectral features as a function of NFT geometry, so that experimental data collected from a small number of real devices can be interpreted. Fabrication of these NFTs was carried out using electron beam lithography, which has the

capability to create structures with dimensions in the scale of 10 nm [36]. Transmission electron microscopy, both conventional and scanning, was the chosen method to examine these plasmonic nanoelements because it offers superior spatial resolution in comparison to optical characteristics and thereby enables direct correlation of a particle's structure to its plasmonic functionality. This technique enables us to understand the effects of features such as imperfect fabrication and granularity on a plasmon spectrum [11, 25]. The particular characterisation technique used throughout this work is electron energy loss spectroscopy, which is used to acquire a vast amount of information about the specimen including characterisation of composition, phonon scattering, and surface plasmon generation [11], which is the focus of this work.

2.1 MNPBEM Simulations

The Metallic NanoParticle Boundary Elemental Method (MNPBEM) is a toolbox available for MATLAB which is capable of simulating the plasmonic response of metallic nanoparticles using the boundary elemental method [37, 38]. This is performed by solving Maxwell's equations over boundaries between two media defined by their dielectric properties, as described in chapter 1. The surface or interface boundary is triangulated and the electromagnetic properties are evaluated at the centre of each triangular face [39]. The particle and environment are assigned with appropriate dielectric functions over which Maxwell's equations are solved, and the plasmonic response is calculated. In order to solve Maxwell's equations (given in section 1.2) we first write them in terms of scalar and

vector potentials A and ϕ which relate to **E** and **B** by

$$\mathbf{E} = ik\mathbf{A} - \nabla\phi \tag{2.1}$$

and

$$\mathbf{B} = \nabla \times \mathbf{A}, \tag{2.2}$$

where **E** and **B** are the electric and magnetic fields respectively and k is the wavenumber (defined as $k = \omega/c$ for the angular frequency ω and speed of light in vacuum c); i is the imaginary unit. **A** and ϕ are related by the Lorentz Guage condition, $\nabla \cdot \mathbf{A} = ik\varepsilon\phi$; the magnetic permeability is assumed to be $\mu_r = 1$. For the Helmholtz equation (equation 1.8 in section 1.2) we introduce the Green function, giving

$$(\nabla^2 + k_j^2)G_j = 4\pi\delta(\mathbf{s}) \tag{2.3}$$

with $k_j = k\sqrt{\varepsilon_j}$ being the wavenumber in the medium j and **s** is a point on the boundary between the two media. Solution to the Helmholtz equation is given as

$$G_j(\mathbf{s} - \mathbf{s'}) = \frac{e^{ik_j|\mathbf{s}-\mathbf{s'}|}}{|\mathbf{s}-\mathbf{s'}|}, \tag{2.4}$$

where **s** and **s'** are points on the boundary over which the calculation is being carried out. This is shown in figure 2.1 where the interaction between both points **s** and **s'** (the centre of the triangular mesh faces) is described by G_1, where the boundary calculations are taken between the media ε_1 and ε_2. The normal vector n_s is chosen to be directed towards

medium 1 (ε_1). The scalar and vector potentials can be written as

$$\begin{aligned} \phi_j(\mathbf{s}) &= \phi_j^{ext} + \int_\Omega G_j(\mathbf{s}\text{ - }\mathbf{r})\sigma_j(\mathbf{r})da \\ \mathbf{A}_j(\mathbf{s}) &= \mathbf{A}_j^{ext} + \int_\Omega G_j(\mathbf{s}\text{ - }\mathbf{r})\mathbf{h}_j(\mathbf{r})da, \end{aligned} \tag{2.5}$$

where ϕ_j^{ext} and $\mathbf{A}_j^{ext}$ are the scalar and vector potentials defining the external excitation (the electron beam in the case of EELS) within medium j, and $\mathbf{r}$ is a point in medium j. Ω refers to the boundary of the media. σ_j and $\mathbf{h}_j$ are the surface charge and current distributions that meet the boundary conditions of Maxwell's equations between two dielectric media and define the plasmon resonance [22]. A schematic of a triangulated boundary over which the calculations are carried out is given in figure 2.1. The MNPBEM toolbox can calculate the plasmonic response to either an optical or electron beam excitation [39] however, for the majority of the work presented here, an incident electron beam is used as a source of excitation [37]. The energy lost by a fast moving electron, with velocity $\mathbf{v}$, charge e and trajectory $\mathbf{r}_e(t)$, can be calculated from the work done on the electric field induced on the particle by the external field, E_{ind}, given by

$$\Delta E = e\int \mathbf{v}\cdot\mathbf{E}_{ind}[\mathbf{r}_e(t),t]dt, \tag{2.6}$$

$$= \int_0^\infty \hbar\omega\Gamma_{EELS}(\mathbf{S},\omega)d\omega, \tag{2.7}$$

where $\Gamma_{EELS}(\mathbf{S},\omega)$ is the loss probability and $\mathbf{S}$ denotes the electron impact point on the boundary. Our definition of the loss probability is taken from references [10, 37] where a

full derivation can be found. This is defined as

$$\Gamma_{EELS}(\mathbf{S},\omega) = -\frac{e}{\pi\hbar\omega}\sum_j \Im m\left[\oint_\Omega \varphi(\mathbf{r})\left\{k\mathbf{v}\cdot\mathbf{h}_j(\mathbf{r}) - qv\sigma_j(\mathbf{r})\right\}da\right]d\omega, \tag{2.8}$$

where e and $\mathbf{v}$ are the electron charge and velocity respectively, and $\mathbf{v} = v\hat{\mathbf{z}}$. The wavenumber, q, is given as $q = \omega/|\mathbf{v}|$, and $\varphi(\mathbf{r})$ is a potential term associated with the electron propagation inside a medium [10]. This is a complex integral over the boundary Ω_j but offers a computationally more efficient method of calculating the loss probability compared to other methods (including a direct calculation of the induced electric field [40]). Equation 2.8 relies on the readily available surface charge, σ_j, and current distribution, $\mathbf{h}_j$, to calculate Γ_{EELS} from an incident electron rather than the induced field along the full electron trajectory [38]. As shown in figure 2.1, the nanoparticles used in the calculations have discretized surfaces using (typically) a triangular mesh. Therefore the loss probability calculation is carried out for individual boundary elements which are in the path of the electron beam trajectory. MNPBEM allows the user to input the electron trajectory and beam width to form a more realistic simulation, making the output more comparable to complimentary experimental work. The trajectory of the electron beam is assumed to be unaltered and follows a straight line in the defined path direction. The electron beam width is set so that it best emulates the spot size of the electron microscope [38], see section 2.3 for details.

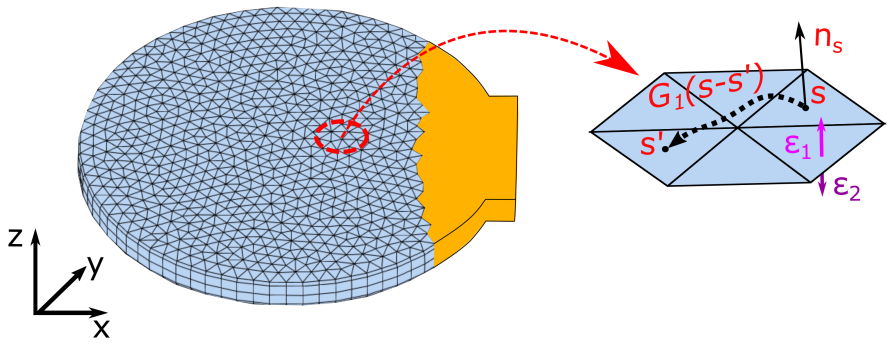

Figure 2.1: *Discretised nanolollipop surface with nodal density to balance accuracy and computational time. Each centre point in the triangulated surface is connected via the Green function given in equation 2.4.*

Another important feature available in the MNPBEM software is the ability to calculate the charge distributions of a nanostructure by considering the perturbation of the electronic state of a nanoparticle caused by an incident electron source [41]. Simulated charge distributions offer great insight into the plasmon modes generated within a nanostructure, and helps to inform the results of the energy loss calculations. Here we highlight the derivations shown in reference [42] where the full plasmonic eigenmode expansion is presented. We can rewrite the scalar potential in equation 2.5 as

$$\Lambda(\omega)\sigma(\mathbf{s}) + \int_{\Omega} F_j(\mathbf{s}\text{ - }\mathbf{r})\sigma_j(\mathbf{r})da = -\frac{\partial \phi_j^{ext}}{\partial n_s}, \tag{2.9}$$

where $F_j(\mathbf{s}\text{ - }\mathbf{r})$ is the surface derivative of the Green's function given in equation 2.4 and

$$\Lambda(\omega) = \frac{\varepsilon_2(\omega) + \varepsilon_1(\omega)}{\varepsilon_2(\omega) - \varepsilon_1(\omega)}. \tag{2.10}$$

The left hand side of equation 2.9 is purely nanostructure-dependent (geometry and di-

electric properties [29,42]), from which we can define the charge distribution eigenmodes modes as

$$\int_{\Omega} F(\mathbf{s}\text{ - }\mathbf{r})\sigma_k(\mathbf{r})da = \lambda_k\sigma_k(\mathbf{s}), \tag{2.11}$$

where λ_k is the k^{th} eigenvalue and σ_k is the corresponding eigenvector. MNPBEM allows us to the calculate and map the eigenmode charge distributions, σ_k, of a defined nanostructure with assigned dielectric properties which aids us in understanding the plasmonic properties revealed by the electron energy loss simulations. Figure 2.2(a) shows an example of the calculated surface charge distribution of a dipole mode for a nanorod (dimensions of 300 x 40nm and thickness of 25nm) using the eigenmode calculation. The charge distribution is normalised between -1 and 1 (blue to red) which is consistent throughout this thesis. The absolute charge distribution values are available to the user in MNPBEM, however here we are normalising between -1 and 1 to make a qualitative comparison, and quantitatively comparing the energy of the modes. It is clear to see the dipole nature of this charge distribution and highlights the usefulness of understanding the plasmon modes of a structure. We can also map the surface charge distribution of the nanostructure in response to the incident electron beam in the MNPBEM toolbox. Figure 2.2(b) shows the charge distributions of the dipole mode calculated using the incident electron excitation (trajectory shown in pink). This is highly localised charge distribution caused by the electron beam and can be difficult to interpret. The majority of the work presented in this thesis will use charge distributions calculated using the eigenmode expansion shown in figure 2.2(a) however, we examine the charge distributions caused by the electron beam in chapter 5 as we analysed the localised coupling between two particles. Combining the electron energy loss spectroscopy calculations with the charge distributions allowed us

to fully examine the plasmonic properties of the nanostructures studied throughout this thesis.

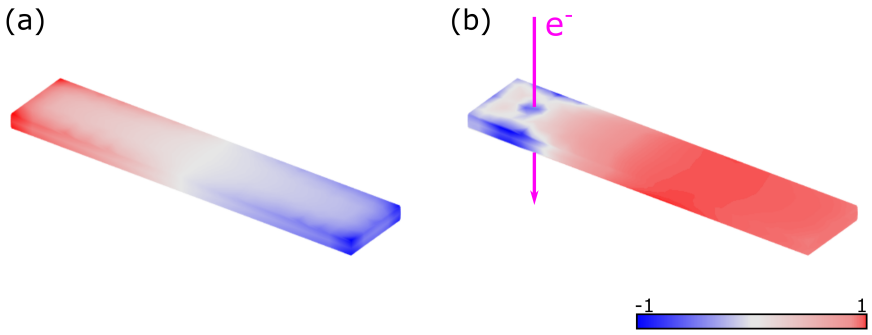

Figure 2.2: *(a) Charge distribution eigenmode for a thin nanorod geometry. (b) Highly localised charge distribution created by the electron beam passing through the sample (trajectory shown in pink).*

After the simulation model is set and a particle has been created with an assigned dielectric function we can simulate the plasmonic response to a fast moving electron. This allows us to make comparisons between the simulated model described above and the experimental results obtained from EELS data [41]. An assumption made within the model is that the dielectric function is homogeneous throughout the particle, which is a simplification when compared to the experimental work as the dielectric properties of a sample will vary in real samples (grain boundary effects for example, see chapter 4) [43]. We build our experimental model by setting a number of electron beam impact points across the particle which allows us to examine a multitude of plasmon modes excited at different parts of the geometry. In figure 2.3(a) we show the resulting electron energy loss spectra for a gold nanodisk with a diameter of 300nm, thickness 25nm with the electron trajectories towards the particle shown as an insert.

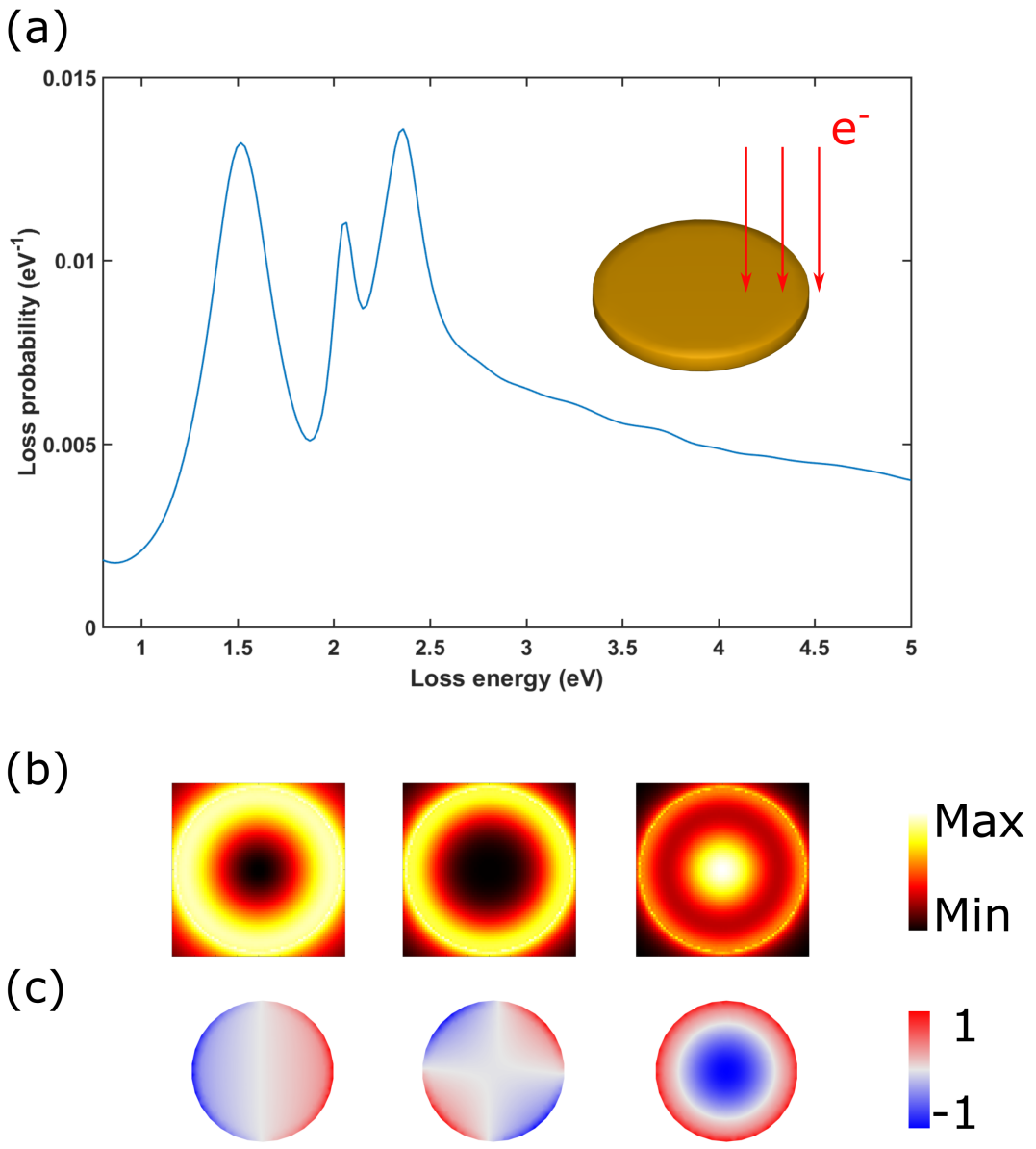

Figure 2.3: *(a) Simulated energy loss spectrum with (b) corresponding energy loss maps and (c) charge distribution eigenmodes for a gold nanodisk of diameter 300 nm and thickness 25 nm, a schematic of which is shown as inset in (a) with three individual incident electron trajectories. There are a number of observable excitations which are the plasmon resonances of the particle associated with the eigenmodes illustrated. The spectrum is obtained by summing the individual responses from the given trajectories.*

In the spectrum of figure 2.3(a) the individual peaks represent a plasmon resonance mode. Each impact point on the particle is used to calculate a spectrum and here we have summed each spectra in order to illustrate the overall spectral response of the particle, revealing which resonance modes are dominant. We select impact points based on the nanostructures geometry, ensuring that we excite as many modes as possible throughout the geometry. Each peak represents either a mode or a superposition of degenerate modes, meaning they cannot be separated energetically. Figure 2.3(b) shows the energy loss maps for each corresponding peaks (ordered energetically from left to right) in the spectrum in 2.3(a). The energy loss map is a superposition of all possible distributions of the mode at that energy, and are generated in MNPBEM by creating a mesh of impact points across the entire geometry and calculating the energy loss response for each mesh point. The input energy used to generate each EELS map in this thesis is taken as the peak values in the corresponding energy loss spectrum and is taken as a single value. However the maps are created using the broadened electron beam (the beam shape is assumed to be Gaussian in nature [38]). This technique allows us to spatially map the plasmon resonance distribution within the structure and aid to our understanding of geometric effects on the plasmonic properties. The first two energy loss maps look very similar due to the high symmetry of the nanodisk. In figure 2.4 we show a simple schematic of how we acquire (both experimentally and simulated) energy loss maps and the problems with examining highly symmetric structures. The passing electron beam causes a Coulombic response of the free electron cloud within the structure which, for simplicities sake, we have shown as a dipole response in figure 2.4. We can see 4 configurations of the dipole mode for a nanodisk structure, however as this is a symmetric geometry there will be an infinite

amount of dipole alignments. As each mode is generated by the electron beam at different positions across the sample, the resulting EELS map appears as a ring for this nanodisk geometry. Decreasing the number of symmetric axes will reduce this effect [41], but shows the need to calculate the corresponding charge distributions for both the simulated and experimental datasets. The corresponding charge distributions for each peak is shown in the top row of figure 2.3(c).

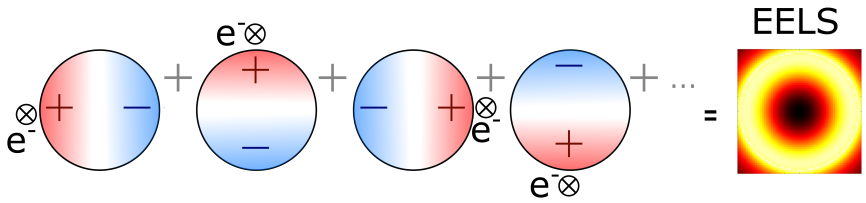

Figure 2.4: *Schematic showing 4 dipole charge distribution configurations within a symmetric circular plasmonic particle. These dipoles are generated by different electron beam positions across the nanostructure, which result in a halo ring in the EELS map. This is a simplified, perfect geometry but highlights the importance of the charge distributions to understand the energy loss results.*

All of the NFTs examined experimentally throughout this work were supported by a Si_3N_4 membrane that needs to be included in the simulations. It will have an effect on the resulting energy loss spectra through scattering (described in section 2.4) within the substrate and surface plasmon generation between the nanoelement and the substrate (see section 1.2) for details). Substrate effects have been studied in reference [37,44,45] where a redshift is consistently observed for a Au element on a Si_3N_4 substrate. However it is important that simulated results corroborate the results obtained in references [44–46]. Here we examine the effects of introducing the substrate within the simulation model. Again a simple Au nanodisk structure of diameter 200 nm, thickness 30nm, was examined

by simulating electron energy loss spectroscopy. A Si_3N_4 membrane was included at a thickness of 30*nm* and dielectric constant of 3.9 [47]. The model was built such that there was no gap between the nanostructure and the substrate (unlike previous MNPBEM substrate models [37]) which required some careful consideration when forming the mesh. In order for the model to compile without fault we had to ensure that the meshing between the upper metallic structure and lower substrate had no overlapping points. Calculations carried out without this consideration can result in unreliable datasets - with outputs of negative loss probabilities previously observed. A number of impact trajectories were assigned onto the xy-plane in the z direction.

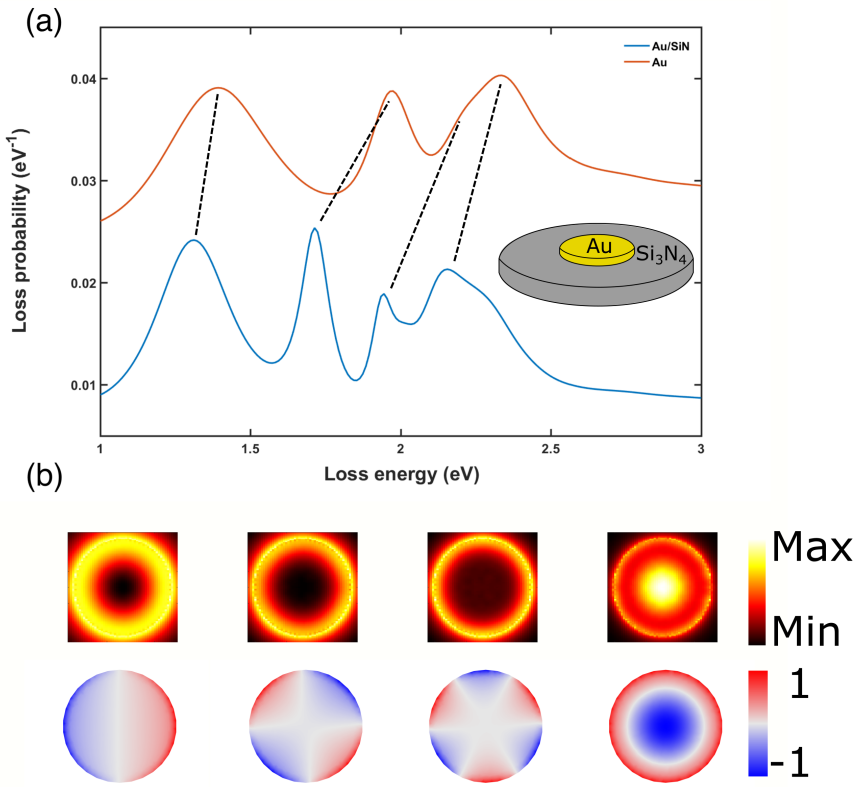

Figure 2.5: *(a) Simulated electron energy loss spectra for an isolated Au nanodisk (red) and a nanodisk on a substrate (blue) with (b) corresponding energy loss maps and (c) charge distributions. A schematic of the disk-substrate system is inset in (a). Resonance energies of each mode are shifted as a result of the substrate due to out-of-plane coupling between the upper metal-air surface and lower metal-substrate layer.*

Figure 2.5(a) shows the simulated energy loss spectra for an isolated nanodisk and the same disk supported by Si_3N_4 substrate with the corresponding energy loss maps and charge distributions shown in figure 2.5(b). Each peak is red-shifted (decreasing in resonance energy) due to the generation of surface plasmons between the dielectric material and the metal, known as proximal modes, that resonate at different energies compared to

the interfaces between the metal and vacuum, distal modes [48]. Coupling between the two types of modes then changes the overall resonance energy of the mode. We understand that there is a redshift in the modes as the energy loss maps and charge distributions match for each peak connected by a black dotted line. The shift in resonance energies differs for each mode in figure 2.5(a) due to the different configurations of the modes, which is consistent with the literature [44–46, 49]. The third-order hexapole mode is clear to see in the spectrum including the substrate, but is enveloped in the breathing mode peak in the isolated disk spectrum. This mode is not generated by the presence of the substrate, but simply shifts its energy and becomes more distinct. Understanding the effect our substrates have on our nanostructures is important in comparing the simulated and experimental data. Throughout this thesis we omit the substrate as part of the simulation model due to the increase in computational time and memory (required memory scales with N^3 [37] where N is the number of nodal point on the mesh of the model), but from figure 2.5 and references [37, 44, 45] we understand the substrate effect on the plasmonic properties of our NFTs, which allows us to make a comparison between experimental and simulated results, whilst excluding the substrate as part of our calculation. Another feature present in the experimental work that was not implemented in the simulations was the adhesion layer used in the fabrication. Details of the adhesion layer are given in section 2.2 and in Chapter 4, but it was omitted from the simulations due to the complications that arose when carrying out the calculation. MNPBEM fails to calculate when the faces of two surfaces are too close together, and due to the size of the adhesion layer the resulting energy loss spectrum was non-physical and erroneous.

A key design parameter that can be used to easily tune a NFT's resonance energy of

the plasmons is the size of the plasmonic structure. In order to illustrate the effect of increasing size we simulated a nanodisk with a diameter ranging from 70 nm to 700 nm, thickness 25 nm. As before, the particle was simulated with numerous electron trajectories and the resulting spectra are summed to give an overall figure of the plasmon resonances in the particle. Figure 2.6 shows the peak energies for each resolvable plasmon mode as a function of nanodisk diameter and shows a gradual decrease in energy of all modes as the diameter is increased, with the dipole mode redshifting by roughly 1.5 eV when comparing the smallest and largest structures. As the particle size increases the energy decreases for each of the resonance modes due to the increase in distance between the opposing charges. There was no notable change in peak width as a function on diameter, and the changes in the spectrum lay in the peak positions.

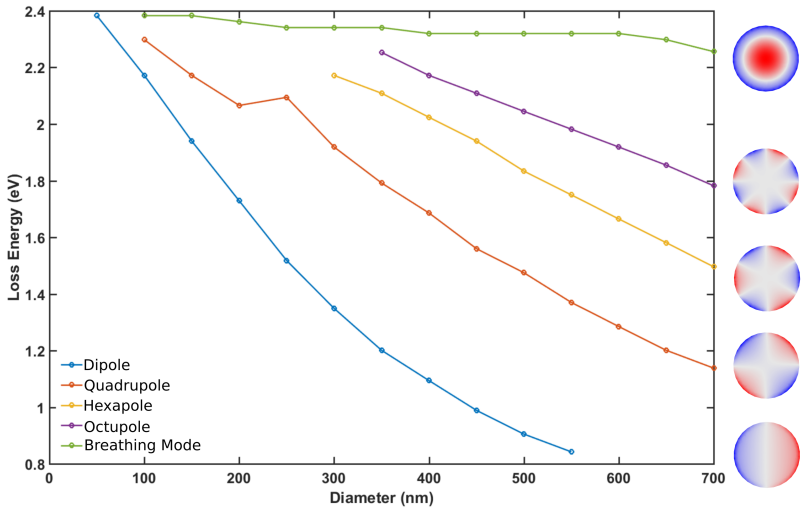

Figure 2.6: *Plasmon resonance energy for a number of modes as a function of size. Increasing the diameter of the nanodisk decreases the resonance energies of the modes. Other higher order modes become non-degenerate at certain diamaters for some modes.*

Another feature observed in figure 2.6 is that higher order modes are resolved as the diameter increases. For small diameters the energies of the modes are too close together to be resolved but as we increase the diameter, there is a separation of the closely spaced modes and we can resolve the individual modes. The smallest diameter, 50nm, only has one resolvable mode: the dipole mode. As we increased the diameter of the nanodisk to 100nm, two more modes are resolvable: quadrupole and breathing mode, as can be seen in figures 2.5 and 2.3. Increasing the diameter further then another two higher-order modes: hexapole and octupole modes. Figure 2.6 also shows the large dependence the size of the structure has on the resonance energies of the plasmon modes [50]. The size of the nanostructures is an important aspect in this work as the plasmon generated are being studied using EELS, which has limitations in its energy resolution (see section 2.4).

2.2 Electron Beam Lithography

Electron beam lithography (EBL) was the chosen method of sample fabrication as it allowed us to create electron transparent ($<$ 100 nm thick) samples and design structures. All NFTs studied in this work were deposited onto Si_3N_4 membranes supported by a Si chip and created in the James Watt Nanofabrication Centre (JWNC) of the University of Glasgow. A schematic of these membranes is shown in figure 2.7. The window in the centre of the chip is roughly 100×100 μm and the membrane thickness is 30-50 nm. These membrane windows are made through wet etch of Si. A Si wafer is coated with a layer of Si_3N_4 on top and a Si_3N_4 mask underneath. The Si wafer is then wet-etched leaving a Si_3N_4 window.

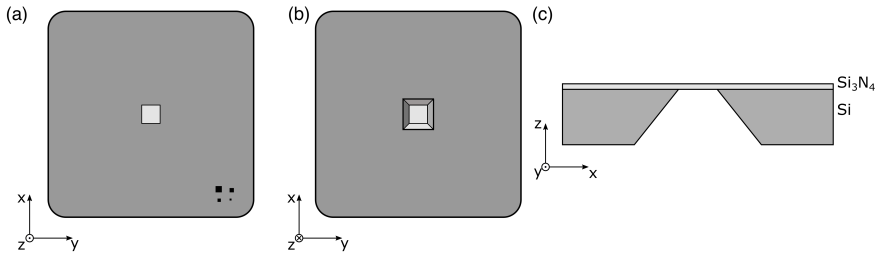

Figure 2.7: *Schematic showing the TEM membranes: (a) top-down view (b) bottom-up view and (c) cross-sectional side view. The central window is* 100×100 μm*. A thin layer of* Si_3N_4 *was deposited onto Si and back etched, leaving only the* $30-50$ *nm thick* Si_3N_4 *layer.*

All experimental samples examined in this thesis are Au nanostructures, fabricated onto Si_3N_4 membranes using a 2nm adhesion layer. Details of the adhesion layer are given below and in Chapter 4. Fabrication of nanoelements by EBL was a crucial part of the experimental work and was carried out in the JWNC using the Vistec VB6 UHR EWF electron beam lithography tool, shown to have capabilities of fabricating features < 5 nm wide [36]. This process starts by designing structures to be made within L-Edit software - a computer-aided design (CAD) software used to create 2D structures. After the designs have been created they were then processed in BEAMER - software which converts these designs into a file format that can be sent to the EBL tool. The output file is then processed through another software package, Belle, which allows the user to assign substrate parameters, doses of the beam, and global and local markers for alignment. It is then transferred to the EBL tool to be written. The EBL process is highlighted in figure 2.8 and is described as follows. This fabrication process is unique to TEM examination and was based off of the expertise within the MCMP group, particularly the work carried out by Dr. Gary Paterson which he has used, for example, to fabricate concave chiral plasmonic

structures [51].

Si_3N_4 membranes were cleaned in acetone and IPA for 5 minutes in a water bath at 50°C then blown dry by N_2. They were then baked at 180°C to drive off residual moisture. In order to carry out the lift-off method of fabrication, two layers of resist were spun and baked to create an undercut profile upon exposure from the beam. This is necessary to prevent depositions sticking to the inner walls of the developed wells, leaving scraggly, rough edges on the nanoelements that would effect the plasmonic properties of any fabricated sample. The bi-layers used here were two layers of positive resist, poly(methyl methacrylate) (PMMA), with the top layer (dark blue layer in figure 2.8) having a higher molecular density than the bottom (light blue layer in figure 2.8). The resist was then irradiated using an electron beam using 100kV acceleration voltage within the EBL tool, which causes a chemical reaction (electron attachment) and changes the solubility in a known solvent (solvent is dependent on the resist being used) [52]. The bi-layers of resist will have different reactions to the exposure and will leave an undercut layer, as shown in figure 2.8. The exposed resist was developed using 2.5:1 ratio of IPA and methyl isobutyl ketone (MIBK), leaving wells of the geometries we have defined in CAD software. From here we can deposit our desired metal into the wells and remove the residual resist using, again, acetone and IPA. Depositions were carried out using the Plassys MEB 550S electron beam evaporator tool in the JWNC. This deposition technique is carried out by bombarding a target ingot with an electron beam that is generated from a filament. The interaction between the electron beam and the ingot creates a vapour which is then deposited onto our sample [53]. For the majority of the experimental work carried out here, we examined Au as a plasmonic material. Due to the low chemical reactivity of Au, if no adhesion layer was

used the deposition would succumb to problems like dewetting and deterioration. Using a more chemically reactive material as an adhesion layer (throughout this work we used 2nm Ti layer as shown in figure 2.8) prevents these problems from occurring. However the presence of an adhesion layer will affect the properties of the Au structures, dictating the grain size of the deposition [54] and quenching plasmon modes [55]. This is explored further in chapter 4 where we consider the adhesion layer and its effect on the structural and plasmonic properties of Au NFTs.

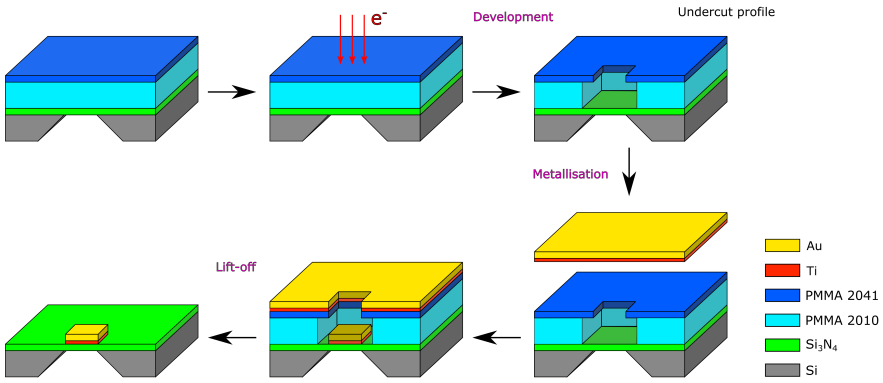

Figure 2.8: *Electron beam lithography fabrication of NFTs using a lift-off process. The Si_3N_4membranes are coated in two layers of resist with the upper layer having a larger molecular weight than the under layer. The sample is selectively illuminated with an electron beam, writing a pattern created by the the user. Developing the resist removes only the exposed layers, creating an undercut layer necessary for a clean lift-off. Metal is deposited and the residual resist is removed with acetone and IPA, leaving the fabricated structures.*

There are limitations in the size of geometries physically possible from electron beam lithography. For the work carried out here the smallest feature of the particles was tens of nanometres wide. Shown in figure 2.9 are TEM images of the fabricated array using EBL. Figures 2.9 (a) and (c) show the fabrication of a number of elements that have successfully

retained their designed geometry. Figures 2.9 (b) and (d) illustrate some typical problems of creating small features using this method for EBL. In these figures it is clear to see that problems arises when fabricating annular structure where the highlighted structures are 'broken'. This is due to the nanostructure being too small for this fabrication method and the hole is positioned too close to the edge, as discussed in chapter 4. In figures 2.9 (b) and (d) the distance between the outer edge and the hole is 25-40 nm, which was taken to be the limit of this fabrication process. To overcome this problem one can carry out fabrication with a negative resist like hydrogen silsesquioxane (HSQ). The process is not too dissimilar to the lift-off process however the metal is deposited initially then the resist is spun on top. The resist is exposed and developed leaving only the radiated HSQ which can then dry etch using a reactive gas with a known etch rate, leaving only the defined geometries. This process has been used to make features of well below 10 nm [36]. However, the successfully fabricated samples examined here were of a good size therefore we used the lift-off process throughout.

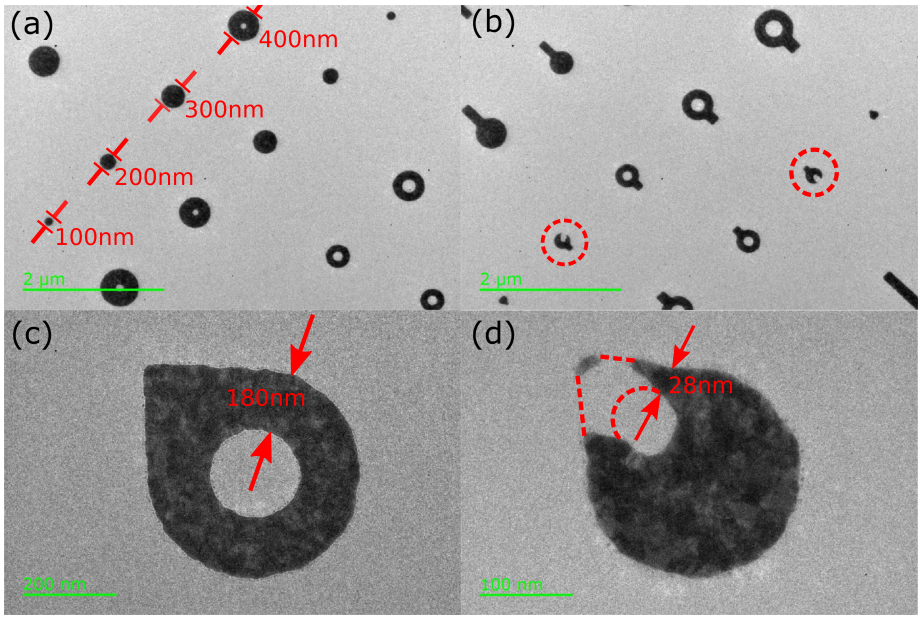

Figure 2.9: *(a), (b) Arrays of NFT designs with incremental changes in size and different geometries. (b) Two structures are highlighted to show the limitations in feature size fabrications using EBL. (c), (d) Individual structures where the process has been successful, (c), and unsuccessful, (d). The failure of the latter case is due to the size of the smallest edge, which have been outlined.*

Another aspect we explored in fabricating our NFTs was the dose of the electron beam used to radiate the resist. Dose is the electron flux measured as the charge, μC per cm^2. It is an important variable in EBL as it defines the ability to properly irradiate the resist while minimising the proximity effect, which is an issue of overexposing the resit to secondary electrons [52] (described in section 2.5), whilst exposing the material enough to change the solubility in a known developer. In our work the EBL jobs were carried out done onto primarily 30 - 50 nm thick Si_3N_4 membranes shown in figure 2.7. By changing the dose we then change the size of the particle being fabricated. Using two nanotriangles of different design sizes, we measured the effective size in comparison to the CAD design size for all

three sides of the triangle, ensuring the microscope was properly focused to ensure the measurements were accurate. We define the error as the difference between the fabricated and the design dimensions whilst plotting the relative error percentage rather than the absolute as the sizes of the nanotriangles examined differ. There are two peaks observed in figure 2.10 at 700 $\mu C/cm^2$ and 970 $\mu C/cm^2$, where the error percentage is 10.1% and 7.8% respectively. These are the doses which have the largest difference between design and fabricated dimension for the collected dataset. A minimum error percentage of 1.4% is seen at a dose value of 920 $\mu C/cm^2$. This minimum point indicates the dose at which the fabricated samples are most similar to the designs submitted to the EBL tool. Figure 2.10 highlights the importance of dose in EBL and how sensitive sample sizes are to different levels of dose. Dose tests, such as the one shown in figure 2.10, were carried out for each fabrication as error percentage can change from sample to sample (slight changes in resist thickness, residual substances such as IPA/acetone, etc. can all attribute to the resulting size of the fabricated structure [52]).

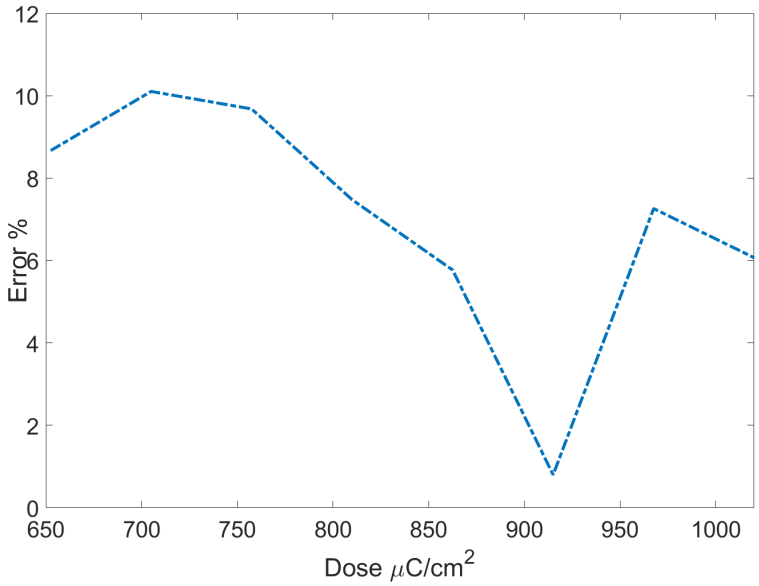

Figure 2.10: *Average error percentage of fabricated sizes of nanotriangles as a function of EBL dose.*

EBL on Dedicated Heating Chips

In chapter 4 we examine the environmental effects on the plasmonic properties of NFTs. An aim of this chapter was to carry out electron energy loss spectroscopy whilst heating the NFTs in the microscope. In order to do so, we tried fabricating Au NFTs on top of dedicated heating chips, specifically created to fit in the DENS Solution Wildfire heating rod [56]. The composition of these chips is similar to the membranes shown above, with a thin Si_3N_4 layer (40 nm) on top of Si. Details of the chips can be found in reference [57]. However, complications arose when carrying out the fabrication process shown above, leading to failed sample creation and we began the task of testing each step in the process. The main source of error in this fabrication was the lack of adhesion of PMMA resist

onto the heating chip. Due to reasons unknown (communications with the manufacturer did not reveal the source of this problem) the resist would not adhere to the chip, leaving large areas uncovered and a huge amount of streaking - thin and long strands of resist. To overcome this issue, and after consulting with the JWNC technicians, we used a Ti layer to help the resist adhere to the heating chip. This improved the spin-coating significantly and allowed us to continue with the fabrication. Fabrication testing results are omitted here but the completed fabrication is shown in figure 2.11, showing (a) an array of NFTs deposited onto the chip, and (b) individual NFTs on Si_3N_4 membranes. In 2.11(a) we used a scanning electron microscope (described in section 2.5) to examine the fabrication which, from initial examination, was successful. We can see fabricated NFTs on top of the Si_3N_4 membrane (the rod features with rounded edges seen in both the left and right images). In figure 2.11(b) we show transmission electron microscope images of individual structures. In each image we see a number of issues with the fabrication. Residual resit has not been fully removed from the specimen, resulting in a large disk-like extraneous feature being left in top of the NFT (highlighted in the left image in red). The samples shown here, and indeed seen throughout the specimen, have a large amount of residue around the perimeter of the structure, which is a mix of residual resist and Au nanoparticles. Electron energy loss spectroscopy was carried out using the samples shown in figure 2.11, however there was no plasmonic activity observable for each of the examined nanostructures. This was in part due to the residual resist present on the samples which creates thick regions which do not produce EELS signals good enough to probe the plasmonic properties [58]. Due to time constraints, this piece of work was unfortunately taken no further, however further work into perfecting this fabrication process would allow one to examine NFTs

using EELS whilst heating in the microscope - an experiment at the forefront of plasmonic research.

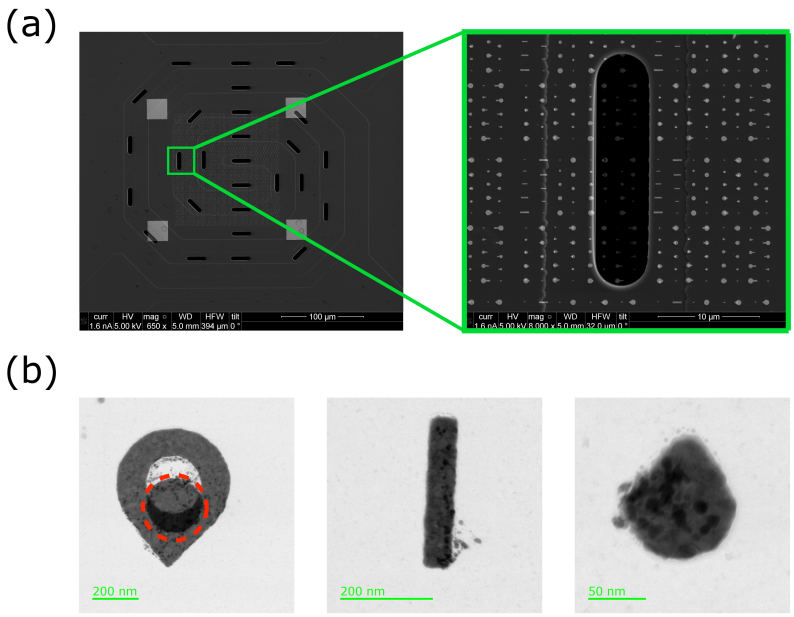

Figure 2.11: *(a) SEM images showing the full array of structures fabricated over the DENS Wildfire chip. The region highlighted in green is one membrane over which we can see NFT structures successfully createded on top of the Si_3N_4 membrane. (b) TEM images of individual NFTs, showing non-ideal fabrication. Highlighted in the left figure is a large deposit of residual resist. Each NFT shown here has extraneous particles around the perimeter of each structure, and are unexaminable by EELS.*

2.3 Transmission Electron Microscopy

Conventional optical microscopy is limited by the diffraction limit of visible light where the smallest observable structure d, is determined by $d = \lambda_{opt}/2NA$, where λ_{opt} is the wavelength of light and NA is the numerical aperture [59]. For visible light wavelengths

the resolution can be down to 250 nm [59]. Other methods such as scanning near-field optical microscopy (SNOM) have the potential to observe sub-diffraction limit structures but is limited by optical throughput [60]. Another, more reliable method for reducing the diffraction limit is to reduce the wavelength of the incident excitation. Electron microscopy has been shown to be an incredibly powerful tool in material science with the ability to not only image at the atomic scale, but to determine characteristic properties of the materials making up the sample through elastic and inelastic scattering events between the electron beam and the sample. Here we employed transmission electron microscopy (TEM) in both conventional (CTEM) and scanning (STEM) modes. The relativistic wavelength of the incident electron is given by

$$\lambda = \frac{h}{\sqrt{2m_o eV(1+\frac{eV}{2m_o c^2})}}, \tag{2.12}$$

where m_0 and e are the respective rest mass and charge of an electron, c is the speed of light in a vacuum, and h is Planck's constant. V is the accelerating voltage which throughout this thesis was set to 80 kV, giving a wavelength of $\lambda_{80kV} = 4.18pm$, which is smaller than interatomic spacing distances. The resolution of the microscope is not just defined by the wavelength of the electrons, but also by the aberrations from the electromagnetic lenses which will limit the capabilities of the microscope. There are a number of advantages to TEM when compared to optical methods such as SNOM. For instance the resolution for TEM far outperforms SNOM, allowing the user to image much smaller samples in finer detail, and when married with electron energy loss spectroscopy, TEM method allows for the physical chemistry of a sample to be examined. These capabilities come at a cost

however, and the main advantage for the SNOM technique is that it is a much cheaper experimental method to buy and run.

Electron Source & Lenses

In electron microscopy there are a number of electron sources which determine aspects as brightness, probe size, spatial resolution, etc. The work presented here uses two electron microscopes with two types of sources: a thermionic emission gun and a cold field-emission gun (CFEG). In the Material and Condensed Matter Physics (MCMP) group in the University of Glasgow we have a CTEM FEI Tecnai T20 electron microscope, used in chapter 4, which has a thermionic emission gun. This electron source is a tungsten filament or lanthanum hexaboride (LaB_6) crystal, with the latter being preferred due to its low work function (and the source used here) - requiring less energy to extract electrons from the source [61]. A LaB_6 thermionic emission gun has a gun-cross over (the focal point of the electrons after leaving the source, which defines the absolute resolution of the system) of the order of 10^4 nm. The MCMP group also has a JEOL ARM 200F STEM with a CFEG as an illumination source. In this gun a high electric field is applied to a sharp tip, typically made of tungsten, and anodes are placed close by. The sharp tip locally enhances the the electric field at the tip, lowering the energy barrier. The electrons can then tunnel out [61]. The current density of the beam formed by a CFEG is determined by the Fowler-Nordheim formula,

$$J = \alpha E^2 exp\left(\frac{\beta \Phi^{3/2}}{E}\right), \tag{2.13}$$

where β is a constant and α is a material constant. The CFEG uses two anodes to extract electrons from the source, which has its advantages. The first anode extracts electrons from the biased tungsten tip and the second accelerates the electrons through a set potential. The use of two anodes allows for the gun cross-over to be reduced much more for CFEG compared to a thermionic gun. Another advantage to using CFEG over thermionic is the energy spread of the beam. This is related to the coherence of the beam and is vital for plasmonic studies. The energy spread in a beam formed by a typical CFEG is $\Delta E = 0.3$ eV whereas in a thermionic source it is roughly 1.5 eV - 3 eV depending on the source. When using EELS for analytical work ΔE becomes important in defining the energy resolution capable by the tool. Minimising the spread will optimise the energy resolution of the analysis [61]. All analytical work on plasmonics throughout this thesis was carried out using a CFEG STEM.

Another section of any electron microscope is the electromagnetic lenses found throughout the column, used to focus the electron beam. A schematic of an electromagentic lens can be seen in figure 2.12. Standard lenses comprise a soft magnetic pole-piece which is cylindrically symmetric, typically Fe, surrounded by copper coils which carry a current - a magnetic field is generated from Ampére's law. Between the upper and lower pole pieces there is a gap where the magnetic field is concentrated. This magnetic field is concentrated to the centre of the bore (indicated in figure 2.12) which is the used to focus the electrons passing through. The strength of the magnetic field is due to the current passing through the copper coils, hence focusing the electron beam in the microscope is done by micro-changes to the current of the lenses. As an electron of velocity $\mathbf{v}$ passes though a magnetic

field **B** of the lens, it is subjected to the Lorentz force **F**, given by:

$$\mathbf{F} = -e(\mathbf{v} \times \mathbf{B}), \tag{2.14}$$

where e is the charge of an electron. The force can be rewritten as $F = -evBsin(\theta)$, therefore if the velocity of the electron is parallel to the magnetic field, the electron will travel through undisturbed. If, however, the velocity is not parallel to the magnetic field, then the electron will experience the Lorentz force. The inset of figure 2.12(b) shows the velocity components of the electron trajectory where $\mathbf{v}_2$ is the velocity component parallel to the optical axis and the magnetic field. $\mathbf{v}_1$ is the component perpendicular to the optical axis and results in circular motion with radius $r = mv/eB$ - cyclotron radius. The resulting trajectory of the electron in the magnetic field is the helical, as depicted in figure 2.12(b) [61].

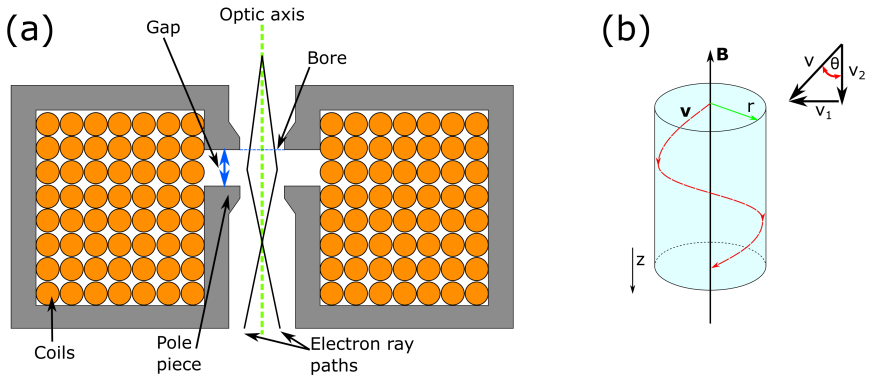

Figure 2.12: *(a) Cross-section of a typical electromagnetic lens found in a modern transmission electron microscope. This lens consists of a soft magnetic upper and lower pole-piece, separated by a gap, and copper coils with a current - creating a magnetic field at the gap. An electron beam passes through the bore and is focused using the magnetic field. (b) The helical trajectory of an electron when the velocity is not parallel to the magnetic field. The inset shows the velocity components parallel ($\boldsymbol{v}_2$) and perpendicular ($\boldsymbol{v}_1$) to the magnetic field. The latter causes circular motion of the electron, resulting in a helical trajectory.*

Electron Microscope Optics

In this thesis we used two types of transmission electron microscopy: conventional and scanning. The CTEM used in this work is the FEI Tecnai T20 electron microscope equipped a LaB_6 crystal source. Figure 2.13 (a) shows a ray diagram for CTEM which is split into three parts: the condenser, objective and projection systems. After the electron beam is emitted from the source, it first encounters the C1 and C2 lenses - used to control the illumination of the specimen. C1 lens controls the *spot-size* of the beam, which is the magnification of the gun crossover. The second condenser lens, C2, is responsible for the brightness/intensity of the beam, and defines whether the sample is being illuminated by a parallel or convergent beam (figure 2.13(a) shows a parallel beam illuminating

the specimen). A condenser aperture is used after the C2 lens to block high-angle electrons contributing to the beam, ensuring that the beam is coherent but at a cost of current density [61]. The objective system shown in figure 2.13 consists of an upper and lower objective lens placed above and below the specimen. Shown in figure 2.13(a), the upper objective lens is used to create parallel illumination of the sample but can be used to converge the beam on the sample (not shown here). After the electron beam is transmitted through the sample, the lower objective lens then projects a diffraction pattern in the back focal plane (BFP) where an aperture is placed. This aperture is a vitally important element in the microscope as it controls the collection angle of electrons imaged, which in turn determines the effect of aberration in the electron beam since higher angle electrons are more effected by aberration [62], described below. The first intermediate image is formed in the plane of the selected area aperture, which can be used with diffraction lens (not shown here) for generating diffraction pattern images of the sample. The projection system magnifies the images or diffraction patten onto the viewing screen [61] (or camera for recording).

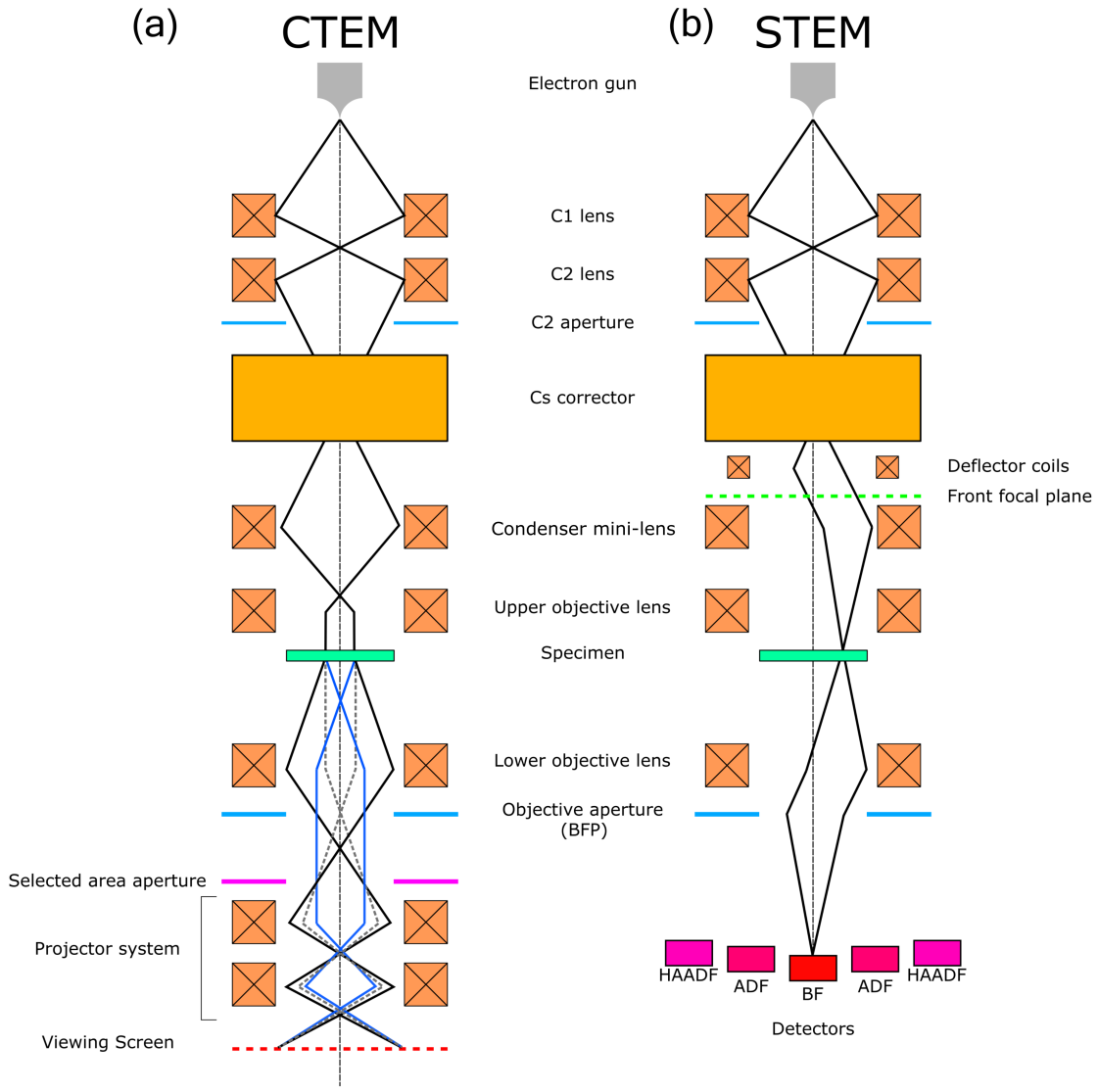

Figure 2.13: *Ray diagram for a transmission electron microscope in (a) conventional mode and (b) scanning mode. Electrons emitted from a source are accelerated and focused through a series of magnetic lenses, illuminating a specimen. The beam then passes through the sample and an image is formed. CTEM uses parallel illumination where as STEM has a probe beam which is scanned across the sample.*

Electron microscopes in general suffer from aberrations that limit the overall resolution capable by the system. Two significant forms of aberrations which are considered here are: spherical and chromatic. Spherical aberrations (C_s) arise from the lenses acting inhomogeneously to rays not on the optical axis. It is a radial effect on the electron beam and the further away from the optical axis the electrons are, the larger the effect of spherical aberration is observed [63, 64]. This is shown in figure 2.14(b) where the focal point changes due to the inhomogeneity of the lens. This defect results in a loss of information during magnification: for example, a point source is imaged as a disc of finite size in the plane of least confusion. Spherical aberration effects are minimised in the condenser and objective systems with octupole correcter lenses (Cs lens in figure 2.13) [61]. Chromatic aberration is an effect caused by the lenses focusing with different strengths due to the different energies of the electrons in the beam, shown in figure 2.14(c) (the different coloured beam paths indicate different electron energies). Electrons from the source are chromatic, resulting in different focal points for the beam as it passes through the electromagnetic lenses. Lower energy electrons are focused at shorter distances meaning the are spread out to higher angles, which leads to loss of information at high magnification [65]. Chromatic aberration can also be caused by inelastic scattering of electrons within the specimen - resulting in differences in energy for the electrons post-interaction with the sample. The choice of source, thinning of samples (reduces scattering events), and corrector lenses all help with minimising the effect of chromatic aberration.

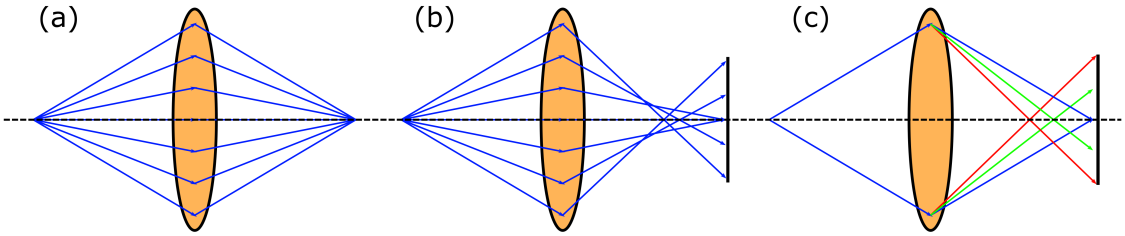

Figure 2.14: *Schematics of electromagnetic lens aberrations. (a) perfect lens with no aberrations, (b) shows the effect of spherical aberration and (c) shows chromatic aberration effect.*

Shown in figure 2.13(b) is the ray diagram for STEM, which is very similar to CTEM the electron beam is focused into a probe. The JEOL ARM 200F electron microscope is the tool used throughout this thesis to perform STEM (with EELS) on fabricated samples. Figure 2.13(b) shows a deflector coil set (simplified to one coil for the schematic but consisting of multiple coils) above the upper objective lens, which is used to ensure that the point probe is parallel to the optical axis as the beam is rastered across the specimen. The condenser mini-lens is used to form a probe onto the sample [61]. As the beam is scanned across the sample, a point-by-point image is formed on a computer for images collected by the detectors. The detectors in figure 2.13(b) are: bright field (BF), annular dark field (ADF), and high angle annular dark field (HAADF) - descriptions of which are given below. STEM has atomic-resolution capabilities (not required in this work) [66] but careful consideration has to be taken in order to do so. Some factors that effect the overall resolution are spherical aberration (see above), the finite source size, and the diffraction limit. The tool used here is equipped with a CFEG electron source and utilises Cs corrector to obtain sub-angstom spatial resolution [66].

Bright Field and Dark Field Imaging

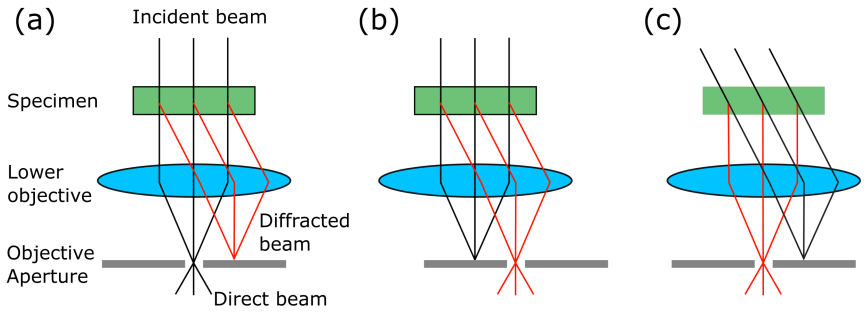

Figure 2.15: *Schematic of BF (a), DF (b) and tilted DF (c) imaging modes in CTEM. In these figures, the black and red lines shows the direct and diffracted beams respectively. In (a) and (c), objective aperture is centred around the optical axis and in (b) the objective aperture is shifted to an off-axis position. (b) and (c) allow for the imaging of the diffracted beam (DF), and (a) shows the imaging of the direct beam (BF).*

As mentioned above, there are different methods of imaging in the TEM. Bright field and dark field imaging are possible in both microscopes described previously, but shown in figure 2.15 are the imaging techniques for CTEM. BF imaging, 2.15(a), is imaging the direct electron beam that is transmitted through the specimen. The diffracted beam in this schematic is blocked out by the objective aperture which is centred around the optical axis (the objective aperture is on the BFP, where the first image is formed). In figure 2.15(b), DF imaging is carried out by shifting the objective aperture off the optical axis to allow the diffracted beam to pass through the column. Tilted DF (sometimes known as centred DF) imaging is shown in figure 2.15(c). In this technique the beam is tilted, allowing for the diffracted beams to pass through the centre of the lower objective lens and through the centred objective aperture. This method allows the diffracted beam to avoid the outer regions of the lens which as more partial to spherical aberrations [64]. For STEM mode,

the point probe illumination is imaged using BF, ADF and HAADF detectors as shown in figure 2.13(b). The BF and ADF detectors collect electrons at angles of < 10 mrad and > 10 to < 50 mrad respectively. The HAADF collection angle is > 50 mrad and offers an advantage to ADF as it produces mass-thickness contrast images with no Bragg effects [61]. These high-angle, low signal images show variations in contrast for differing atomic number for atoms and is a technique used in atomic imaging [67].

2.4 Electron Energy Loss Spectroscopy

In this thesis we use electrons as a method of plasmon excitation for our simulated and fabricated Au specimens. An incident electron interacts electrostatically with a sample causing elastic and inelastic scattering with its atoms and electrons. Figure 2.16 shows a number of different scattering interactions for an incident electron beam on a specimen. SEM and TEM (both used in this work) have a multitude of electron-matter interactions due to the nature of the experiment and samples being examined, this is depicted in figure 2.16 .

It is useful to distinguish two types in interactions between incident electrons and matter. Elastic scattering is caused by the interactions between the incident electrons and the positive electrostatic charged nuclei of a material. In SEM this interaction takes the form of backscattered electrons, where the electron trajectory is greater than 90° [61]. Forward scattering of this collision can cause small angle deviation in the electrons trajectory path.

Inelastic scattering is caused by interactions between the incident electron and the atomic electrons of the specimen, through a multitude of events. Interactions between the

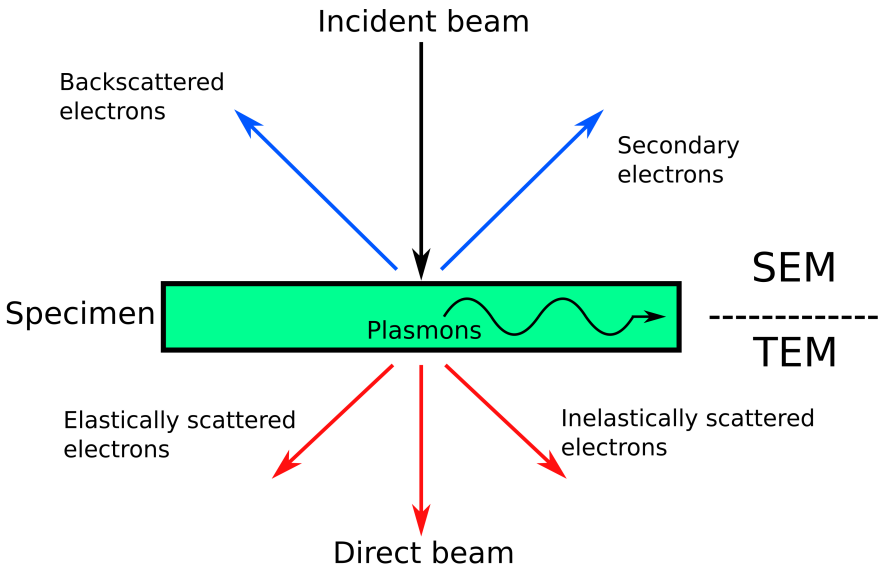

Figure 2.16: *Diagram showing incident electron beam interactions with a specimen - split between scanning electron microscopy and transmission electron microscopy imaging methods.*

incident beam and the inner electron shell can cause generate characteristic X-rays and Auger electrons as atomic electrons are excited to higher energy levels.Both interactions are similar as the high energy incident electron interacts with the inner-shell electron and ejects it from the atom. For characteristic X-ray emission, the resulting inner-shell hole is filled by an electron from the outer-shell which results in an X-ray emission with the energy equivalent to the difference between the two energy states. The energy released when filling the inner-shell hole can also be released as an electron from the same energy level - an Auger electron. Both of these physical phenomenon can be used to characterise the atoms that they occur in [61]. Secondary electrons are also produced as a consequence of inelastic scattering, and are utilised in scanning electron microscopy as an surface imaging

method [68]. Interactions with outer shell electrons can cause the excitation of a number valence electrons collectively, creating longitudinal oscillations in thin samples. This is plasmon generation, as depicted in figure 2.16. For a in-depth description of electron scattering, details can be found in references [62]

Throughout this thesis, electron energy loss spectroscopy (EELS) is used as a method of examining plasmonic properties of Au nanostructures, using both simulated and experimental techniques. The JEOL ARM 200F STEM has EELS capabilities which allow us to examine fabricated structures. EELS can be used to characterise a wealth of information about a sample due to different elastic and inelastic scattering events described above. EEL spectra are conveniently split into two categories: low-loss (< 50eV) and high loss (> 50eV) spectra which are illustrated in figures 2.17(a) and (b), respectively. By considering the different scattering events between a specimen and a fast moving electron, we can understand information from both of these datasets. The high-loss regime holds information of inelastic scattering interactions between inner (core) electrons and the fast moving electrons of the incident beam. Electrons, typically from the L, K and M shells of the sample, are excited to an unoccupied state above the Fermi energy by an energy amount which is a characteristic of the element [11]. This method can be used to determine the chemistry of the specimen, and when married with STEM, can be used to chemically map the specimen [67, 69]. In figure 2.17(b) we show a high-loss spectrum of a fabricated nanostructure with a number of clear edges appropriately labelled. Indicated in this figure is the background signal which is assumed to be a decaying power law [67]. The edges seen in this energy range are the nitrogen K edge, titanium L edge, and oxygen K edge, which come from the Si_3N_4membrane and the oxidised titanium adhesion layer

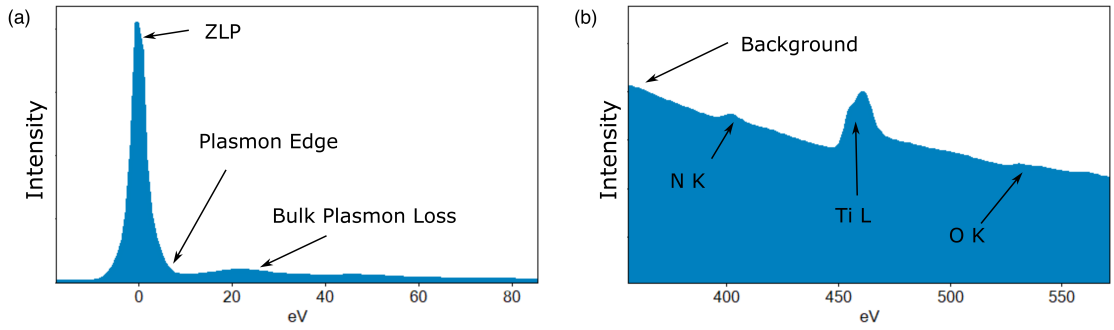

Figure 2.17: *EEL spectra for low-loss mode (a) and high-loss (b) obtained for Au nanostructures fabricated onto Si_3N_4membrane. Low loss spectrum is dominated by the ZLP generated by electrons passing through a specimen without losing energy. Bulk and surface plasmon generation energy regions are highlighted. High loss spectra contains information of elastic scattering events from core electron, with edges used as a mean of chemical analysis. In (b) 3 edges are: nitrogen K edge, titanium L edge and oxygen K edge.*

described in section 2.2. In this work, however, the high-loss data are not used as we examined the dielectric properties of Au nanostructures. As indicated in figure 2.17(a), the most prominent feature in the low loss spectrum is the zero-loss peak (ZLP). This peak derives from electrons that have not lost energy as they were transmitted through the specimen. The full width half maximum (FWHM) is determined by the energy spread of the electron source. The inelastic scattering, rising from a few eV energy loss, at this energy range is dominated by plasmon generation [27, 48, 70] . The incident electron beam scatters with loosely bound valence electrons to excite plasmons, which are the focal point of this work. In figure 2.17(a) two regions of plasmon generation have been indicated. The higher energy plasmon generation is due to bulk plasmonics, as described in section 1.2. For the work carried out in this thesis, we examine the energy range at the tail of the ZLP, indicating the importance of a CFEG electron source with a low energy spread.

The EEL spectrometer used in this thesis is a Gatan Image Filter (GIF), a simple

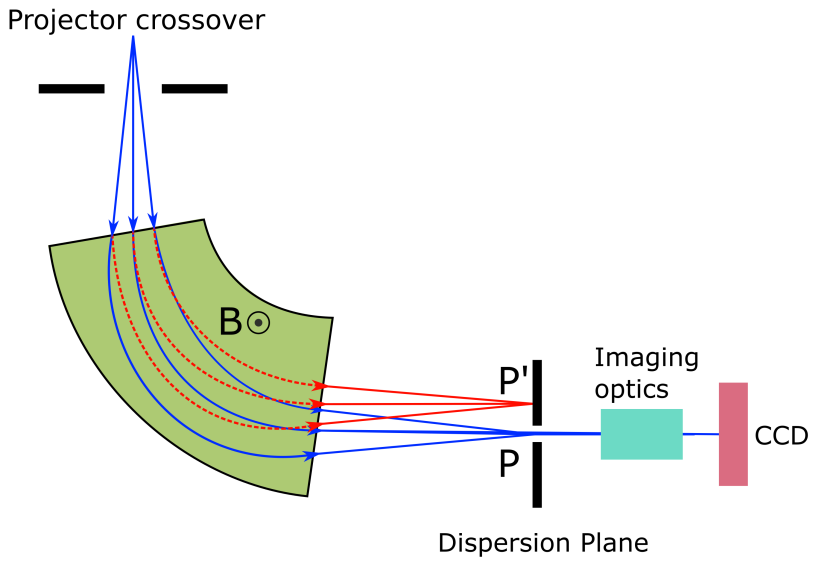

Figure 2.18: *Simple schematic of an electron energy loss spectrometer. The red beams represent the electrons that have lost no energy as the beam is transmitted through the sample. They are deflected by the Lorentz force through approximately 90^o and enter the camera, forming the zero-loss peak. The green beam illustrates energy loss electrons, deflecting through a greater angle due to their lower velocity.*

schematic of which is given in figure 2.18. The spectrometer is mounted post column, after the viewing screen in the JEOL ARM 200F, meaning that the BF detector in figure 2.13(b) is moved out of the beam's path in order to allow electrons to pass through the column and into the spectrometer. As the figure shows, an electron beam from the electron microscope passes through an aperture, which is used to control the collection angle of electrons entering the spectrometer [61]. The electrons then pass through a magnetic prism which deflects electrons through different angles due to their velocity [58] using the

Lorentz force. The radius of curvature that the electron experiences is given by

$$R = \frac{\gamma m_o}{Be} v, \tag{2.15}$$

where m_o is the resting mass of an electron, B is the magnetic field strength, e is the charge of an electron, v is the velocity and γ is the relativistic factor given by $\gamma = 1/\sqrt{(1 - v^2/c^2)}$. Electrons that have lost energy in the process of transmission through the specimen will have a lower velocity which means they have a smaller radius of curvature, and therefore are deflected through a larger angle when compared to electrons that were elastically scattered. For example in figure 2.17, electrons that form the ZLP (blue line) pass through the magnetic prism and converge onto the dispersion plane point P. Electrons that have undergone energy loss (red line) pass through the spectrometer and form an image at point P'. The electrons converging at point P' are blocked by an energy filtering slit on the dispersion plane. The slit width can be controlled piezoelectrically, determining the amount of electrons entering the imaging optical unit and Charge-Coupled Device (CCD). The imaging optics unit consists of a series of quadrupole and sextuple which restores the cylindrical symmetry of the electron beam which has been lost due to the prism [58] and the beam is detected ad recorded by a CCD camera, more details of which are given below.

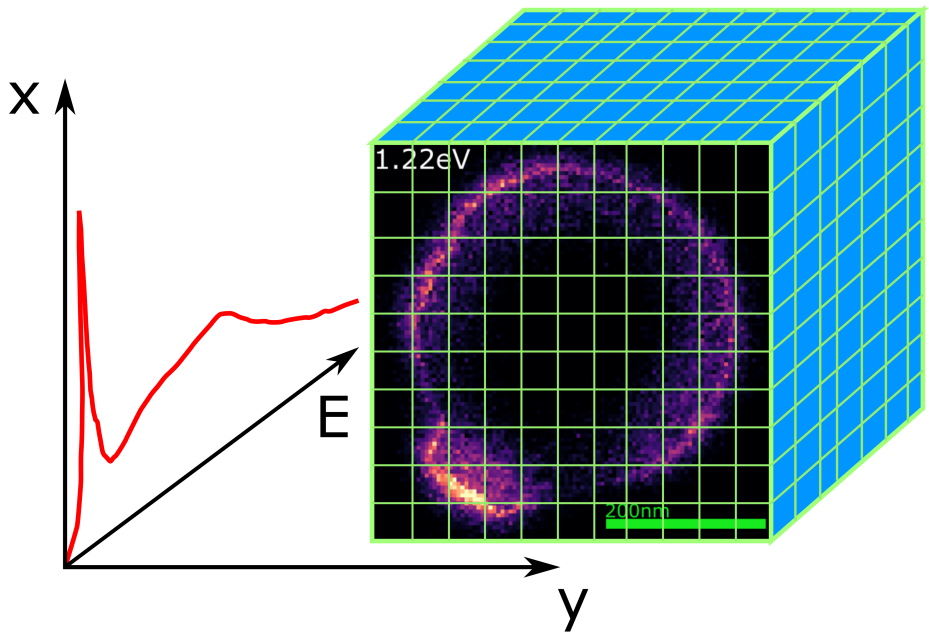

Figure 2.19: *EELS spectral image data cube of dimensions x, y, and E. Data shown in this figure is taken from the nanolollipop structure examined in chapter 3. This 3D data set can be used to build a spatial and energy landscape of the plasmonic properties of nanostructures.*

As mentioned above, STEM acquires images in a point-by-point process as the beam is scanned across the specimen, building a 2D image. The technique of EELS spectral imaging (SI) involves collecting an energy loss spectrum for each point in the 2D imaging process, which builds a 3D data cube shown in figure 2.19. The EELS SI method is incredibly useful in plasmonic research as it allows for the spatial mapping of plasmon excitations for selected energies [11, 25]. Using processing techniques outlined below, we are able to build a spatially distributed energy loss map for a given energies and understand the geometric effect on the plasmonic properties of a nanostructure.

The process of acquiring data in the spectrometer requires the user to input variables

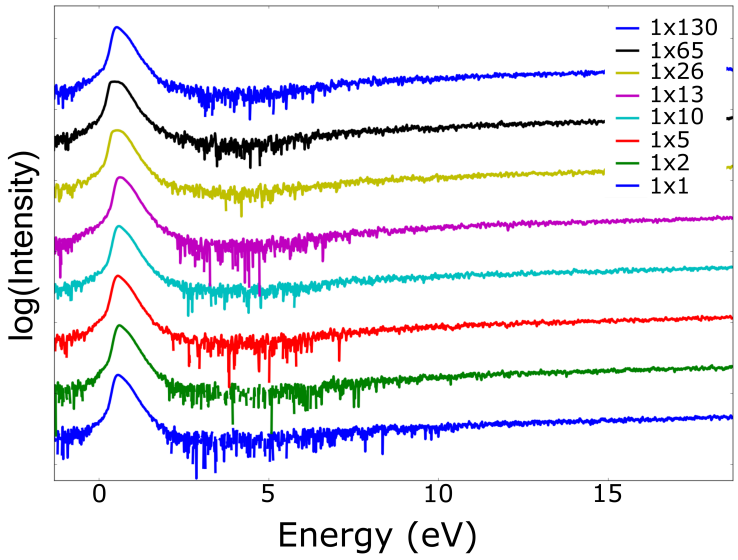

Figure 2.20: *Low-loss EEL spectra obtained for different vertical binning parameters. CCD detector used here has a* 260*x*2048 *vertical and horizontal pixels [2]. The spectra shown here are obtained from single pixel read-out to 1x130 binning. The SNR is calculated for each spectrum and the results are shown in table 2.1.*

suitable to the experiment being carried out. For our low-loss acquisition the signal to noise ratio (SNR) is of vital importance as the spectral features we are examining, in comparison to the ZLP, are weak. Therefore a process of optimisation was carried out in order to best tune the spectrometer to meet the needs required in this thesis. Tuning for other characterisation methods (chemical mapping etc) would require different optimisation parameters which would need to be considered when acquiring data. Considered here is the optimisation of the CCD read out and its effect on the SNR. As shown in figure 2.20, a CCD is the detector used in the EEL spectrometer. This device is an indirect detector which relies on the incoming electron generating a photon in a scintillator which is then passed through an optical fibre and into a camera [71]. For the GIF used in this work (for

low-loss [2]) the camera has a 260×2048 (vertical x horizontal binning) which we will try to optimise for the best SNR possible in this system. SNR is calculated as

$$SNR = \frac{N}{\sigma}, \tag{2.16}$$

where N is the average number of primary electrons per energy channel, and σ is the signal standard deviation which consists of several components (Fano noise, shot noise, gain noise and read-out noise) [58, 71]. Here we considered the vertical binning and its effect on the SNR [2]. Increasing the binning value will increase the SNR as we are averaging the signal taken for a number of pixels, but it subsequently increases the acquisition time (as well as increasing the gain noise for higher doses) [71]. Therefore we had to find a balance point in the binning value used in order to optimise the EELS acquisition process. Shown in figure 2.20 is a stacked plot of each spectrum obtained for each binning setting, starting from 1x1 pixel binning (single pixel read-out) to 1×130 binning. From these spectra, the SNR was calculated using the data to the right of the ZLP (from 1 eV to 7eV), and the results are shown in table 2.1. The spectra in figure 2.20 have clear favourable binning set-ups which correspond to the low SNR values in table 2.1. The results show a decrease in SNR as the amount of pixels binned is increased, with 1x13 being an outlier in the dataset. However, a compromise has to be made between SNR and acquisition time. Therefore, throughout this thesis, a binning of 1x5 was used for each experiment, as this offered the best balance between the two.

	Binning							
	1x1	1x2	1x5	1x10	1x13	1x26	1x65	1x130
SNR ($\times 10^5$)	2.39	2.26	2.29	1.65	1.94	1.36	1.29	1.23

Table 2.1: *Calculation of SNR for each binning type for low-loss EELS.*

EELS Data Processing

The dataset acquired from EELS can be very large with a lot of information about different scattering events in the specimen. Scattering from plasmon generation within a sample, however, is dwarfed in intensity when compared to the very large ZLP (as shown in figure 2.17(a)). The surface plasmon energy loss range ($0.7-5$eV) also lies on the tail of the ZLP which complicates matters further. Therefore to extract the information needed to characterise the plasmonic properties we must process the data. Deconvolution is a known signal processing technique used to extract information and remove noise from recorded datasets based on a known distortion [72]. There are many methods of deconvolution based on the particular dataset but here we use the Richardson-Lucy deconvolution method, which has previously been shown to successfully extract plasmon signals from low-loss EELS datasets [73]. Another post-processing technique applied here is non-negative matrix factorisation, which is a decomposition technique used to extract individual plasmon excitations from deconvolved EELS datasets. Both of these processing techniques were applied to every experimental EELS data set shown throughout this thesis.

Richardson-Lucy Deconvolution

Deconvolution is a necessary step to obtain the true signal from the acquired data as there will be an inherent *blurring* of the data from the energy spread of the source. Many numerical methods have been applied to optical imaging in order to restore the true image that has been effect by defects such as blurring, an example of which was applied to the images taken by the Hubble telescope [74]. Richardson-Lucy deconvolution (RLD) has successfully been applied to such optical images, and was introduced as a method for improving energy resolution in EELS by Gloter *et al.* in reference [73]. RLD is an iterative process where the collected image is deconvolved with a point-spread function (PSF) which comes from the energy spread of the electron source, aberrations in the optical system mentioned above and energy spread in the CCD [73]. In this work, the PSF used is a reference spectrum obtained from an isolated section of $Si_3N_4$where there is no influence on spectrum from the plasmonics of the metallic structures being examined. This reference spectra will contain information about the energy spread of the source, lens aberrations etc. as well as energy spread from interactions with the substrate. We can consider the image equation for a recorded image given by

$$P_i = \sum_j \rho_{i,j} O_j, \tag{2.17}$$

where O_j is the de-blurred data at pixel j, P_i is the observed, blurred image seen at pixel i and $\rho_{i,j}$ is the PSF. This is a convolution of the unblurred image with a known PSF which can then be deconvolved using the Richardson-Lucy method. This iterative approach is

given by

$$O_j^{t+1} = O_j^t \sum_i \frac{P_i \rho_{i,j}}{\sum_j \rho_{i,j} O_j^t} \tag{2.18}$$

where t is the iteration number [75]. Figure 2.21 shows a typical RLD process being applied over the surface plasmon generation energy range. The raw (blue) data is deconvolved $t = 40$ times using the reference spectrum, resulting in the red spectrum with clear plasmon peaks.

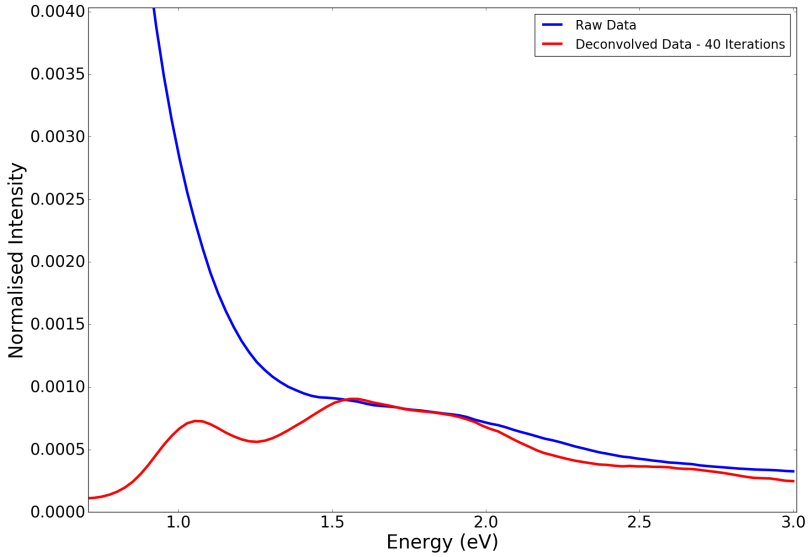

Figure 2.21: *An example of Richardson-Lucy deconvolution at the tail of the ZLP. After RLD, a number of spectral features are revealed.*

This deconvolution method has been extensively tested and proven successful in field of STEM EELS [51, 73], however care has to be taken when considering the iteration number. A typical number of 20-50 iterations is usually applied in the literature [48] but throughout this thesis, whenever experimental data has been shown, the number of

iterations has been found by testing the process. This testing process for the dataset shown in figure 2.21 is shown in figure 2.22. This figure shows the relationship between the FWHM of the ZLP and the Richardson-Lucy deconvolution iterations. Inset are snapshots of the logarithmic intensity energy loss spectra for the low-loss regime. Figure 2.22 shows a gradual decrease in FWHM as a function of iteration number, however, an increase in noise in the signal is also observed for the energy loss spectra. The introduced noise levels are relatively low in this example but this can vary for different datasets.

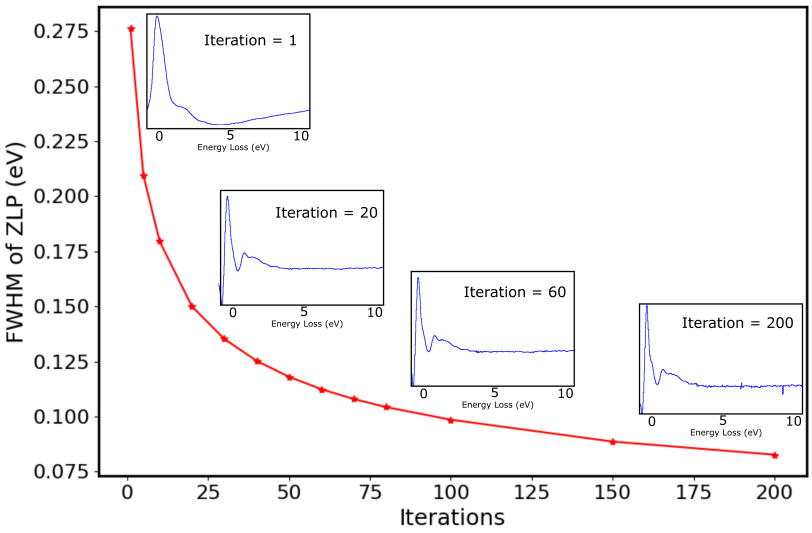

Figure 2.22: *FWHM of the ZLP as a function of Richardson-Lucy deconvolution iteration number. Snapshots of the logarithmic intensity energy loss spectra are given inset for Richardson-Lucy deconvolution iterations of 1,20, 60 and 200. FWHM of the ZLP decreases as a function of iteration number, however noise is introduced into the signal as a consequence, shown in the 60 and 200 iteration spectra.*

Non-negative Matrix Factorisation

After data has been deconvolved through the method given above, we can further process this dataset into individual features using non-negative matrix factorisation (NMF). This is a decomposition method which uses linear matrix factorisation to reconstruct a dataset based on partially learning individual components of the dataset. Here, however, we examined the individually decomposed datasets as they are representations of each plasmon mode generated within the structure. NMF decomposition is a machine learning technique which approximately factorises an $n \times m$ matrix V into two components: W and H via $V \approx WH$. In the case of our STEM EELS datasets, V is the 3D data cube (shown in figure 2.19) where n is the $x \times y$ spatial energy loss images and m is the energy vector of figure 2.19 (number of $x \times y$ images are present in the dataset). The columns of W can be thought of as the set of 'basis' images (in our case this is the individual EELS maps that make up the the full dataset) and the columns of H are the 'encodings', which tells us how to reconstruct an approximation of a pixel in V when combined with W [76]. The dimensions of W and H are $n \times r$ and $r \times m$, respectively, where r is known as the rank and, for our purpose, is defined as the number of estimated plasmon modes within the 3D data cube (selected by the information obtained from the corresponding simulations). Therefore, each column of W represents a basis image of the data cube which is a single plasmon mode and each row of H then represents the corresponding individual plasmon mode spectrum. Details of the learning algorithm are beyond the scope of this thesis and can be found in reference [77].

We highlight our application of this method with an example dataset shown in figure 2.21. In figure 2.23 we can have applied the NMF algorithm to the decomposed spec-

trum shown in figure 2.21. In figure 2.23(a) is the decomposed data after RLD given as the red spectrum and the resulting individual components of the spectrum, which we know are plasmon resonances [48]. These individual peaks have been fitted with a Lorentzian distribution [78] using a least-squares method in order to smooth out the resulting NMF spectra. Least squares method, simply put, is a fitting method which is based upon minimising the sum of the squares of the data from a given curve [79]. The boundaries for the fit are set manually as it is dataset-dependent (centre of the peak and half-width half-maximum values are set at sensible values in order for the optimisation process to complete) and the correctness of the fit is ensured by checking the standard deviations. This process of manually checking the fit is carried out for each experimental dataset presented in this thesis. In figure 2.23(b) we show the energy loss map for each peak found in 2.23(a), visualising the plasmon resonance for the examined structure (in this case it is an annular raindrop structure which will be discussed in chapter 3). Each of these clear distinct modes has been successfully found using an NMF algorithm. However one has to take care when carrying out this process as the algorithm requires an estimate of the number of plasmon modes generated within the energy range for a given geometry. At first glance this would appear to be a rather rough technique for identifying individual plasmon modes in STEM EELS dataset, but using the simulated results as a guide and experience in analysis this technique was incredibly useful for understanding the plasmonic properties of our fabricated samples. Throughout this thesis the experimental results will be presented as individual peaks (in a similar fashion to figure 2.23 but with no deconvolved spectrum) as this is a simple representation of the plasmon modes observed in the dataset.

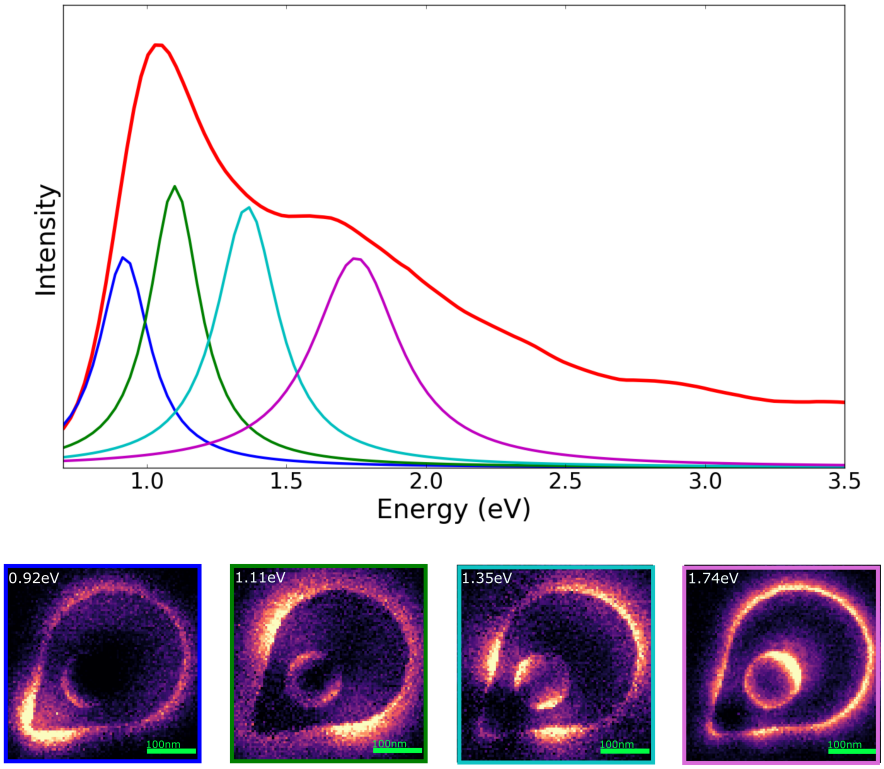

Figure 2.23: *NMF decomposition after RLD. Algorithm produced four individual spectra, fitted to a Lorentzian distribution and shown in (a). NMF decomposition also produces the corresponding 'basis' images for each spectra and are presented in (b), showing the spatial distribution of the plasmon modes.*

2.5 Scanning Electron Microscope & Focused Ion Beam

In chapter 4, we examine the environmental effects in the plasmonic properties of our NFTs. In order to do so, we must use a focused ion beam (FIB) to mill trenches through our samples - details of why this is necessary are given in chapter 4. The tool used through-

out the MCMP group for TEM sample preparation [80] and fabrication [81] was a Thermo Fischer Nova DualBeam instrument. This tool is equipped with a FIB as well as a scanning electron microscope, enabling the user to carry out nanoscale characterisation during a FIB process [68]. In this work, the tool was used to mill trenches through a Ta_2O_5 encapsulating layer as well as the Si_3N_4, in order to perform aloof beam EELS [58] for encapsulated NFTs. A simple schematic of the system used is shown in figure 2.24 where the tool is equipped with a Ga ion column, electron column, an omniprobe and a gas injection system (GIS). The omniprobe is used for manoeuvring TEM lamella that have been milled from a sample [80] and the GIS is used for ion or electron assisted deposition. A FEG electron source is used to illuminate the specimen with the beam being focused by electromagnetic lens system similar to a TEM, described above. The electrons are not transmitted in this system however, and images are formed from the secondary electrons and back-scattered electrons. This microscope is used to locate regions over which the milling process will take place, as well as a quick method of imaging a specimen in low magnification. A liquid metal ion source (LMIS) was used to generate Ga^+ ions by placing the W tip into a reservoir of Ga [68]. The extract voltage of 7000V is used to accelerate Ga^+ ions down the ion column towards the specimen, focused by a series of electrostatic lenses. These incident Ga^+ ions bombard the sample causing sputtering of the material as well as implantation into the specimen.

It has previously been shown that the implanted Ga^+ ions due to the FIB process has negligible effect on the plasmonics of structures fabricated using FIB [82]. The work presented in this reference also compares EBL and FIB fabrication process and reveals that the FIB structures exhibit a weaker plasmonic response when compared to the EBL method

due to the better quality of EBL sample (edge defects reduced damage in specimen etc), justifying the decision to use EBL as our chosen method. The sputter rate is determined by parameters such as the acceleration voltage in the ion column, beam current, dwell time and material being milled [68].

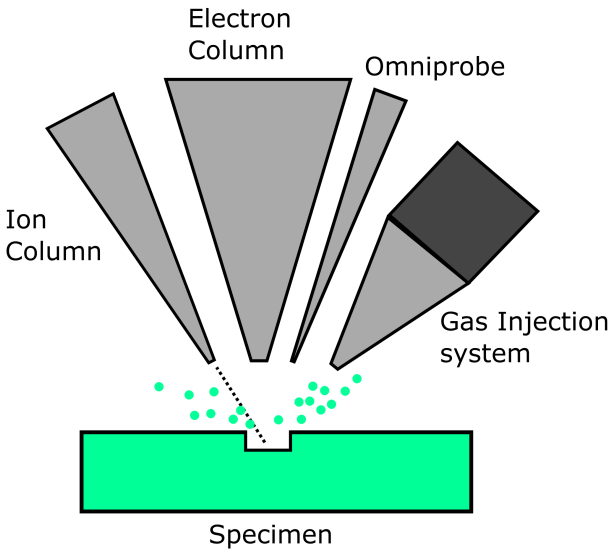

Figure 2.24: *A schematic of the Dual-Beam FIB/ SEM system used in chapter 4. The tool consists of an ion column, electron column, omniprobe and a gas injection system.*

2.6 Concluding Remarks

Here we have laid out the methods which we will use to examine the plasmonic properties of NFTs and are used through this thesis. Simulations are run through MNPBEM toolbox for which we have compared with the literature in order to confirm that the results obtained are realistic - ensuring confidence in the simulations carried out in the upcoming chapters. Substrate simulations matched the result seen in [44–46] and allowed us to understand

the effect Si_3N_4has on the plasmonic properties of the structures we examine. This in turn also allowed us to neglect them in simulations throughout this thesis (unless stated otherwise) due to the computational cost of its inclusion. Resulting energy loss maps from symmetric geometries have also been considered here, showing similarities in the distributions, and cementing the need to marry these results with corresponding charge distributions. Pairing of the two will be carried out throughout this thesis. Experimental work carried out here begins with electron beam lithography, where a lot of time has been spent optimising the fabrication process. Steps in the fabrication process were tested, such as EBL dose, to create samples capable of being examined by EELS. Fabrication of NFTs directly onto DENS heating chips was laboured over but, due to time constraints, samples created were not able to be examined using EELS. The JEOL ARM 200F STEM used throughout this thesis, in conjunction with EELS, to examine the spatial distribution of plasmon resonances for a NFT structure. Acquisition and data processing methods described above are used throughout this thesis in order to map plasmon resonances.

CHAPTER 3

PLASMONIC NEAR FIELD TRANSDUCERS

3.1 Abstract

In this chapter we examine the plasmonic properties of prototypical near field transducers using simulated and experimental electron energy loss results. To begin, we examine the properties of these NFT geometries using Scanning Transmission Electron Microscopy with Electron Energy Loss Spectroscopy (STEM EELS). We tested two geometries which are known for their nanofocusing abilities [83], showing that both structures have similar plasmonic response. We have also examined *annular* nanostructures as viable NFT designs, testing the tuning capabilities of the plasmonic properties both energetically and spatially. Tunability of NFTs plasmonic properties is highly desirable and has attracted

a lot of interest and research. We present annular nanodisk results through both simulations and experimental STEM EELS data showing that we are able to tune the resonances within certain energy limits. Energetic tuning was carried out by gradually increasing the diameter of the hole, showing a tunable window of 0.33 eV (corresponding to a redshift of 400 nm in coupled electromagnetic radiation), which is comparable to other tuning methods [84]. We then displace the hole within the structure, breaking the symmetry, in order to pin the resonances to the edge closest to the hole, which was successfully shown in both simulation and experiment. This chapter concludes with applying the annular model to a more realistic NFT geometry. From solid, to annular, to an annular geometry where the hole is displaced towards the apex of the structure, we see a tunable window of 0.3 eV and an accentuation of the resonances. We also see an increase in the intensity of the optically bright mode for the annular nanostructure at the region where we have displaced the hole, furthering the argument that this model is highly applicable to nanofocusing applications.

3.2 Nanolollipop & Nanoraindrop NFTs

Plasmonic NFTs play a pivotal role in the physical capabilities of HAMR devices and have been at the forefront of research for a number of years. As mentioned in section 1.2, one of the key aspects which defines the plasmonic properties of a nanoelement is the geometry of the particle. This creates a wide scope of variability to tune the plasmonics and has been extensively studied throughout the literature, a comprehensive description of which is given in references [20,21,83] where the authors present a multitude of NFT geometries and their individual applications. The majority of these studies has been carried out using

optical excitations as this method gives insight into the coupling between the source and the device in a HAMR device. However, we know this experimental technique does not offer full insight into the plasmonic properties of the NFT, with information such as plasmon resonance distribution and higher order dark energy modes being inaccessible. Here, we used simulated and experimental STEM EELS as a means of examination in order to energetically and spatial resolve the optically bright and dark modes and to assess the impact of practical aspects including geometrical imperfections on the NFT response. This experimental method allowed us to examine the plasmonic properties of HAMR NFTs in more detail than has previously been done and is one of the first examples of studying HAMR NFTs with STEM EELS.

For HAMR, NFTs are coupled to laser light and heating areas on the order of tens of nanometers in size [20]. Therefore the design of such a device requires a large body (for coupling) and a small protrusion (to focus the plasmon mode) in order to fulfil its role. We carry out this study on two geometries here termed 'nanolollipops' and 'nanoraindrops'. The structures are similar in design and schematics are given inset in figure 3.3(a), both having a wide circular body to couple with incident optical radiation, then a short protrusion that exploits the lightning rod effect [85]: focusing the radiation into a nanometric spot. The difference is in the shape of the protrusion. Nanolollipops, as described in references [85,86], have a concave tapered end in comparison to the nanoraindrop which comes to a point with a flat edge. This distinction could potentially result in different behaviours in harsh environments which is presented in chapter 4. Both of these structures are viable NFT geometries, with the former commonly found in the patents owned by Seagate Technologies and competitors [87–89].

3.2.1 Simulations

To begin, we simulated nanolollipop geometries, as described in section 2.1, with increasing stem length as a preliminary examination of the effect the protrusion has on the plasmonics. A number of nanostructures were created, beginning with a nanodisk and then a rectangular protrusion was added. This protrusion was gradually increased in length, transitioning from a disk element to a structure resembling a rod-like structure. This transition can be seen in figure 3.1. Au nanostructures of thickness 25 nm were created with the circular end of the lollipop kept at a diameter of 200 nm. This diameter was chosen due to the proposed NFT designs found in the patents [87–89] as well as guidance from Seagate Technologies. Calculations carried out in this section were performed taking nanostructures to be in vacuum (i.e. without a surrounding dielectric) in order to reduce the computational time. Substrate effects are shown in section 2.1 where a redshift in energy is observed due to the out-of-plane the coupling between the metal-substrate interface and the metal-vacuum face [44, 46]. Simulations are presented in a similar fashion to the results shown section 2.1 (figures 2.2 and 2.4) as an overall spectrum of the plasmon excitations in the structure.

Figure 3.1 shows the peak resonance energies for four observable modes: dipole, quadrupole, hexapole, and breathing mode as a function of increasing stem-length. The energies for all but the breathing mode gradually decrease with the increase in stem-length. Each of these modes were assigned through electron energy loss maps and charge distribution calculations, using the methodology described in section 2.1. Changing the symmetry, from disk to lollipop, creates mode splitting in the plasmon resonance as they lose their degeneracy [41]. This loss of degeneracy therefore means a redshift in energy as the path-

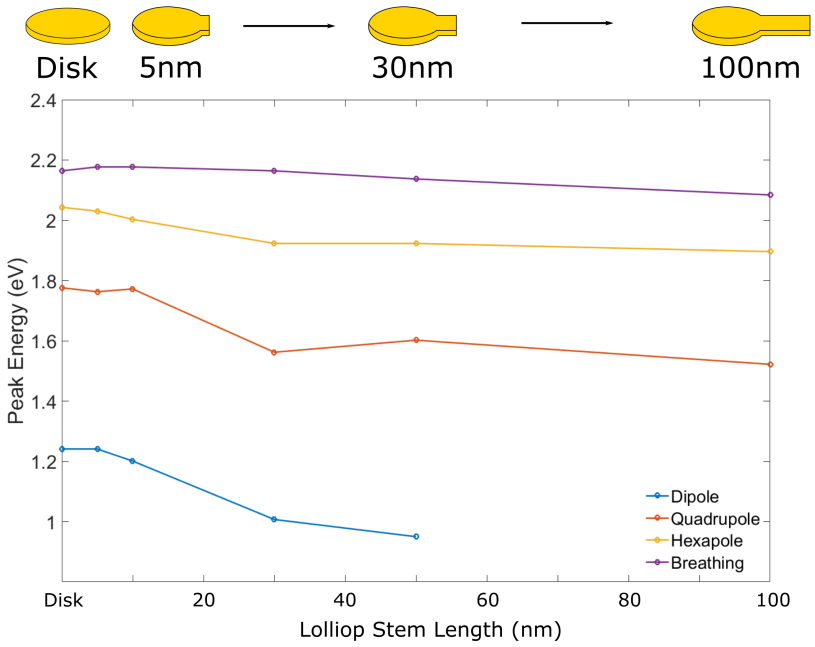

Figure 3.1: *Simulated peak energy loss results for nanostructures ranging from a disk geometry to a lollipop with increasing stem length. Each mode decreases in energy (i.e. redshift) as a function of this transition as a consequence of increasing the path length between the opposing charges.*

length between opposing charges increases. This could potentially be used as a method of tuning, however the tunable window (for the optically bright dipole mode) shown here is small, 0.23 eV.

For HAMR applications there are a number of disclosed geometries as given in reference [83] (bow-tie structures, 'E' geometry NFTs etc), as well as a number of geometries in patents. The basis of the work in this chapter will focus on the two simple geometries named above, nanoraindrops and nanolollipops. Therefore, in order to compare both structures as viable NFT geometries, we simulated the plasmonic response of two nanostructures with similar dimensions. The nanoraindrop's major and minor axes are 400 nm

and 500 nm respectively, whilst the nanolollipop has main body diameter of 400 nm with a stem length of 50 nm. These dimensions are larger than the models simulated above, and were chosen due to the size of the fabricated NFTs given in section 2.2 in order to make a more comprehensive comparison. A number of impact points are set across the structure and summed to give an overall spectrum for the device, just as before. Electron energy loss is then simulated over these structures and each observable mode is mapped. Figure 3.2(a) shows the calculated EELS spectra for both particles with their corresponding energy loss maps and charge distributions shown in figure 3.2(b). As described in section 2.1, each energy loss spectrum and map are normalised to the maximum value in the spectrum. However, in figure 3.2 we show multiple spectra. Therefore in figure 3.2 and throughout the rest of the thesis, each spectrum in a figure is normalised between the maximum and minimum of all the spectra in order to make a comparison between them. Charge distributions are normalised to values between -1 and 1.

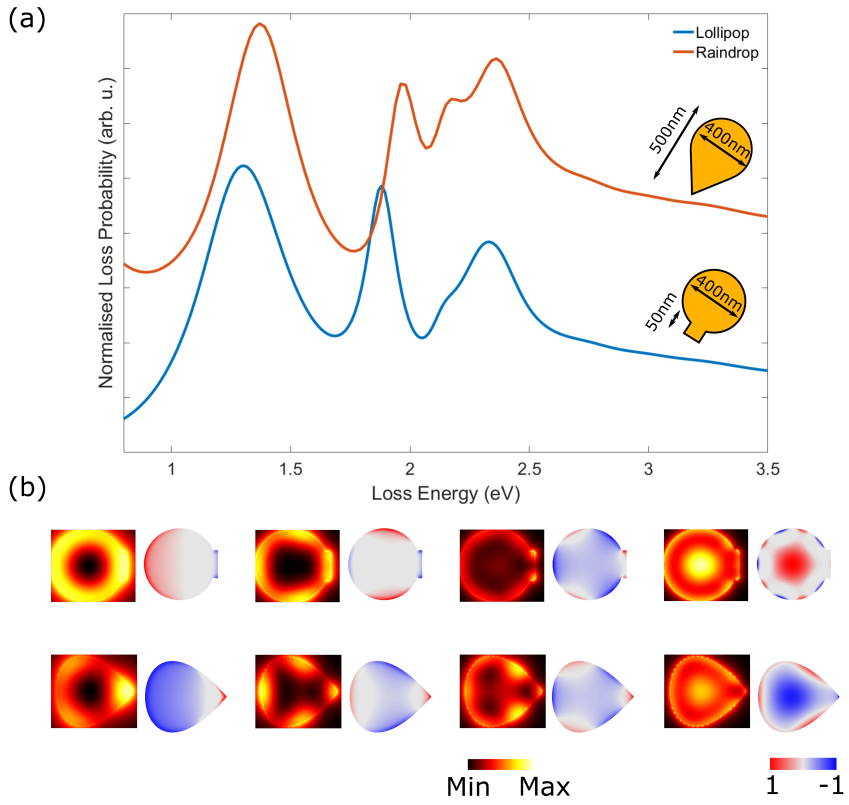

Figure 3.2: *(a) Simulated energy loss spectra for both a nanolollipop (blue) and a nanoraindrop (orange), with four observable peaks shown for both. Nanoraindrop major and minor axes of* 500*nm and* 400*nm respectively. Nanolollipop has a main body diameter of* 400*nm with stem length of* 50*nm. (b) The corresponding energy loss maps for each resonance peak which shows that the nodule of both structures accentuates the plasmon mode at that region.*

In comparing the peaks in each spectrum shown in figure 3.2(a) it is clear to see that both nanostructures have similar plasmonic resonances. The charge distributions shown in figure 3.2(b) indicate that the modes observed for both nanostructures (increasing in energy) are a dipole, quadrupole, hexupole and breathing mode. The first observable mode in each geometry is the dipole mode (optically bright mode) resonating at 1.41 eV for

the nanoraindrop compared to the nanolollipop's 1.37 eV. Energy loss maps and charge distributions of the dipole modes show that the intensity of the resonances at the tip of these structures. For the nanoraindrop the majority of the intensity in the energy loss map is concentrated to the apex, whereas the intensity distribution in the nanolollipop is homogeneous around the perimeter of the structure which is expected as its closer to a disk-like geometry. For HAMR applications there are advantages to both. The obvious advantage to the nanoraindrop is the concentration of the electric field to the tip of the structure, the main requirement of the NFT. However, the nanolollipop has a larger nodule with a more homogeneous resonance mode, which could lead to heating of a larger area using a more uniformly distributed electric field from the nodule of the NFT, resulting in more even heating if the bit which is desired. Both geometries have their advantages and hence were chosen to be examined here. Higher order modes for both geometries again have similar resonances energies.

The quadrupole mode in nanoraindrop and nanolollipop geometries resonate at energies 1.89 eV and 1.97 eV respectively with their energy maps and charge distributions shown in figure 3.2(b). Similar to the dipole charge distribution, the nanoraindrop quadrupole mode has a concentrated region at the apex of the structure. The hexapole mode is separated from the breathing mode in the raindrop whereas the modes are degenerate in the nanolollipop. In 3.2(b) the charge distribution and energy loss maps of the hexapole mode have very different distributions. The intensity distribution of the energy loss for the nanolollipop is large at the corners of the nodule which is also seen in the charge distributions, where the intensity for the distribution is in the corners of the lollipop geometry. The intense regions around the nodule of the nanolollipop are due to the sharp

edges of the lollipop structure where the resonances are pinned. Breathing modes for both the lollipop and raindrops resonate at similar energies, 2.43 eV and 2.44 eV respectively, however the intensity of the nanoraindrop is slightly increased. Energy loss maps and for this mode are very similar as the mode has intense regions in the centre of the nanostructure surface and the perimeter. The charge distributions in figure 3.2(b) show that the nanolollipop has a larger number of nodes on the perimeter of the structure compared to the nanaraindrop. The similarities between the two nanostructures gives us insight into the prototypical NFT geometries, highlighting the energetic and spatial plasmon resonances.

3.2.2 Experimental Results

HAMR NFTs are primarily studied using optical excitations to assess only the optically bright modes [20, 21]. However, it is well known that STEM EELS is a far more effective means to understand the plasmonic properties of nanostructures [10], offering the ability to spatially and energetically examine not only the optically bright modes but the dark modes; modes not excitable with electromagnetic waves [90]. In order then to correlate simulated and experimental results we can perform the same experimental analysis on our lithographically patterned nanostructures. Electron beam lithography was carried out as detailed in section 2.2 with 25 nm thick Au nanostructures created on top of Si_3N_4 membranes and examined using the JEOL ARM 200f. Figure 3.3 shows resulting plasmonic response of the fabricated nanolollipop and nanoraindrop geometries. Each peak in figure 3.3(a) was obtained through post processing methods, described in section 2.4, to extract distinct excitations from the strong zero loss peak. Energy loss maps for each peak are shown in figure 3.3(b). Normalisation for each spectrum and spectral image is carried

out using the intense ZLP of each acquisition, as described in section 2.4.

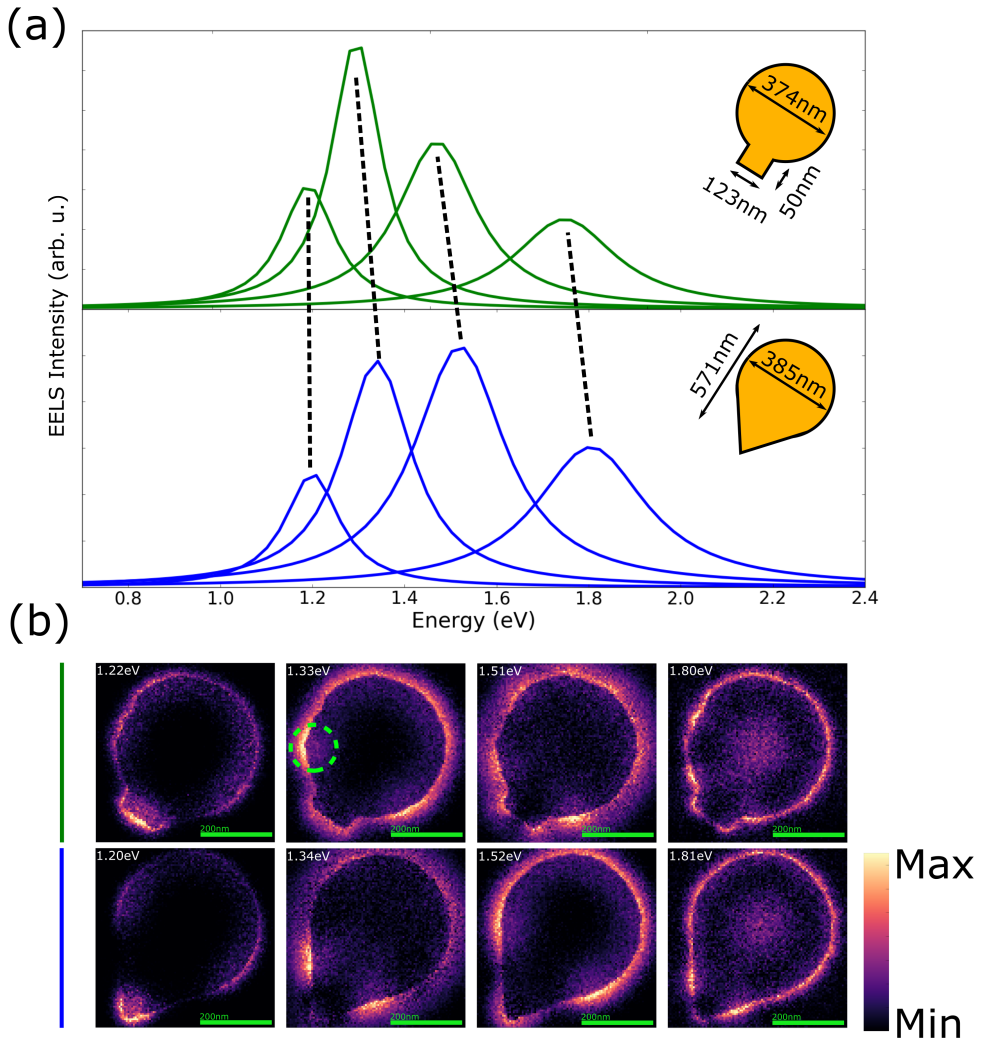

Figure 3.3: *STEM EELS data comparing the resolvable modes for a nanolollipop and nanoraindrop. (a) Individual peaks for each mode after post-acquisition analysis with the corresponding energy loss maps given in (b). From these maps we understand each mode to be, from lowest to higher energy, as: a dipole, two non-degenerate quadrupole modes, and a breathing mode. For the first nanolollipop quadrupole mode we have highlighted a deformation in the geometry to show the accentuation of the higher energy mode. Scale bars are* 200 *nm is size.*

The observable modes seen for both the nanolollipop and nanoraindrop in figure 3.3(a) are (ordered in increasing peak energy) a dipole mode, two non-degenerate quadrupole modes, and the breathing mode of the particles. There is a blueshift in energy for the two quadrupole and breathing modes when we compare the lollipop to the raindrop. The dipole has a redshift of 0.02 eV. The intensity for the dipole mode for both particles is less than that of the quadrupole modes. Thus, energy will be lost to the quadrupole mode as the dipole mode is excited and the larger intensity of the quadrupole mode means more energy will be lost when it is excited [91]. Examining the spatial distribution of the energy losses for each peak given in figure 3.3(b), we can see there are some similarities in the configuration of the modes. However, there are some slight differences in the energies of these modes. The effect geometric imperfections has on the resonances is illustrated in figure 3.3(b), where defect at the edge of the structure is highlighted in the first quadrupole mode in figure 3.3. This mode shows a clear accentuation of the energy intensity at this defect with the energy loss map peaking at this point. However it is worth noting that the imperfection due to the fabrication process does not effect the resonance distribution of the dipole mode, meaning that the optically active mode will not be drastically altered due to this type of imperfection. We have highlighted a deformation of the fabrication in the first quadrupole mode of the nanolollipop in figure 3.3(b). This mode shows a high intensity at the point but this is not present in the dipole mode. This is due to the position of the deformation which does not effect the dipole mode. Therefore, in this particular sample, the imperfect geometry does not effect the dipole mode, but does play some role in defining the higher energy modes. If the highlighted defect was positioned in the region of the dipole mode however, one would expect that the resonance would be pinned in a similar

manner. We have shown here the ability to spatially and energetically map a multitude of plasmon modes using STEM EELS for HAMR NFT designs. Experimentally showing the spatial distributions of the plasmon resonances for viable HAMR NFTs provides new insight to the field (this is one of the first examples of applying this experimental method to the field of HAMR NFT studies), whilst modelling gives us a better understanding of the higher order modes within the structures.

To continue this further and to fully compare the spatial distributions of the plasmon resonances within a number of NFT geometries we examined the electron energy loss maps for each resolved mode. We look at four geometries: a nanoraindrop, and three nanolollipops with increasing stem length. The energy loss maps of figure 3.3 are shown here in order to make a comprehensive comparison of the energy loss distributions of the NFTs. Figure 3.4 shows the energy loss maps for each of the geometries with the dimensions of each respective NFT given inset. Figure 3.4 is aligned energetically from left to right with each resonance energy given. Each mode here has been resolved from the raw data as described in section 2.4.

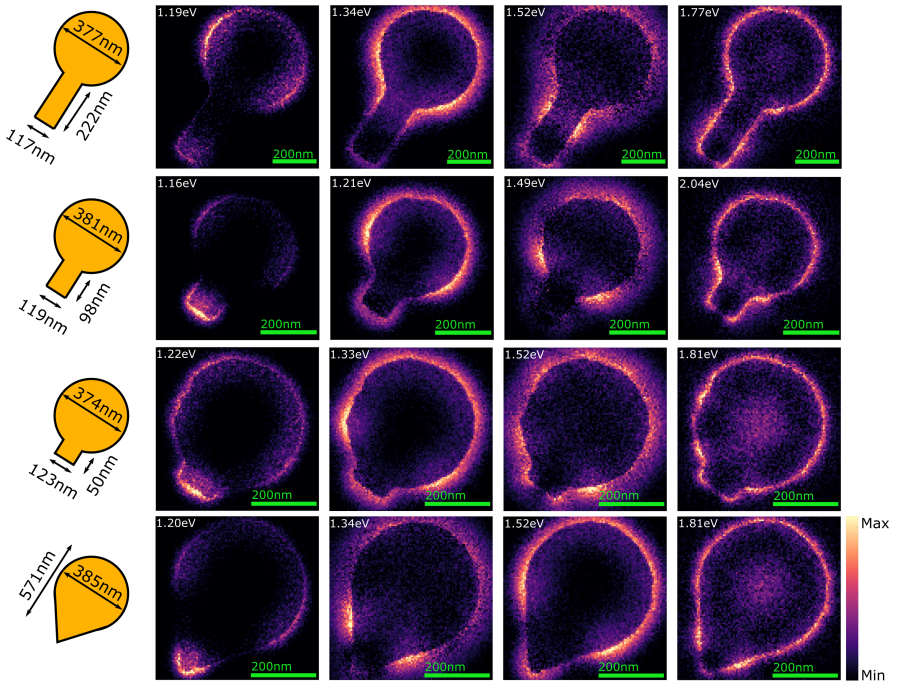

Figure 3.4: *Electron energy loss maps for a number of different geometries. From top to bottom: Long, middle, and short stem nanolollipops, with a nanoraindrop at the bottom. Each of the rows are aligned energetically from left to right. Dimensions of each NFT are given schematically.*

The spatial distribution of the energy loss shows us the effect of increasing the peg length of the lollipop. For each of the NFTs examined there are four distinct resonance modes resolved and shown in figure 3.4. The first column in figure 3.4 shows the dipole mode for each of the NFT geometries. As expected, each of the resonance distributions has an intense region around the apex of the structure, a necessary attribute for HAMR. The relationship between the resonance energy and the stem length is not the same as shown in figure 3.1 where we see a gradual decrease. This is due to the size discrepancies in the disk-body of the lollipops created during the imperfect fabrication process. It can also be

seen in figure 3.4 that the disk-body is slightly more elliptical in the axis perpendicular to the protrusion (more noticeable in the long-stem nanolollipop). This is another unwanted feature caused by the fabrication process but we expect that it has minimal effect on the plasmonic properties of the NFTs and is ignored here. Energy loss maps of the second and third column which, from figure 3.3 we understand to be two degenerate quadrupole modes for the nanoraindrop and nanolollipop with the shortest stem, show differences between each of the structures. The second map for the middle and long stem length nanolollipops show a similar resonance distribution. The third mode for the longest stem lollipop shows rod-like resonance similar to that seen in reference [92] with an intense region in the middle of the stem. The third mode of the middle is a quadrupole mode with a weak region of intensity at the stem. The highest energy mode in each of the maps is a breathing mode emanating from the centre outwards, where we see discrepancies in the energy trend not seen in figure 3.1 due to the fabrication differences. The results shown in figure 3.4 provide insight into the resonances of viable NFT geometries. With respect to the proposed NFTs in references [20, 83], our understanding is that a shorter protrusion from a larger body is more appropriate due to thermal effects such as dewetting which is explored in chapter 4. However it was important to understand geometric dependencies of the plasmonic properties for the nanolollipop in order for us to gain a full picture of this NFT model.

3.3 Annular Plasmonic Nanostructures

3.3.1 Simulations

In this section we present an analysis of annular plasmonic nanoelements and test the tunability of this prototypical NFT model. We examine this both experimentally and through simulations for a number of geometries, starting with annular nanodisks and then testing annular NFT structures. Tunability by altering the geometry is a vastly studied area in the field of plasmonics, dictated by the application of the structure. The plasmon energies of cross and dagger geometries have been shown to be controllable by changing the length of the arms, which in turn changes the resonance energies of the optically bright modes [84]. Annular plasmonic nanostructures have been extensively examined as they are used in devices such as split ring resonators. Gold nanorings have been studied using optical excitation as a method for tuning and improving the plasmonic properties for nanoantenna applications [93]. Asymmetric nanorings have also been shown to accentuate the plasmon mode resonance [35], inspiring the work carried out in this chapter. However, in this work, we implement the annular model to viable NFT geometries (nanodisks and nanoraindrops) in order to increase the functionality of these nanostructures for HAMR applications. We consider two variables in our annular models: the hole diameter, and the eccentricity of the hole. The latter is used as a method of accentuating the modes spatially and the former can be used as a method of tuning the plasmonic resonance energies and will be the starting point of this section. To begin with, simple Au nanodisk structures were modelled in MNPBEM with an outer diameter of 380 nm, thickness of 25 nm. The substrate layer was omitted in these simulations due to the computational time being vastly increased, but it

is expected to result in a blueshift the plasmon energy of the simulated results when compared to the experimental. This is described in section 2.1. We then placed a hole into the centre of the particle with a diameter 20 nm and gradually increased the diameter to 280 nm in order to examine the effects on the resonances. These dimensions are used here and throughout to match the dimensions of the fabricated structures that we will examine further on, and are described in section 2.2. Figure 3.5 shows the resulting simulated energy loss calculations for increasing inner diameter size, descriptions of which are described in section 2.1.

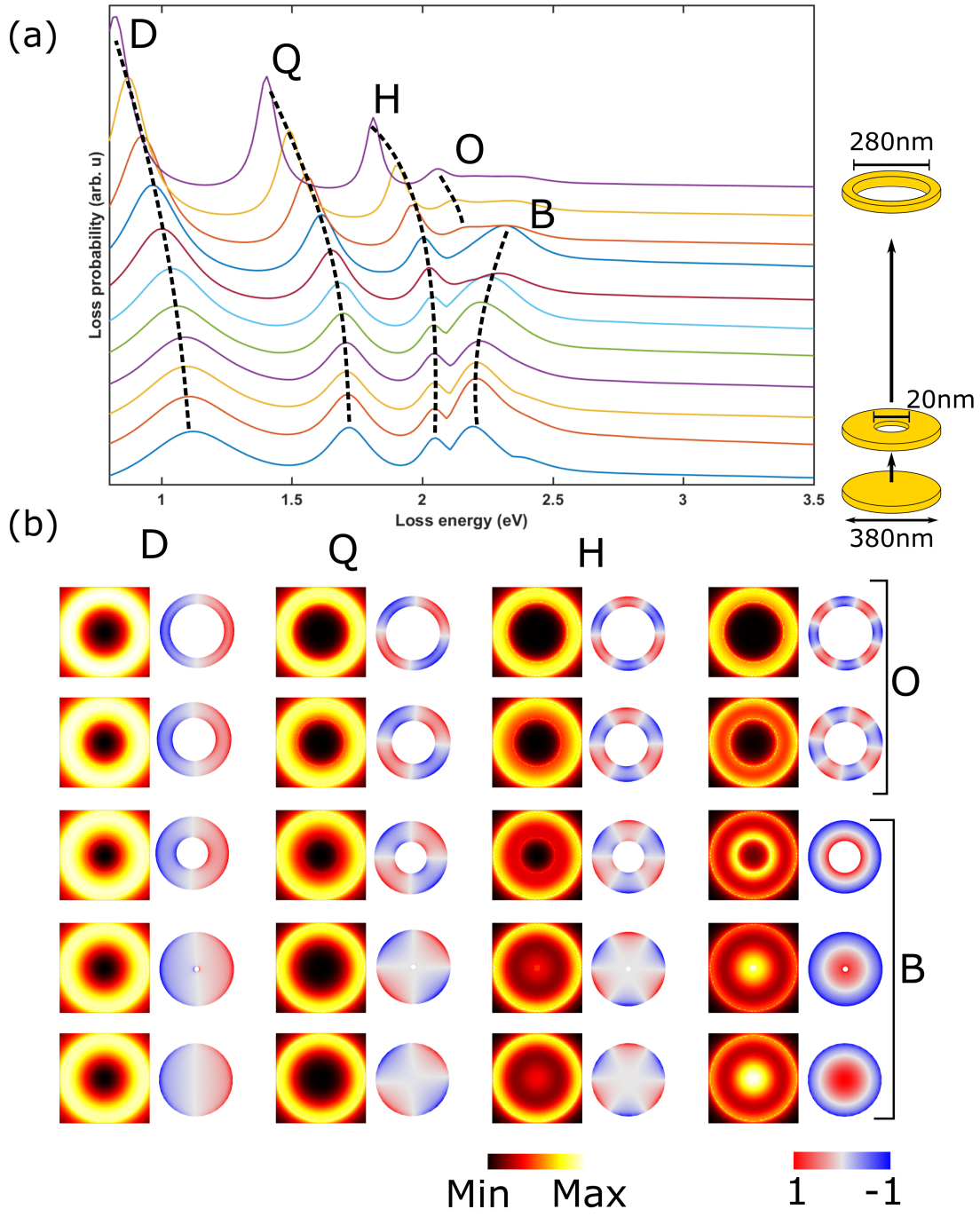

Figure 3.5: *(a) Simulated energy loss spectra for annular nanodisks, starting (bottom trace) with a complete disk and incorporating a hole on increasing diameter (upper traces). Dimensions of the nanodisks are shown schematically to the right. Hole diameter increases from* 20 *nm to* 280*nm. (b) The corresponding energy loss maps and charge distributions. The distribution as a function of inner diameter shows a clear decrease in resonance energy for each peak. The breathing mode is excited for each nanodisk until it is no longer energetically feasible to be generated, and an octapole mode is observed.*

As before, each spectrum produced by each impact point is summed to give an overall spectrum for the resonances of the structure. Figure 3.5 shows the resulting EELS simulations for a number of annular nanodisks, where figure 3.5(a) shows the summed spectrum for a number of impact points, increasing in inner diameter from bottom to top, and figure 3.5(b) shows the energy loss maps (left figure in each rows) and charge distribution (right figure in each pair) for each corresponding peaks. Moving from the bottom to top through the spectra, we show the results for a solid nanodisk, then an annular structure with an inner diameter for 28 nm, which gradually increases to 280 nm for successive spectra. In each spectrum we resolve four distinct peaks. From the charge distributions in figure 3.5(b) we understand that the first three modes for each nanodisk are a dipole, quadrupole and hexapole mode. The highest energy mode changes from a breathing mode to an octupole mode when the hole diameter is greater than 196 nm. The first three modes follow a consistent redshift trend as the inner hole diameter is increased. In addition, there is also an increase in the intensity for each of the peaks, along with a decrease in the FWHM. We can conceptually understand by considering the charge separation illustrated in the charge plots in figure 3.5(b). A hole acts to physically separate charges and if positioned at a nodal position of the disk's charge distributions, can maintain the symmetry of the mode whilst increasing charge separation. When the separation of charge increases, the energy of the system decreases. From the work carried out in reference [94] we understand that the propagating wavevector k_s is related to the the ring diameter r by $k_s = n/r$ where n is the order of the mode. Therefore, in the frequency range we are examining and using the formulae defined in reference [94], we can relate the surface plasmon frequency

defined in section 1.2 through

$$k_s \approx \frac{\hbar\omega_s^2}{2\alpha_o E_F c}, \tag{3.1}$$

$$\omega_s \approx \sqrt{\frac{2n\alpha_o E_F c}{\hbar r}}, \tag{3.2}$$

$$\text{and } \omega_s \propto \sqrt{\frac{nE_F}{r}}, \tag{3.3}$$

where α_o is the fine structure constant which describes the interaction between the electromagnetic force and elementary particles [95], c is the speed of light in vacuum, $\hbar$ is Planck's constant and E_F is the Fermi energy. Therefore changing the radius from 100 nm to 200 nm we can calculate $\omega_s(r = 100nm)/\omega_s(r = 200\text{ nm})$ giving us a value of 1.41. From section 1.2 we know that $\omega_s \propto E$, hence we can compare the ratio of two dipole peak energies for radii 100 nm and 200 nm, and obtain a value of 1.21. To expand on this further, we have fitted the peak energy values for the dipole, quadrupole and hexapole modes to $\sqrt{r}$ in order to quantify how well the above relationship fits our simulated results. We carried out square-root fitting using the inbuilt curve fitting tool built into MATLAB which allowed us to compare the fit to the data and test the robustness of the fit. Figure 3.6 shows the dipole peak energies from figure 3.5(a) as a function of inner diameter ($2r$), as well as the resulting square-root fit. As can be seen in figure 3.6, the $\sqrt{r}$ fit does not fully explain the relationship between energy and inner diameter size. This is corroborated and quantified by the R^2 value obtained from the fit, which is statistical measure of how well a trend-line fits the data and ranges between 0 (a very bad fit) and 1 (a very good fit) [96]. The R^2 value for dipole mode trend shown in figure 3.6 is 0.72. We calculated this value for the quadrupole and hexapole mode trends (omitted from this thesis) as 0.58 and 0.33

respectively. Therefore the above approximation dictating the relationship between the plasmon energy partially fits our simulated energy loss results, however this is a simplified model relating the energy and the inner diameter of a nanoring and does not fully explain the nature of the relationship.

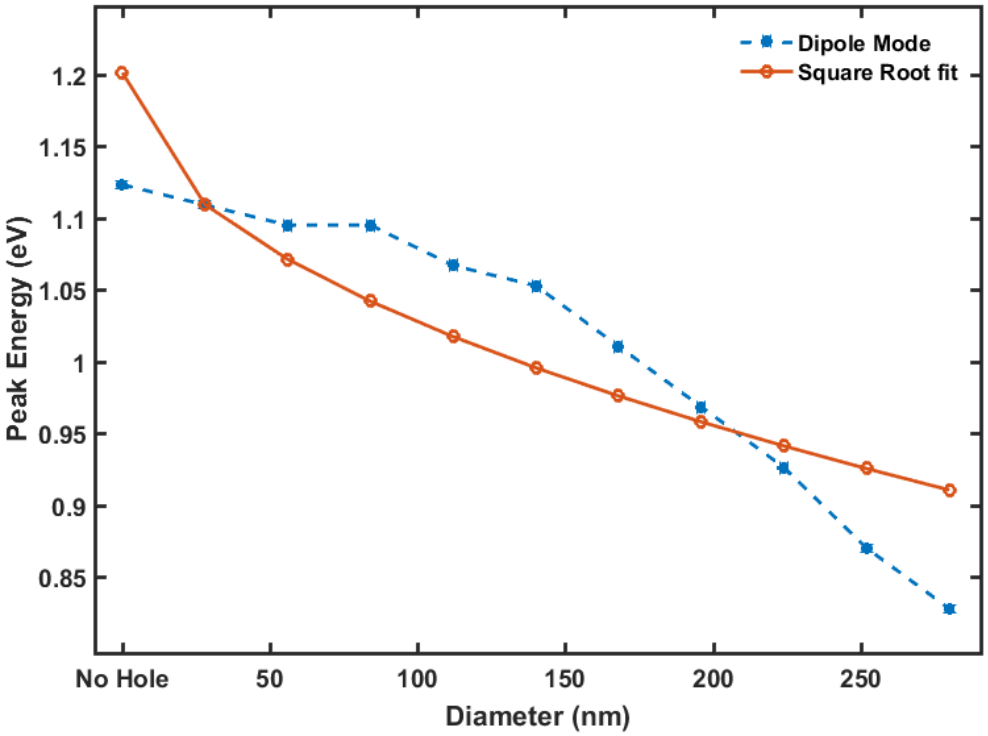

Figure 3.6: *Dipole peak energy values from figure 3.5 as a function of r, as a well the* $\sqrt{r}$ *fit.*

The higher energy breathing mode does not follow this trend, however. From the charger distributions shown in figure 3.5 we observe that there is a mode change at a hole diameter of 210nm which can explained by the path length between the positive and negative charges. For the breathing mode, it is clear to see that the nodal line between

the charges runs radially around the structure. As the hole diameter is increased in size, the distance between the two opposing charges decreases which leads to an increase in the energy needed to excited this mode, as seen in the highest energy peaks in each spectra in figure 3.5. At a hole diameter of 210 nm, the energy required to excite a breathing mode is too large, therefore the ocutpole mode is revealed. This simulated model showcases a viable tuning method for controlling the plasmonic resonances for NFTs. The overall change in energy for the optically bright dipole mode is roughly 0.2 eV. In comparison to the energy change seen when the size is increased, shown in [84] and in section 2.1, this is a relatively small change in energy. We will see experimentally that the change is much more considerable. In figure 3.5(a) there is a slight increase in loss probability intensity for the dipole mode as a function of increased inner diameter size. However for the higher order modes, the intensity does not follow any discernible trend.

Another potential for the annular model is the spatial enhancement of the plasmon modes. Here, using STEM EELS, we examined the effect of shifting the hole within the structure and how this would change the plasmon resonances. We expected to spatially confine the plasmon modes to the smallest edge, similar to the results shown in reference [35], allowing for the energy of the mode and evanescently decaying electric field to be enhanced at this point. Carrying on from our annular nanodisk structures, we gradually positioned the hole closer to the edge of the particle in order to pin the resonances to that edge. Here we examined the effect of shifting a hole of diameter 167 nm in a nanodisk, outer diameter 380 nm, towards the the edge of the particle. Again, these dimensions are chosen due to the fabricated samples seen in section 3.3.2 which would give a successful fabrication for these size of structures. The inner hole is shifted gradually by 90 nm

towards the edge of the particle.

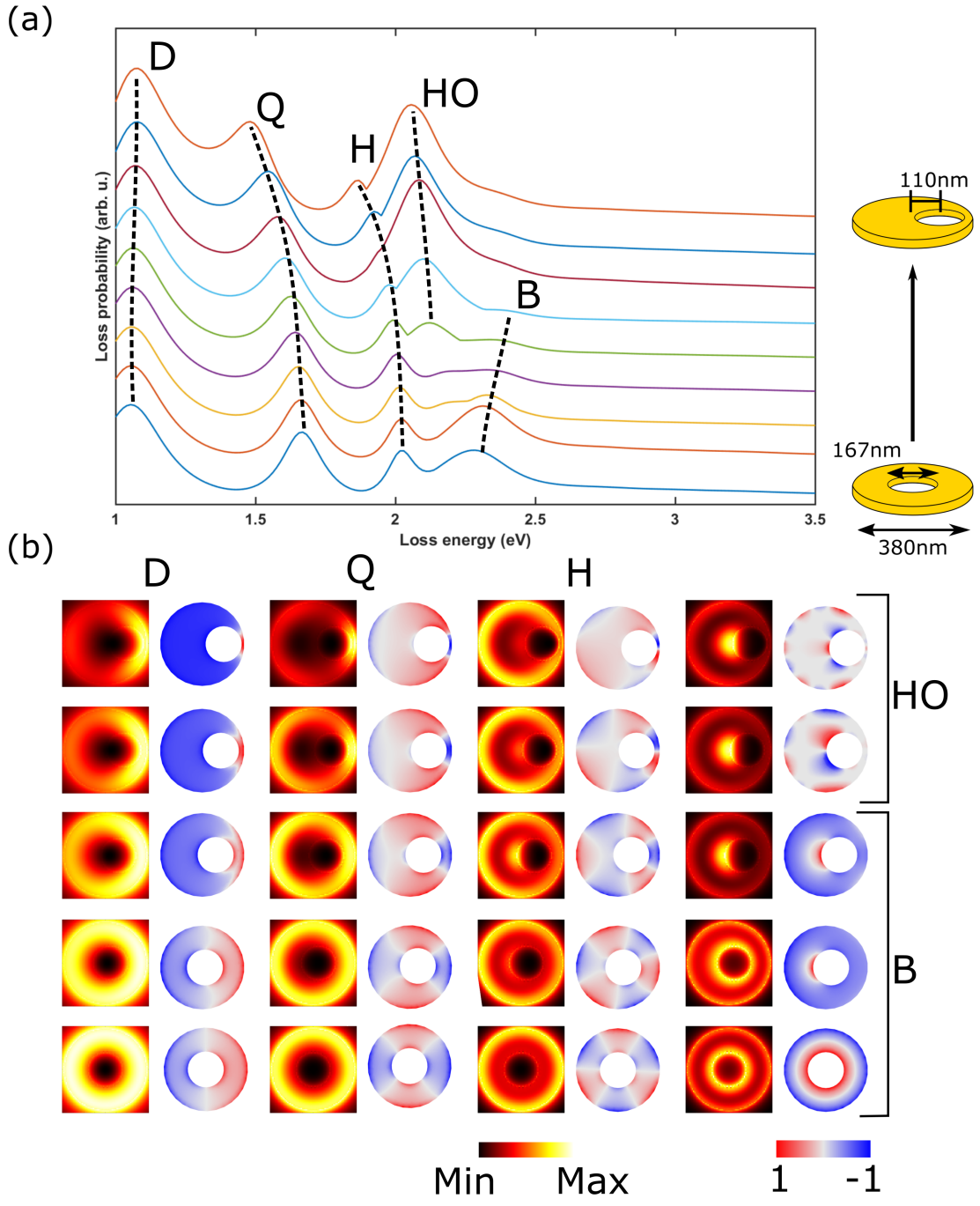

Figure 3.7: *Annular nanodisk structures with the hole being shifted within the particle. (a) The resulting spectra for a number nanodisks with increasing displacement of hole from bottom to top. (b) Corresponding energy loss maps for each peak in each spectrum arranged from lowest energy to highest going left to right. From lowest energy to highest (left to right in both (a) and (b)) the observable modes are a dipole, quadrupole, hexapole and breathing modes, where there is clear pinning of the resonances as the hole is displaced.*

Figure 3.7(a) shows the resulting spectra, with corresponding energy loss maps and charge distributions shown in figure 3.7(b), aligned energetically from left to right as before. The peaks observed in the spectra (in order of lowest energy to highest) are the dipole, quadrupole, hexapole, and breathing modes. If we examine the lowest energy mode, the dipole mode, in terms of shifting the hole further away from the centre, there is only a slight change in resonance energy (approximately 0.02 eV). The mode does not change in FWHM nor intensity, unlike the results presented in figure 3.5 (FWHM and intsenity simply calculated by cropping the datasets into individual peaks and manually obtaining these variables). However, we do observe the ability to accentuate the dipole resonance to the small edge, similar to the results presented in reference [94]. As the hole is shifted, the dipole mode is accentuated at the edge, as can be seen in the corresponding energy maps and charge distributions. However there is a change in the higher energy resonance modes. As the hole is shifted towards the edge of the particle, the energy of the quadrupole and hexapole modes decrease in a similar manner to that seen in figure 3.5. In the energy loss maps and charge distributions shown in the bottom panel of figure 3.7 we can see the spatial effect shifting the inner hole has on the plasmon modes. The dipole, quadrupole, and hexapole modes are concentrated to the edge closest to the hole. The breathing mode still emanates from the centre of the device but is clearly disrupted by shifting the hole. At the extreme, the highest energy mode transitions from a breathing mode to a resonance with a larger number of nodes as the hole is positioned closer to the edge.The confinement of the dipole mode to the small edge of the particle is what we expected; spatial pinning of the mode in order to concentrate the decaying electric field emitted as the mode is excited. In this simulated annular nanodisk model, we have shown that the resonance energies for

each mode can be controlled by the inner diameter size; a method for energetically tuning the plasmon modes. Continuing further, we have shown that the resonances can be pinned to an edge of the particle if we shift the hole away from the centre of the particle. In this nanodisk model, the optically bright dipole mode does not change in energy as we shift the hole away from the centre and towards the edge of the particle.

Expanding this prototypical model further, we wanted to examine the annular effect on nanostructures more applicable to NFT design. Annular nanoraindrops will be examined throughout this section, an initial description of which is given above. These structures have a tapered end in which there is a nanofocusing through the lightning rod effect [97]. Here we wanted to enhance the plasmonic properties by shifting the hole to the apex similar to the results shown in figure 3.7. The simulation model was built as before using isolated nanostructres in vacuum, assigned with a dielectric function. Au nanoraindrop structure was created with dimensions 400x300 nm and thickness 25 nm. The hole, diameter 120 nm, was positioned in the centre of the main body structure, and gradually shifted to the apex by 90 nm.

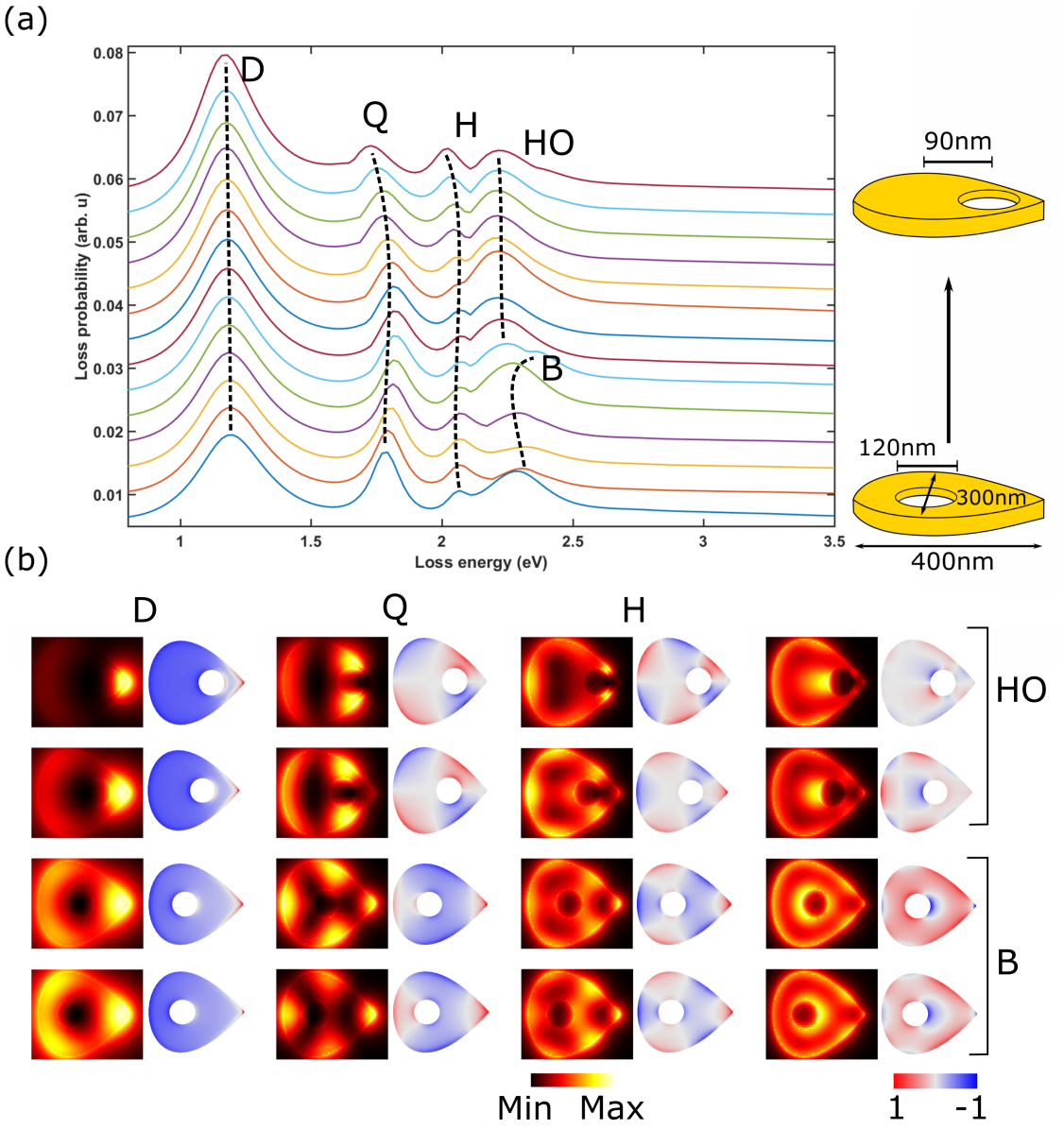

Figure 3.8: *(a) Electron energy loss spectra for annular nanoraindrop NFTs with the hole positioned centrally (bottom trace) and gradually shifted to* 90*nm towards the apex (top trace). Dimensions are given schematically to the right. (b) The corresponding energy maps and charge distribution for each observable resonance.*

Figure 3.8(a) shows the EELS spectra for the annular nanoraindrop structure as a function of hole displacement. No change is observed in the dipole energy as the hole is displaced from the centre to the apex of the device, which is consistent with the result seen for the nanodisk in figure 3.7. If we examine the energy loss maps and charge distributions in figure 3.8(b) we can observe the relationship between the distributions and the displacement of the hole. The lowest energy dipole mode shows a clear accentuation the mode towards the apex of the structure, similar to the results shown in figure 3.5. The concentration of the dipole mode for both the nanoraindrop and nanodisks indicates the promise of the annular model in applications such as HAMR. The higher energy quadrupole and hexapole modes also show some changes to their charge distribution. The breathing modes charge distribution in figure 3.8(b) change as the hole is displaced from the centre. The distributions are complex with a large number of nodes observed for each annular nanoraindrop model. We have tested this annular model for a more realistic NFT geometry through MNPBEM simulations and were able to successfully pin the resonances with a simple displacement of the hole.

Before we analysis the experimental results we first simulate the optical resonance of the nanoraindrop geometry in order to understand the effect this annular model is having on the dipole mode. This is important as the proposed annular model is expected to accentuate the electric field of the plasmon modes. Therefore we calculated the scattering cross section for x and y polarisations across the nanoraindrop geometries which shows us the resonance energies for the optically active modes. We chose the polarisation orientations by considering the geometry in the nanostructure. As the nanoraindrop is a 1-fold symmetric geometry, the polarisation axes were chosen to be parallel and perpendicular

to the symmetric axes (symmetric axis is the major axis of the geometry). This would allow us to excite the optically bright modes (dipole modes) along the symmetric axis. A description of these calculations is given in section 2.1 and in reference [37]. We examined three nanostructures which are termed a solid, annular-centred, and annular-shifted raindrop geometries with the dimension identical to the nanoraindrops given above, the optically bright dipole modes are calculated given the peak energies. After the optical excitations are calculated we can then spatially map the electric field both on the surface and surrounding the nanostructure. Figure 3.9 shows the simulated plasmon response to optical excitation. Scattering cross sections are given in figure 3.9(a) and show the peak energy for the optically active mode, figure 3.9(b) shows electric field maps for the surface of the structures for each of the given modes, with the E-field lines calculated on a plane 1 nm below the device. We have labelled each peak observed in figure 3.9(a) D_{AB} where A indicates the model (solid (s), annular-centred (ac) and annular-shifted (as)) and B is the polarisation direction (x and y).

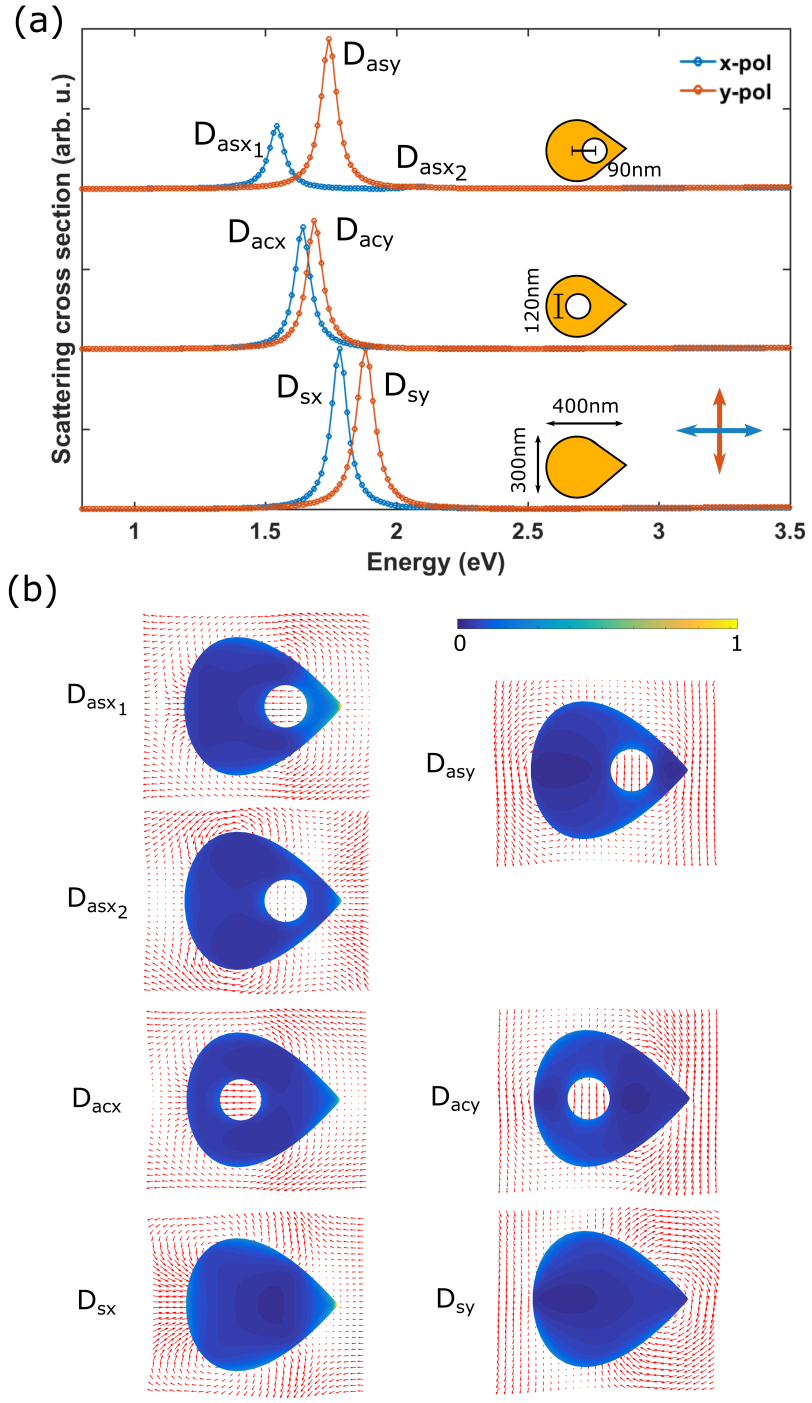

Figure 3.9: *Simulated optical response for three nanoraindrop geometries: solid, annular, and shifted annular. (a) The scattering cross section for the solid, annular-centred, and annular-shifted, from bottom to top respectively. Each spectrum has both x and y polarisation directions shown inset. Dimensions are given for each model. (b) The electric field distributions across the sample and the field lines* 1*nm below the nanoelements.*

In examining the trend of the blue peak in each spectrum there is a clear relationship between D_{sx}, D_{acx}, and D_{asx_1} as the energy gradually decreases from solid to annular-centred, and then to annular-shifted. This decrease in resonance energy does not corroborate the results observed in figure 3.8, where there is redshift in energy as the hole is positioned closer to the apex. We would expect that the dipole mode of the optical excitation would follow a similar relationship as the dipole mode in the EELS results [98], even though we excite different configurations of the dipole mode in the optical simulations due to the polarisation direction, as it is the same electron could resonance for the structure (see section 1.2). Later, as we go through the experimental results for the annular nanoraindrop structures, we do see a decrease in resonance energy of the dipole mode which indicates that there is an error in the STEM EELS simulations. Looking at the electric field maps of these modes as labelled in figure 3.9(b) we can see a clear resemblance between the x polarised electric field distribution. Each of the surface electric field distributions are normalised to the overall maximum of calculations in order to make a comparison between the field values. The peak electric field for each of the maps is generated at the apex of the structure as one would expect for a mode generated across the x-axes (major axis). In comparing each of the maps, the most intense field is given for the D_{asx_1}, the major axis mode for the annular shifted structure, as we expected from the simulated EELS maps. This confirms the expectation that the electric field of this mode is increased as we displace the hole from the centre of the structure to the apex.

Comparing the peaks energies for the y-polarisation modes (minor axes) we observe something interesting. Solid to annular-centred (mode D_{sy} and D_{acy} respectively) decreases in peak energy, and as we move from a centred to a shifted annular structure we see

an increase in energy (mode D_{asy}). The latter mode is the most intense peak in figure 3.9(a) and when we simulate the electric field for this mode we can see the majority of the intensity is generated at the edges closest to the hole. If we compare the resonance energy of this mode with the quadrupole mode in figure 3.8(a) as well as comparing both the e-filed and EELS maps we can say that as we shift the hole to the apex, we are optically activating the quadrupole mode. A similar result has also been shown in reference [35] where the authors couple the optically active quadrupole mode to a dipole mode of a smaller disk positioned within the hole of the annular nanodisk.

3.3.2 Experimental Results

Annular Nanodisks

We now examine the fabricated NFT structures to test this annular tuning model. To begin with a comparison between simulated and experimental models we first study an annular nanodisk structure with increasing inner diameter. Hole diameters of 77 nm, 167 nm, and 272 nm (measured using BF images of each of the sample) are examined in particles with outer diameter of 380 nm, along with a solid nanodisk structure. Some discrepancies between the outer diameters for each of the annular structures are due to the inaccuracies in the fabrication process which have been assessed in section 2.2. However, these effects should be negligible in comparison to the shifts caused by increasing the inner diameter. Imperfect geometries in the nanoparticle will also have an effect in the plasmonic resonances but these will be small and are ignored as well. Figure 3.10 (a) shows the STEM EELS data after post processing, described in section 2.4. Each peak in the spectra is an observable plasmon mode for the nanodisk structures which corresponds

to the energy loss maps given in figure 3.10(b), along with the charge distribution of the mode. Charge distributions were generated in MNPBEM using dimensions measured from STEM and matched to each map through their resonance energy and eigenvalue. Some discrepancies between the simulated and experimental plasmon energies are observed here due to the presence of a substrate and adhesion layer in the experimental data; omitted in the simulations (see section 2.1 for details).

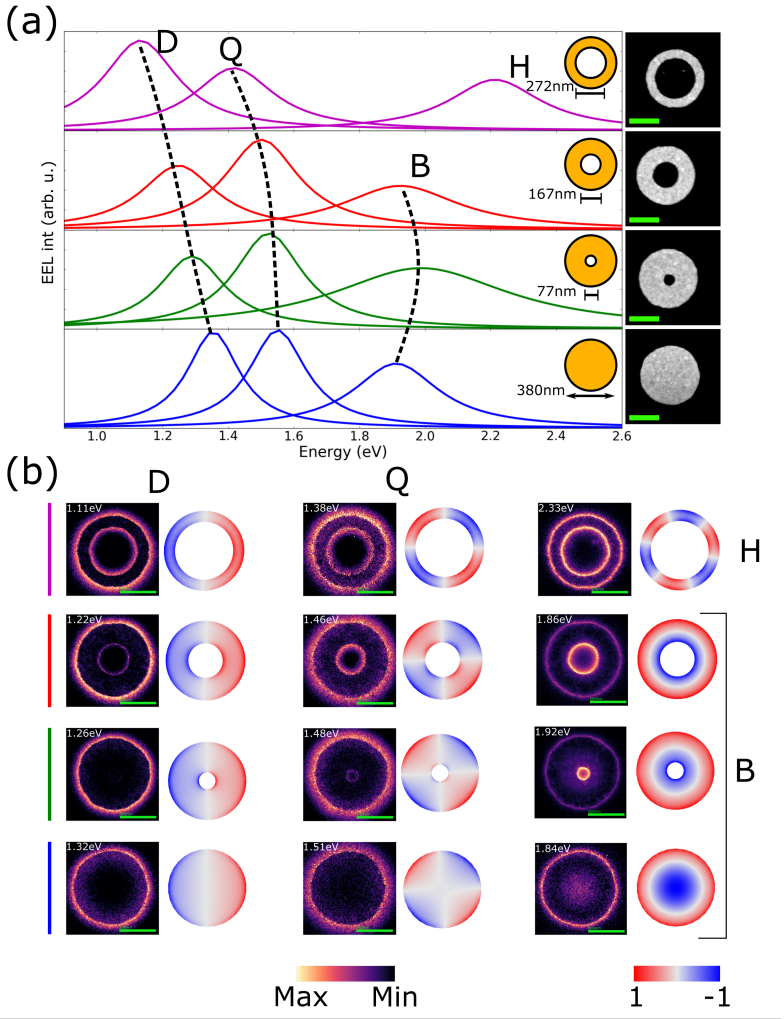

Figure 3.10: *(a) STEM EELS of a complete nanodisks (bottom trace) and incorporating a hole of increasing to a maximum diameter of* 167 *nm. Dimensions are given schematically to the right. (b)The corresponding energy loss map and simulated charge distribution pairs for each resolved peak with peak energy given inset. A decrease in energy is observed for the first two modes as a function increasing inner diameter as expected from the simulated results in 3.10. The highest energy mode does not follow a similar trend in energy however. We understand from the charge distributions that this mode changes from a breathing mode to a hexapole mode for the largest hole diameter .*

In figure 3.10(a) we can see the relationship between the inner diameter and the reso-

nance energy of the observable modes. Here we only observe three peak for each structure, one fewer than the simulated results shown in figure 3.5(a). This is due to the energy resolution of the experimental process described in section 2.4. The first two peaks in each spectrum are attributed to the dipole and quadrupole modes respectively. When a hole is introduced and the inner diameter is increased, there is a decrease in the resonance energies of the dipole and quadrupole modes. The highest energy mode in each spectrum has a different energy trend with this annular model, which increases in energy, decreases, and increases again as a function of increasing hole diameter. This does not match with the simulated breathing mode in section 3.3.1. In order to understand this, we must examine the charge distributions, more importantly the pathlength between opposing charges. As the hole is introduced the path length increases as there is a gap between the opposing charges, which increases as the hole diameter increases. Similar to the results presented in figure 3.5. Therefore, the energy needed to excite this mode *decreases*. As the inner diameter is increased, the pathlength increases resulting in further lowering of the energy of this excitation. The dipole and quadrupole mode energies fall off gradually as a function of inner hole diameter, allowing for some controllable tunability. The breathing modes (red peaks in each spectra) do not follow this trend. We again examine the charge distributions to understand this. Emanating from the centre outwards, as the hole is introduced and increased, the pathlength between the opposing charges also increases, requiring more energy to excite the mode. When the inner diameter is large enough (272 nm diameter), the energy needed is too much, resulting in a mode change to a hexupole mode. This confirms the result observed from our simulated model presented above however there is some discrepancy in the energy of this mode when compared to the simulated results.

This difference can be attributed to the presence of the substrate in the experimental results (presence of a substrate effects higher order modes more than dipole mode [48], see section 2.1) and imperfect geometric effects; roughness of the sample edges, structures etc. A discrepancy seen in the experimental data that is not seen in the simulations is the dipole mode of the smallest inner diameter. The energy loss maps shows an outer-only excitation - no intensity seen in the inner part of the particle. In this model we aim to *tune* the plasmonics by controlling the size of the hole and compare results to simulations. The difference in energy between the solid nanodisk and the annular structure with the largest inner diameter is 0.21 eV (corresponding to a redshift in EM radiation of 177 nm). The change in energy is consistent with that simulated in section 3.3.1. For applications like HAMR, this amount of tuning is enough to decrease the loss of the system by a substantial amount [85]. Energetic tuning of plasmonics for HAMR applications is aimed towards controlling and maintaining a dipole plasmon mode energy set by the wavelength of the incident excitation (see section 1.1.1). Here we have shown a tuning method through geometric manipulation which could be easily applied to HAMR NFTs.

We now turn to the tunability measured by displacing the hole from the centre of the nanodisk to one side of the structure, as modelled in section 3.3.2. Displacement of the hole within graphene nanodisks has been computationally calculated in [85] and the references therein. Being able to experimentally show this for Au annular plasmonic sturctures would show the real-world applicability of this model as an NFT design, in an ability of pinning the resonances to a desired position. Fabricated nanodisks with an inner hole diameter of 167 nm were used, and the hole was displaced by 60 nm, making the distance between the inner diameter and outer edge 56.5 nm measured using the corresponding

HAADF image. STEM EELS and post acquisition processing was applied just as before, as described in section 2.4. Figure 3.11(a) shows the spectra for each observable mode for both the centred (bottom) and shifted (top) annular structures. For each observable peak there is a corresponding energy loss map given in figure 3.11(b), with the associated charge distributions. Both nanostructures show three distinct modes have been resolved from the data: dipole mode (blue), quadrupole mode (green) and a breathing mode (red). We again do not observe the hexapole mode for the experimental results (seen in the simulated data shown in figure 3.7(a)) due to the energy resolution of the microscope. Comparing each of the peaks for centred and shifted hole structures there is a clear decrease in plasmon resonance energies for each mode.

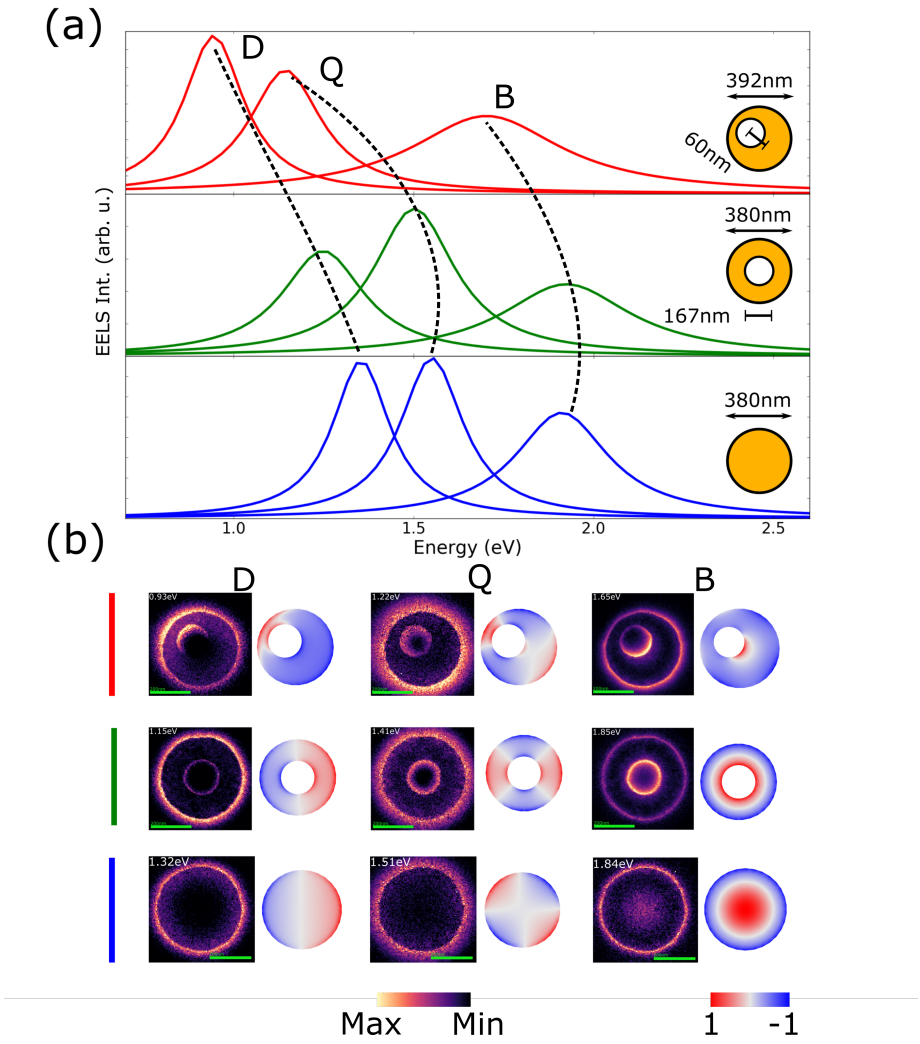

Figure 3.11: *(a) Electron energy loss spectra for three particles: solid nanodisk, annular nanodisk, and annular nanodisk where the hole is displaced by* 60 *nm edge of the device. Dimensions for each particle are given inset. (b) The corresponding energy loss maps and simulated charge distribution for each observable peak. There is a clear decrease in resonance energy as the hole is shifted, and a pinning of the optically bright dipole mode as well.*

The spectra shown in figure 3.11(a) indicate a change in energy as the hole is moved to

the edge of the particle. Each mode resolved here shifts by roughly 0.2 eV, with the intensity of the dipole mode being the dominant mode in the resonance landscape. Comparing the STEM EELS data with the simulations in 3.3.1 there are discrepancies in the two. The simulation model does not show any observable change in the dipole resonance energy, as a function of hole displacement, and the decrease in energy for the higher order modes is much more significant than observed experimentally. The latter may be attributed to proximal and distal hybridisation from the substrate-metal modes with the metal-vacuum [48], but the former may show the limitations in the calculated results obtained via MNPBEM. This red-shift in energy is 0.4 eV (a shift of 400 nm in wavelength - the difference between the highest and lowest dipole energy values in terms of wavelength). If this is consistent with the results shown for the annular nanoraindrops it will corroborate this model as a viable NFT design. Going back to the spectra show in figure 3.11 we also see an increase in intensity for the dipole mode, becoming the dominant mode in the spectra as the hole is displaced. This increase in intensity indicates an accentuation of the dipole mode, which is clearly seen in the corresponding energy loss maps in figure 3.11(b). The energy maps do, however, follow the same spatial enhancement when the inner hole is shifted. In comparing the two dipole modes, we can clearly see the spatial pinning of this mode to the small edge of the structure as the hole is shifted. The spectral images for the higher order modes shows results consistent with the energy loss maps seen in the simulated results. As the hole is displaced there is some shifting in the distribution of the plasmon resonances of the structure. Experimentally showing the ability of the spatial pinning provides insight into how useful this model can be as a method of electric field enhancement. Crescent shaped nanostructures have theoretically shown to enhance the electric field [99], but being able

to the experimentally show this within the limit of fabrication (small edge limitations described in section 2.2) is obviously significant. Tuning the plasmonics by 0.4 eV is clearly a great asset to have in applications like HAMR, and enhancing the resonances by hole displacement furthers this argument.

NFT annular nanoelements

We now examine the plasmonic properties of fabricated nanoraindrop geometries in order to explore the applicability of our annular model as a method of tuning for HAMR NFT geometries. Here we tested a three different nanoraindrop nanostructures: a solid particle, an annular raindrop, and an annular structure with the hole shifted towards the tapered end. Using STEM EELS we want to spatially and energetically resolve plasmon modes in order to understand the annular effect on the plasmonics, and testing the ability to accentuate the electric field of the optically bright dipole mode and corroborating the results obtained in the section 3.3.1. Figure 3.13(a) shows the resulting STEM EELS spectra for each resolvable mode in solid (blue), annular-centred (green), and annular-shifted (red). Figure 3.13(b) shows the corresponding energy loss maps and charge distributions for each resolved resonance.

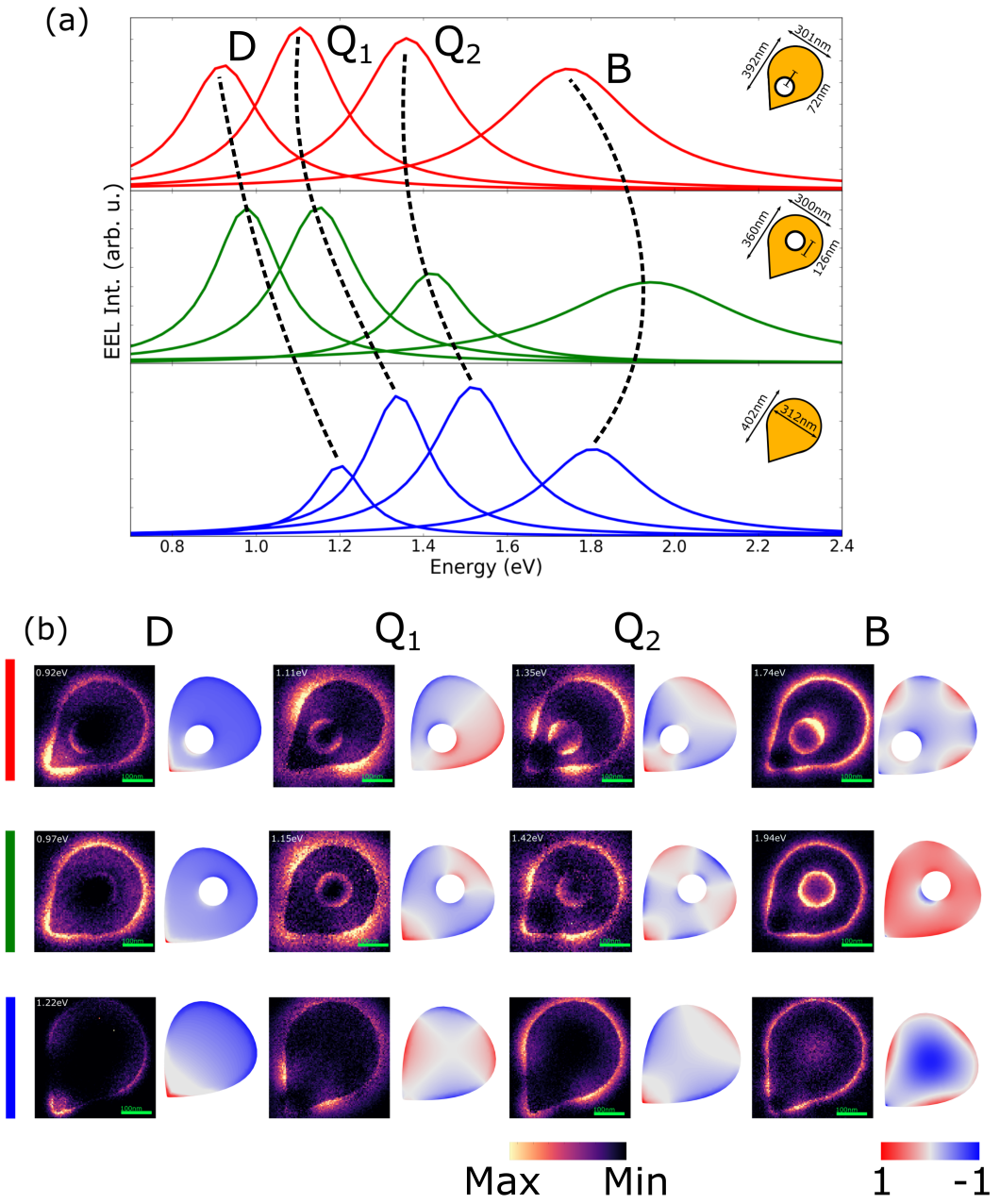

Figure 3.12: *STEM EELS spectra of three different nanoraindrop structures: a solid particle, raindrop with a centred hole and an annular raindrop with the hole shifted towards the apex. (a) The observable plasmon modes obtained through decomposition of experimental data. The results for the solid, annular, and annular with a shifted hole are given as the bottom, middle, and top spectra respectively. (b) Corresponding energy loss map and simulated charge distribution for each resonance.*

Examining figure 3.12 we resolve four modes for each of the nanoelements which we identify as: a dipole mode, two non-degenerate quadrupole modes, and a breathing mode. The energies of each dipole mode show a decrease when a hole structure is introduced, and a further reduction as the hole is shifted to the apex of the nanoelement. This decrease in energy by displacement was again not observed for the simulated model in section 3.3.1 but corroborates the relationship seen above for the experimental annular nanodisks. The total decrease in energy of the dipole mode from a solid nanoraindrop to an annular nanoraindrop with the hole shifted 90 nm towards the apex is 0.4 eV as seen in annular nanodisks results shown in figure 3.11. This tunable range is comparable to the energy shift observed using other methods such as extending the arms of a nanocross [84] or increasing the size of the structure by approximately 150 nm [50]. There is a gradual decrease in peak energies as the hole is introduced and then further when the hole is shifted towards the apex. These energy loss map results are in good agreement with the maps shown in figure 3.8(b). Examining the peak energies, energy loss maps and simulated charge distributions for the higher order modes we again see shifts in energy as we compare the solid and annular structures. The two non-degenerate quadrupole modes again show a decrease in energy as we go from a solid to an annular structure, and then shift the annular to the apex (0.25 and 0.21 eV for the lower and higher quadrupole modes respectively). The breathing mode increases in energy from solid to annular and again decreases in energy as we shift the hole. Again the discrepancies between the simulated and experimental results we understand that the differences in energy can be attributed to the substrate and the imperfect geometry of the nanostructure. The optically bright dipole mode is the most important mode for HAMR [21, 100], as it is the mode that couples with

the incident laser light. We have shown the viability of our tuning model to control the plasmon modes spatially and energetically. For this model to be completely useful, we must test the enhancement of the fabricated samples between a centred and shifted annular raindrop structure. Figure 3.13 shows the resolved dipole mode peaks from the STEM EELS data for all three structures as above, normalised to the intensity of the zeroloss peak I_o in order to compare the energy loss of each peak which will give a true representation of the mode intensity [62].

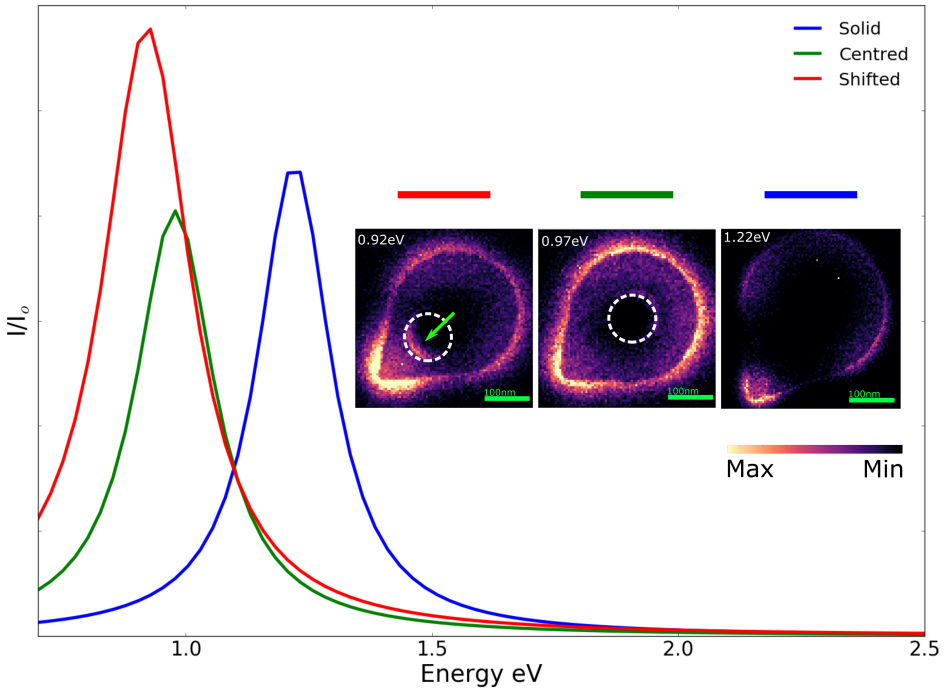

Figure 3.13: *Comparison for the optically bright dipole mode for the three nanoraindrop geometries.There is an increased intensity as the hole is shifted from the centre to the apex of the structure. Resonance maps are shown as an insert in this figure with clear pinning of excitation at the small edge of the shifted particle. This is a viable and usable method for accentuating and tuning plasmonic properties of nanoparticles.*

Figure 3.13 shows the effect on the dipole mode as we go from solid to annular, and from annular-centred to annular-shifted. To begin with we see a decrease in both energy and intensity when we go from solid to annular, which in terms of HAMR application would only be good for energetic tuning. The energy loss maps shown as insert gives insight into the loss of intensity, as the dipole resonance distribution is much more diffuse for the annular structure. However as we shift the hole towards the apex this changes quite drastically. Again we see a decrease in energy but we also observe an increase in intensity. This increase shows the accentuation of the energy loss and hence the electric field of the mode. The energy loss maps show a clear accentuation of the mode to the apex of the structure, exactly what is desirable for nanofocusing applications like HAMR. Here we have shown the applicability of our annular model as a method of both energetically and spatially tunning the plasmonic properties for this prototypical NFT design, both experimentally and through our simulation model. Here, the annular model has been applied to HAMR NFTs and examined using STEM EELS for the first time, showcasing the applicability of this model to accentuate the plasmonics and improve the functionality.

3.4 Conclusion

We have examined prototypical NFT geometries using STEM EELS and shown the capability of our annular model as a method of tuning plasmonic properties. Through both simulated and experimental data we revealed the similarities of the resonances for both viable NFT designs: nanoraindrops and nanolollipops. From these initial results we then explored the annular model in order to test the tunability, both energetically and spatially.

Beginning with a simple nanodisk structure, we examined the effect of increasing diameter of the inner hole, showing the ability to control the resonances within a 0.3 eV window (400 nm). By displacing the hole towards an edge of the structure, we have shown the ability to spatially tune the mode where the resonances are pinned. Applying this to a viable NFT geometry, a nanoraindrop, were able to show the applicability of this model for nanofocusing applications. By shifting the hole towards the apex of the structure we observed an increase in intensity for the optically bright dipole mode, whilst also pinning the resonances to that point. Comparing this model to other tunable designs, we showcase that the energetic tuning is similar to other tuning methods [84]. The advantage here is the spatial pinning of the modes by displacing the hole and the enhancement of the mode. Therefore this prototypical design could have huge benefits too applications like HAMR. We will now, in the following chapter, explore the environmental effects on these NFTs and how their plasmonic properties are effected by a dielectric coating and high temperatures.

CHAPTER 4

ENVIRONMENTAL EFFECTS ON PLASMONIC NFTS

4.1 Abstract

Much of the work reported in previous chapters has considered NFTs in isolation: bare, patterned Au on a thin Si_3N_4 substrate that was used to explore the basic plasmonic response of NFTs, and had the advantage of giving rise to an appreciable EELS signal. In operation within HAMR, however, the dielectric and thermal environments of NFTs will differ substantially. It is projected that temperatures can reach 723 K for a very short period of time, of the order of 1 ns [20], and it is therefore essential that the NFT is thermally stable and unchanging in fluctuating harsh environment. Here, we have tested the thermal stability of our Au NFTs using bright field imaging and STEM EELS by applying heat

both inside and out of the microscope. Using out experimental method there was no way to fully replicate the intense, short-burst thermal fluctuations on NFTs in a HAMR device, therefore this work provides a general insight into temperature effects on the structural and plasmonics properties of NFTs. Prototype HAMR devices are known to have a limited lifetime due to the softening and retraction of the Au NFTs after the application of fluctuating temperature [101]. The melting point of bulk Au is 1337.15 K however the melting point and structural deformation temperatures for Au nanoparticles are considerably lower. Au nanoparticles have been observed to melt at temperatures between 600 and 1000 K [102] and picosecond laser pulsing of nanoparticles causes structural deformation at temperatures below the melting point [103]. For these reason, a variety of alternative materials have been studied. Nitride materials are known to be far more thermally stable than Au but have weaker plasmonic properties [20, 83]. Titanium nitride (a proposed plasmonic material for NFT applications [104]) has a melting point of 3203.15 K, however the thin film plasmonics presented in reference [105] show broad, low intensity peaks which do not compare well to those of Au or Ag. We will therefore continue to use Au as a plasmonic material due to its superior plasmonic properties but work has been carried out to increase the thermal stability of these NFTs, such as alloying [106] Au nanostructures. Here, we observe that the fabricated structures shown here are far more thermally stable than would be expected from the melting point of Au alone, which we attribute to a stabilisation effect of the Ti adhesion layer that is necessary for the NFT fabrication process. We also gain an understanding of how annealing effects the plasmonic properties of our NFTs.

We also explore the plasmonic properties of our NFTs coated with a dielectric layer.

The dielectric environment, whilst necessary in a working device, is an easy and effective method for tuning the plasmonic properties of a nanoelement, as described in section 1.2. HAMR NFTs, as shown in figure 1.2, will consist of a nanoelement partially embedded in a waveguide with one section exposed to atmosphere (in figure 1.2 this exposed section is tip of the nanolollipop NFT). The waveguide material in HAMR is an important consideration with numerous proposed candidate materials [20, 21, 83]. Here, however, we focus our efforts on Ta_2O_5 , a viable waveguide material due to its high reflectivity and low absorption [107]. To gain a better understanding for the plasmonic properties of NFTs in more realistic environments we perform STEM EELS on encapsulated nanoelements using a unique sample preparation method.

4.2 Thermal Stability of Au NFTs

Annealing can thermally activate processes such as solid state diffusion, which can allow for the removal of structural defects like grain boundaries [108]. We are interested in the macroscopic effect of grain boundaries on our plasmonic NFTs as their presence will have an effect on the energies of the modes [109]. Here we examine the structural and plasmonic properties of annealed NFTs from chapter 3, using TEM and STEM EELS. Temperature was applied both in the microscope (*is-situ*) and in a separate furnace (*ex-situ*) due to the two imaging methods being performed of different microscopes. This means that the NFTs were thermally annealed in vacuum and in atmosphere, but due to the inert nature of Au we did not expect to see any compositional change. Work carried out elsewhere [109] shows that annealing reduces the number of grains in Au ring and

rod nanostructures whilst altering the plasmonic properties. More detail of this work is given in section 4.2.2. The granularity of Au nanoelements is a result of the fabrication process shown in section 2.2. Throughout this thesis, we use a Ti adhesion layer for Au deposition. This is necessary due to the inability of Au to chemically react and hence bond to a substrate, resulting in effects such as delamination or dewetting [54]. Ti is a commonly used adhesive layer for noble metals as it forms chemical bonds with typical substrates and alloys with Au. This process is commonly simplified in the literature, but a detailed description of an underutilised adhesion model can be found in references [54, 110] where the authors present a comprehensive study of the effect of Ti and Cr adhesion layers on Au thin films. The Ti adhesion layer dictates the grain size of Au layer due to the enhanced wetting, as a result of $TiAu_4$ bond formation [111].

Solid-state dewetting is an important concept when considering the annealing of thin films. This effect is an agglomeration of a thin film material into globules, driven by minimising the free surface energy of the system by diffusion of material [112]. This process is thermodynamically driven, and has a number of forms such as fractal or void dewetting, which alter the surface topology quite drastically and have a profound effect on the plasmonic activity. A detailed overview of solid-state dewetting is given in reference [110]. It is understood that the decreased Au dewetting as result of using a Ti adhesion layer is due to the diffusion of TiO_2 through grain boundaries [113]. This phenomenon provides key insight into the thermal stability of our NFTs as they are annealed at high temperatures. Something else taken into consideration in this work is the relationship between annealing effects and particle size. In reference [114] the authors show that as the particle size decreases, the melting point also decreases. This is due to a phenomenon called melting

temperature depression [115]. As the size of a metallic nanoparticle decreases (for the order of 10s of nanometres), the surface-volume ratio increases which changes the thermodynamics. In this chapter, we examine a number of different sizes and geometries of Au nanoparticles up to and above the predicted operational temperatures in HAMR. We expect to see some size effects in the smaller NFTs examined here, but for the larger structures (similar to the dimensions proposed for HAMR NFTs) we expect them to be more robust.

4.2.1 In-situ Heating with TEM

We start this investigation by examining the effect of annealing the NFT geometries using TEM with in-situ heating. The FEI Tecnai T20 TEM was used in this section to image our annealed samples, a description of which is given in section 2.3. A dedicated heating rod was used to anneal samples in the microscope for 5 minutes, after which they were imaged at room temperature. This was necessary due to thermal drift, which caused severe imaging problems. Heating mechanism is similar to a filament in an (energy inefficient) electric light bulb, where a current is passed through a Tungsten coil. Our sample was positioned in the centre of the coil and the temperature is applied through thermal radiation and the temperature is controlled by dictating the current passing through the filament. This is a rather rudimentary process but was effective in annealing our samples. A number of NFTs with differing geometries and dimensions were examined in this section, fabrication of which is described in section 2.2. To observe the effect of annealing, we measured the mean grain size of each structure, along with the change in dimensions. Figure 4.1 shows TEM BF images for a nanolollipop structure, imaged after each given annealing tempera-

ture. In each image we have highlighted a number of grains in order to assess the change in grain size as a function of annealing temperature.

There are a number of factors dictating the thermodynamics of our system, which control the changes in shape, dimensions and granularity [54,113,114]. In reference [109], the mean grain diameter doubled after annealing at 637.15 K for 10 minutes, comparable to the experimental conditions shown here. In figure 4.1 there is a clear increase in grain size as the annealing temperature is increased. The figure shows that there is little change structurally to the NFT as the annealing temperature is increased. This corroborates the results observed in [113] in that the Ti adhesion layer increases the thermal stability of the Au deposition. Dewetting at temperatures much lower than presented here is seen in reference [116] (the lowest annealing temperature of 573.15 K results in clear dewetting). A quantitative analysis of grain size as a function of annealing temperature was carried out by using particle size analyser built into Gatan Digital Micrograph software [117], and is presented in table 4.1. In table 4.1, which shows the average grain size diameter for six devices, ranging from largest nanolollipop geometry of diameter 400 nm (figure 4.1), to the smallest dimensions of a nanotriangle, where the length of each edge is roughly 150 nm (figure 4.2).

We now examine the smallest nanotriangle structure as it is the most obviously effected by temperature. Figure 4.2 shows TEM BF images of a nanotriangle after each anneal. The figure shows that there is no change in dimensions or deformation in shape, however there is a clear change in structure due to the size effects as expected [115]. As the annealing temperature is increased we observe a clear decrease in the number grains in the element due to an increase in the average grain size as shown in table 4.1. From 293 K to 1073 K

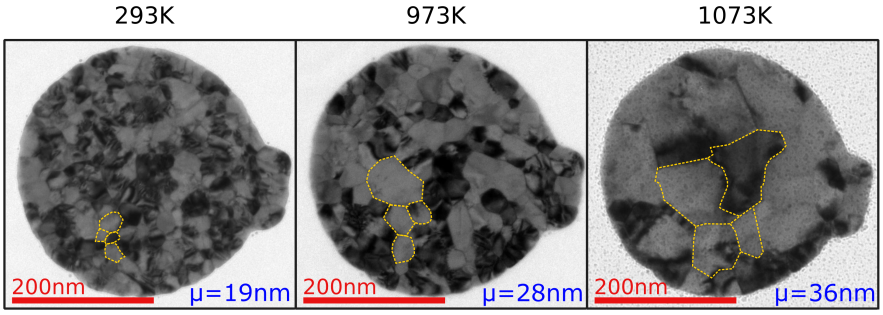

Figure 4.1: *TEM BF images for a nanolollipop imaged after a 5 minute anneal in vacuum at the temperatures indicated. A selection of grains are highlighted to illustrate the growth in size with annealing. The mean grain diameter, μ, is indicated in each image.*

there is an increase in the average grain diameter: a change of 20.5 nm; quite a significant change in size relative to the dimensions of the NFT. Figure 4.2 shows that annealing at 373 K (the lowest annealing temperature applied here) is enough to stimulate a change in grain size in this experiment - highlighting the sensitivity of Au to temperature. By 773 K, as proposed to be reached by NFTs in HAMR [21], we see an increase of 19.6 nm in average grain size which, again, is significant and could effect the coupling efficiency of the NFT with the incident laser-light in HAMR [101]. We will examine how this will effect the plasmonic properties below, but we would expect to see some change in the response of the NFT when annealed.

	293	373K	473K	573K	673K	773K	873K	973K	1073
Grain diameter (nm)	18.1	19.9	22.1	26.5	28.2	28.5	34.4	36.7	38.6
σ (nm)	47.1	51.9	53.7	58.3	67.4	73.8	74.8	77.9	7.9

Table 4.1: *Average grain diameter and standard deviation for six devices after annealing at temperature for 5 minutes.*

A number of mechanisms could be attributed to the change in grain size which, in reference [118], relate to the curvature and inter-facial energy of the grain boundaries.

Burke and Turnbull [119] calculated that the grain growth of a particular system depends on the radius of curvature for a grain and the boundary energy, however newer models have been proposed in order to incorporate topological factors, such as surface roughness and edge effects, into the understanding of grain growths [118]. This is beyond the scope of the work presented here but could be a part of future projects. Here, we observe a particular process known as *abnormal* grain growth. Normal grain growth is a continuous process where grains grow in a uniform manner. Abnormal grain growth is an inhomogeneous growth of selected grains which have growth advantages over their neighbours, meaning one or several grains grow at faster rates, consuming smaller grains and dominating the process. Abnormal grain growth process halts when two abnormally growing grains come into contact [118]. A study of normal and abnormal grain growth in Au thin films has been carried out by Ruffino *et al*. [120]. Both normal and abnormal grain growth can be explained by Ostwald ripening. This phenomenon describes the redeposition of smaller particles into larger particles, first discovered by Wilhelm Ostwald in 1897 [121], and theorised by Lifshitz and Slyozov 1959 [122]. In this process the transfer of matter from smaller to larger particles, minimising the free energy of the system [123]. Here we observe Ostwald ripening as larger grains absorb smaller grains due to annealing. Reference [124] gives an overview of Ostwald ripening, and examples of Ostwald ripening are shown in references [123, 125]. We understand that the growth process shown here is abnormal due to the increase in σ as a function of annealing as seen in table 4.1. As the grain size increase is inhomogeneously the distribution of grain size broadens, resulting in an increase in σ; a homogeneous growth rate would not change σ. The work presented here also shows that at temperatures of 973 K and 1023 K there is recrystallisation of smaller

nanoparticles around the perimeter of the sample. Solid-state structural transformations as a result of annealing are shown in reference [126], however the temperature at which these changes happen are much lower than observed here (373.15 K - 523.15 K). The reason for this discrepancy is due to the size of the particles examined in [126] (6-20 nm) and the Ti adhesion layer required for fabrication.

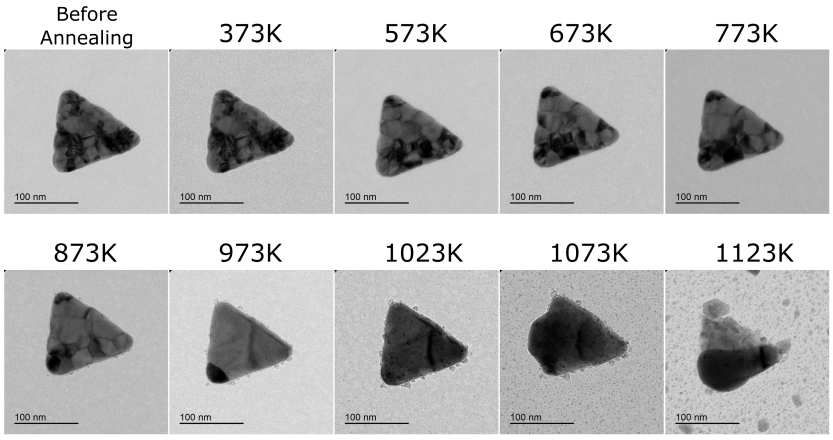

Figure 4.2: *TEM BF images taken after successive annealing at the temperatures indicated. The figures show a gradual increase in grain size as a function of annealing, until the temperature reaches a point at which we observe structural deformation. In comparison to figure 4.1 where there is no change in geometry, here it is clear.*

For an annealing temperature of 1073 K we begin to see a breakdown of the geometry, with the left-hand edge of the nanotriangle bulging out. This looks to be the beginning of a dewetting process in the nanotriangle as the surface energy is overcome by the thermal energy [112]. At the same annealing temperature we do not observe this behaviour in figure 4.1, corroborating the size-dependency annealing effects presented in reference [115]. This deformation would obviously have a huge effect on the plasmonics of the structure as this is a large change in geometry. We also observe some thermally induced changes on

the Si_3N_4 substrate at this temperature. At the highest annealing temperature, 1123 K, the structure is completely deformed from the original geometry and larger blotches appear on Si_3N_4. It is worth noting that, even for this small size of nanotriangle, the geometry and shape remained intact well above the operational temperature of HAMR, 723 K.

4.2.2 STEM EELS of Annealed Au NFTs

The importance of annealing effects in NFTs is important as it could effect the performance of the NFT [101]. Coupling efficiency is a measure of the power output from the plasmonic element in relation to the excitation laser light power [127]. Continuing from the work carried out above we examine the plasmonic properties of pre and post annealed NFTs in an attempt to understand how the nanostructure will behave in a HAMR device. The effect of annealing on Au nanorings and nanorods has previously been examined, where the quality factor increases as a function of annealing temperature [109]. The increase is due to a decrease in the size of the structure and a decrease in the Drude dampening within the elements as a result of increasing the average grain size [109]. This will be examined for our NFTs. We also expect that the Ti adhesion layer will quench the quality factor compared to that of an isolated NFT, based on similar results using a Cr adhesion and the similarities between the two adhesive layers [54, 55, 109]

The importance of grain boundaries on the plasmonic resonances as been studied previously, including a unique examination technique using Surface-Enhanced Raman Spectroscopy (SERS) and Atomic Force Microscopy (AFM), analysing 2D graphene layers that found plasmonic interference due to plasmon reflection at boundaries [108]. The plasmonics of a purely covalent system obviously differ from that of a metallic material,

but we would expect the grain boundary effect on the plasmonic resonances to have a similar effect. The macroscopic optical property changes as a function of grain boundaries presented in reference [128] corroborate our expectation. The authors show that Ag thin-films exhibit a decreasing trend in the refractive index as a function of increasing grain size. This is due to a decrease in grain boundary strains. Here we use *ex-situ* annealing, performing STEM EELS before and after, in order to understand effect of annealing and reducing the grain boundaries has the on the plasmonics of our NFTs. For HAMR applications, improving the quality factor (how sharp the resonances are in energy loss spectra) could result in a decrease in coupling efficiency between the input laser power and the output electric field [85].

Using our fabricated nanoraindrops described in section 2.2 (with major and minor axes of 300 and 250 nm respectively), with a Ti adhesion layer, we annealed our samples at 973 K for 10 minutes in three separate steps using a Carbolite CTF 12 tube furnace. We chose 973 K on the basis of the results of figure 4.1, as it is a temperature that showed clear change in granularity without effecting the structure of even the smallest NFTs and does not appear to effect the substrate. However, after the first bake there was no clear change in grain size, which would have resulted in no change in the plasmonics. Therefore we baked a further two times until there was an observable change in average grain size.

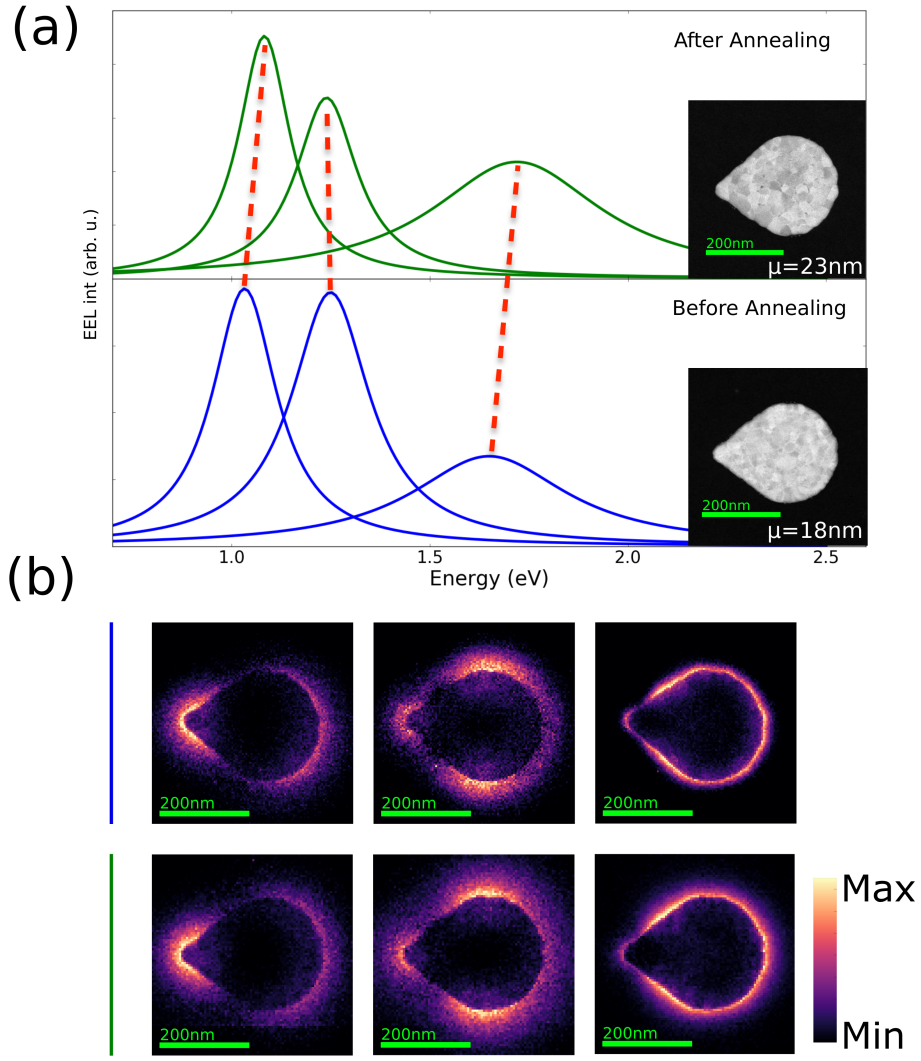

Figure 4.3: *STEM EELS of a nanoraindrop geometry before and after annealing at* 923 *K, dimensions for* 300×250 *nm and thickness* 25 *nm. (a) The individually resolved plasmon modes for a nanostructure before and after annealing. HAADF images are given inset and annotated with the average grain diameter,* μ*. (b) The corresponding energy loss maps for each peak in (a), aligned energetically from left to right.*

Shown in figure 4.3 are the resulting energy loss spectra and maps for a nanoraindrop

structure before and after annealing. Figure 4.3(a) shows the extracted plasmon models obtained through post-processing techniques described in section 2.4, with corresponding to an energy loss maps for each peak shown in 4.3(b). HAADF images of the structure before and after annealing are shown in figure 4.3(a). It is difficult to observe by eye but there is a change in mean grain size - given in each HAADF inset. The average grain diameter increases from 18 nm to 23 nm. The process of annealing, as mentioned above, causes abnormal grain growth through Ostwald ripening [109], but is limited by the relatively low T used. Here, the annealing of the sample has increased the dimensions by 1.23% and increased the grain size by 5 nm. Therefore we expect some change in the plasmonic nature of the structure after annealing due to the results shown in section 2.1, where figure 2.6 shows a clear change in resonance energy for different sizes of nanodisks. Figure 4.3(a) shows a change in the resonance energies of the modes observed for the nanoraindrop after annealing. Increases in each peak energy are seen as a result of annealing and are more prominent in the highest energy mode. These energy changes are indicated by the red dashed lines connected each mode.

A variable which will determine how annealing effects the plasmonics of the structures is the calculate the *quality factor*, Q. This was not considered as an evaluation tool in Chapter 3 as it would not have provided more insight in comparing directly the plasmon energies of the modes. Here, we use the Q factor to isolate the effect annealing has on the plasmonics of NFTs. This is a measure of the local field enhancement of the oscillation plasmon mode and indicates the coupling efficiency to an optical excitation [129]. It is also a measure of how sharp the resonance peaks are in the energy loss spectrum. Here,

we calculate Q as

$$Q = \frac{E_p}{FWHM}, \tag{4.1}$$

where E_p is the peak energy of the mode and FWHM is the full-width half-maximum [129]. In table 4.2 we show the calculated quality factors for each of the peaks in figure 4.3(a). Our understanding of annealing and how it effects the Q factor comes from the work carried out in references [109, 129, 130], where Q is calculated as a function of annealing and geometry. The Drude-Lorentz model defines the dielectric function as:

$$\varepsilon = \underbrace{1 - \frac{\omega_p^2}{\omega^2 + i\Gamma_p\omega}}_{\text{Drude Model}} + \underbrace{\sum_m \frac{f_m\omega_m^2}{\omega_m^2 - \omega^2 - i\Gamma_m\omega}}_{\text{Lorentz Oscillation}}, \tag{4.2}$$

where ω_p is the plasma frequency and Γ_p is the Drude dampening factor. Γ_m and ω_m are the dampening parameter and resonance frequency of the mth Lorentz oscillator respectively, f_m is the oscillator strength. The Drude model explains the *intraband* free-electron transitions whereas the Lorentz term comes from *interband* transitions for electrons in bands lower than the conduction band (d-band for noble metals) [129]. The Drude term describes the dielectric function of a free-electron gas of a metal in response to an excitation [22]. The Lorentz oscillation term corresponds to interband transitions with set energies [131]. For Au, we understand from reference [132] the first Lorentz oscillation is at 1.7 eV [132]. For our work this means that the quality factor for modes with energies above 1.7eV will be effected by the Lorentz oscillator term, and will reduce Q. This is observed in table 4.2 for both the pre and post annealed Q factors, where the breathing mode has a lower calculated Q factor than the dipole and quadrupole modes. We see a

	Quality Factor		
	Dipole	Quadrupole	Breathing
Pre	5.21	5.22	3.46
Post	6.85	6.60	3.29

Table 4.2: *Calculation of Q for each mode in 4.3 for a nanoraindrop pre- and post- annealing.*

33.5% increase in Q for the dipole mode, and an increase of 26.4% for the quadrupole. The next Lorentz oscillator energy is 2.3 eV which is greater than the highest observable mode in figure 4.3. In reference [129,131], the Drude dampening factor is defined in terms of three electron scattering terms: electron-phonon scattering, electron scattering from the film surface, and electron scattering from grain boundaries. In this, we assume that the first 2 scattering terms do not change after annealing, and therefore we attribute the reduction in the Drude dampening and increase in Q for the dipole and quadrupole modes to the reduction of grain boundaries. Therefore we expect to observe an increase in Q due to the reduction of the Drude dampening term. However for the breathing mode, above 1.7 eV, there is an additional dampening term due to the Lorentz oscillation term, and hence a reduction in Q for resonance energies. Here, we observe a decrease in Q, of 5.2%, for the breathing mode due to the increased interband transition contribution to the dampening [129]. These changes as a function of annealing may appear subtle in the spectra shown in figure 4.3, but our calculations show that there is significant changes in the quality factor. This could effect the coupling efficiency of the NFT in a HAMR application, which could effect the overall performance of the device.

4.3 NFTs Encapsulated in a Realistic Waveguide Material

The next aspect to explore in examining more realistic environments for our NFTs was to encapsulate them in a proposed waveguide material [87]. The design of HAMR devices proposed in a number of patents [88, 89, 133] show that the NFT is only partially exposed to atmosphere, with the bulk of the body being embedded in a waveguide. A schematic of this is shown in figure 1.2 in section 1.1.1. Dielectric environmental effects on plasmonics have been extensively studied for numerous tunable and enhancement applications. Controlling the surrounding dielectric material is a simple method for tuning the plasmonics of a system, reasons for which are described in section 1.2. TiO_2 and indium tin oxide dielectric layers have been shown to redshift plasmon resonance energies in thin Ag films [134]. This is attributed to the surface plasmon generation between at the metal-dielectric interface resonating at a lower energy than a metal-vacuum boundary. We have shown the effect of dielectric environment on the plasmonics of NFTs in section 2.1 by comparing an NFTs response with and without a substrate. This work corroborates the results presented in reference [55] where a decrease in energy and a broadening on plasmon peaks was observed. Core-shell plasmonics is a popular field of study, as the plasmon resonances of metallic nanoparticles can be tuned by varying thickness of dielectric shell. References [135, 136] present such results.

Here we look at Ta_2O_5 as a dielectric environment for our NFTs, which is a well studied optical material with high reflectivity, low absorption, and good thermal stability [107, 137, 138], making it a highly applicable material to HAMR. The choice of dielec-

tric layer was partly made due to the ongoing work of colleagues in Queen's University Belfast within the Centre of Doctoral Training that this work is aligned to, and Seagate Technologies. Currently, some colleagues are also investigating the dielectric coatings for thin metallic films as a method of enhancing the plasmonic properties whilst improving the thermal stability of the sample. In this section we examine the effect a waveguide material has on the plasmonic properties of our NFTs, using STEM EELS as before. To determine the plasmonic properties of our NFTs embedded in a waveguide material, we deposited Ta_2O_5 on top of pre-fabricated structures, a description of which is given in 2.2. After deposition of the Ta_2O_5 layer, the sample is too thick to be examined directly using STEM EELS [58]. Therefore, in order to examine the plasmonic properties of our NFTs in the dielectric environment, we milled cross-sections through the entire sample. This allowed us to pass the electron beam close to the encapsulated NFTs and examine the energy loss of plasmonics. This experimental set-up also emulates an NFT in an HAMR device [83]. The beam is rastered over a region similar to the position of a recording material in HAMR [139].

4.3.1 Deposition and Milling Process

Deposition of Ta_2O_5 was carried out in Queen's University Belfast's ANSIN facility using the Lesker UHV co-sputtering system. The deposition was carried out at 293K with 15 mTorr Ar gas, onto NFTs that had already been fabricated on Si_3N_4 membranes using the procedures described in section 2.2. The thickness of the deposited Ta_2O_5 layer was determined to be 57.1 nm byX-Ray Reflection (XRR) [140, 141], measurements were carried out using a Bruker D8 four-circle resolution X-ray diffractometer. We expect that

thickness would not be a factor in the plasmonics at this level [134]. Core-shell systems depend heavily on the dielectric layer thickness which are typically less than 10 nm [135], however our thickness exceeds this, and would have less of an effect in defining the overall plasmonics.

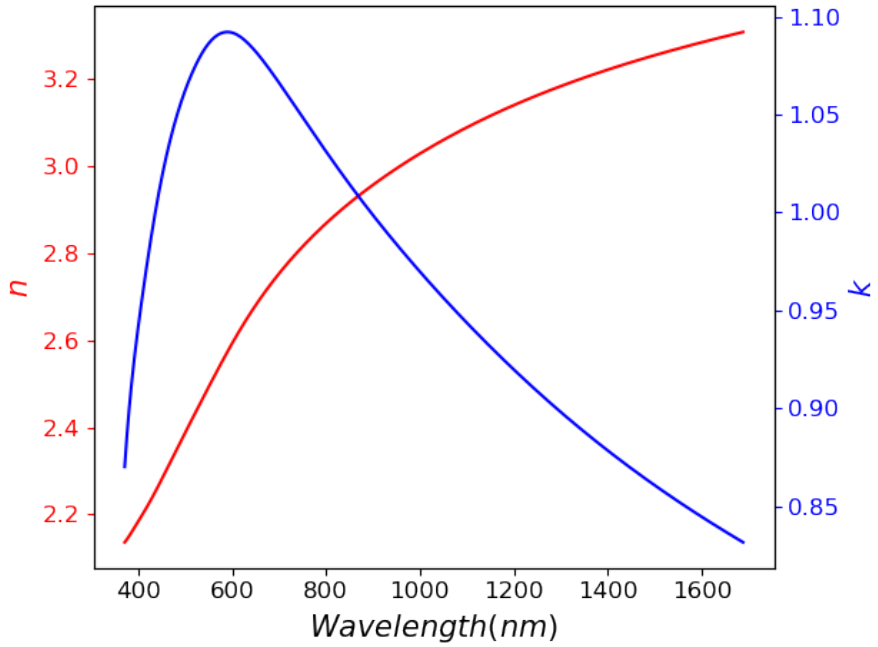

Figure 4.4: *The refractive index, n, and extinction coefficient, k, of Ta_2O_5 measured using ellipsometry.*

In order to measure the optical properties of the Ta_2O_5 layer we used a JA Woolham HS 190 ellipsometer, ranging from 380 nm to 1700 nm. This then allowed us to examine the refractive index, n, and extinction coefficient, k, as a function of wavelength, descriptions of which are given in section 1.2. Ellipsometry works by measuring the change in polarisation, from linear to elliptical, upon reflection from a sample by measuring the relative intensity and phase differences. Shown in figure 4.4 are the measured n and k values

for the deposited Ta_2O_5 layer. We can see in this figure that the refractive index continually increases as a function of wavelength. The extinction coefficient k peaks at 600 nm. Since k determines the optical absorption of electromagnetic waves in a material, the maximum amount of absorption is at the peak of k shown in figure 4.4. However, the energy ranges examined here will not be drastically effected by the absorption of the material (1eV-1.5eV equating to a wavelength range of 1240 nm - 826 nm). The n and k spectra exhibit properties similar to an amorphous material, with no sharp peaks observed which would indicate crystallinity [142]. Results show that the crystalline Ta_2O_5 layer shows much more prominent features in the dielectric function when compared to the amorphous layer [143]. This is due to a reduction in the dampening coefficient for the crystalline material. We would expect recrystallisation to occur when heating, something which is not explored here but would form part of future work. We can then use these values to calculate the real and imaginary parts of the dielectric function given in section 1.2 in order to simulated the plasmonic response with the measured Ta_2O_5 properties.

Focused Ion Beam (FIB) milling, described in section 2.5, was used to cut trenches through the sample in order to expose the encapsulated NFTs, a schematic of which is shown in figure 4.5(a). This was necessary for a number of reasons. The sample was too thick to obtain a good enough EELS signal-to-noise ratio to examine the plasmonics of the structures. We also wanted to partially expose the NFTs to create a more realistic environment. In HAMR devices, nanofocusing elements will be partially exposed to the inert atmosphere surrounding the HDD whilst being embedded in a waveguide [20, 88, 89, 133]. Our sample preparation process would emulate this in order to provide greater insight into realistic HAMR NFT properties. The FIB milling was carried out using a FEI

Nova 200 Duel-Beam SEM/FIB system. The result can be seen in figure 4.5(b) where three two trenches have been highlighted. The red and cyan stars in 4.5(b) indicate two nanolollipops that are examined using STEM EELS. Also seen here is another trench that was not successfully milled, highlighted by the pink star. We can see that the Si_3N_4 has not fully been stripped away, and the milling process has completely destroyed a column of NFTs.

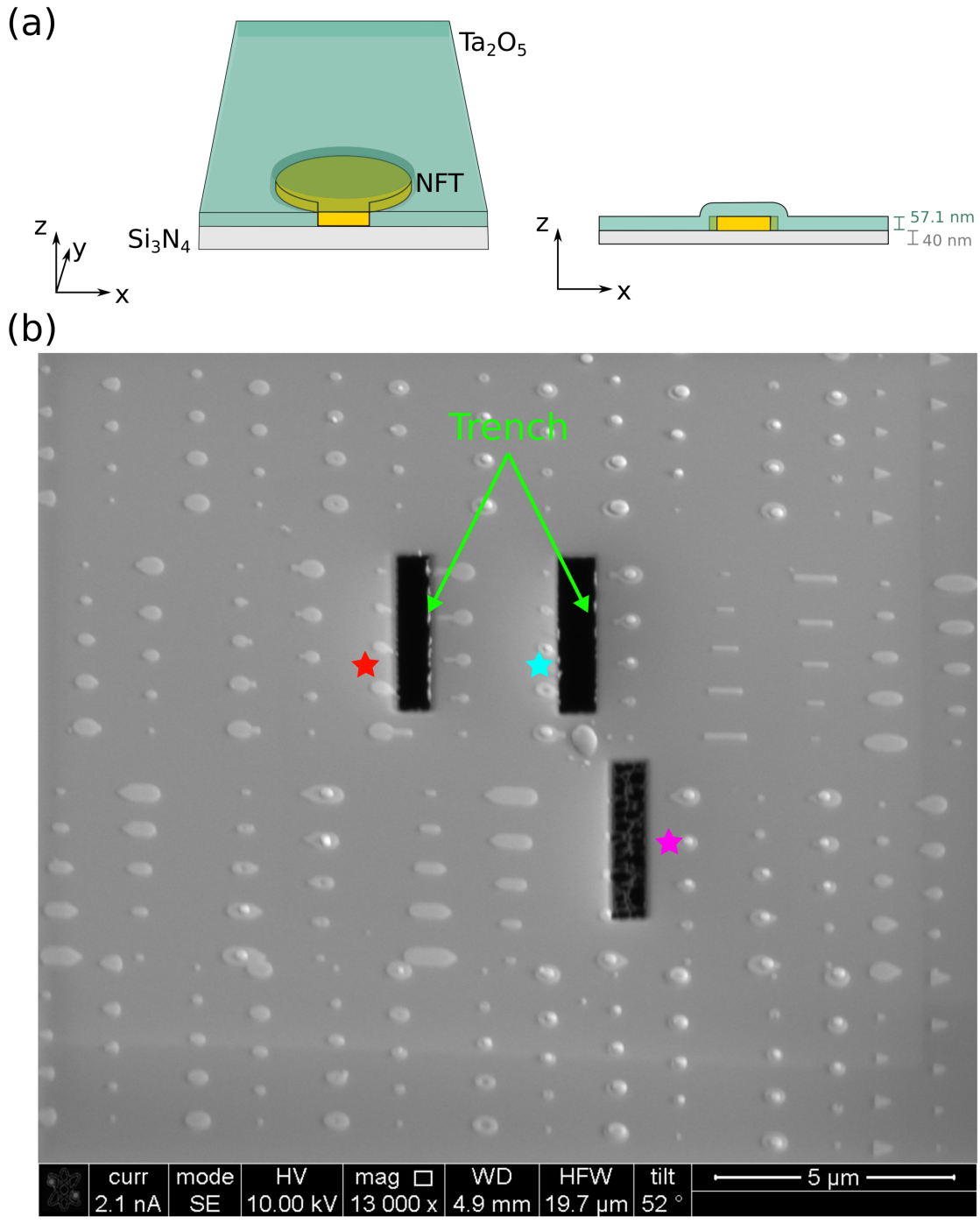

Figure 4.5: *(a) A schematic of encapsulated NFTs between $Si_3N_4$and Ta_2O_5 layers. (b) SEM image of encapsulated NFTs with trenches created using FIB milling. Red and cyan highlighted structures are the two examined using STEM EELS as they are exposed to vacuum.*

Another feature of the sample preparation process that can be observed in this figure is the *warping* of the membrane as a result of FIB milling. For both of the highlighted trenches there is a clear downward curvature of the sample towards the trench edge. One method to resolve this issue is to fabricate structures onto pre-made, sharp edges which we will examine later. Another aspect of this experiment is the inability to finely select an area to mill that would allow one to accurately expose an NFT to atmosphere.

4.3.2 Aloof-beam Excitation of Encapsulated NFTs

In order to examine the plasmonic properties of our encapsulated NFTs we performed STEM EELS using aloof-beam mode, placing the electron probe adjacent to the NFTs highlighted in figure 4.5 (through the milled trench). Shown in figure 4.6 is the HAADF image for a solid an annular nanolollipop (highlighted in figure 4.5 by a red and cyan star respectively) of dimension 400 nm and 300 nm for major and minor axes respectively, with the region of interest in each figure given, where STEM EELS was performed. Electron energy loss maps of each region are shown in figure 4.6 with resonance energies given.

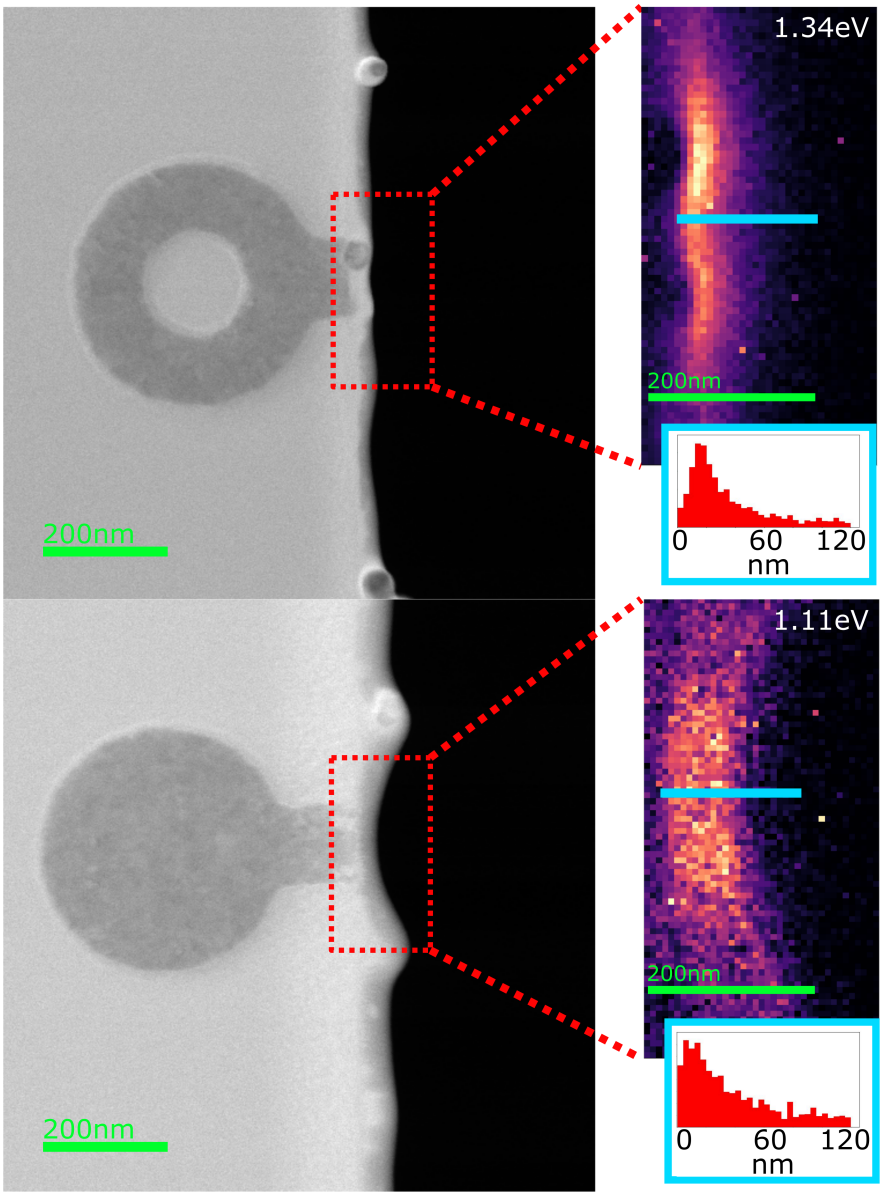

Figure 4.6: *HAADF images for a solid (bottom) and annular (top) nanolollipop encapsulated in Ta_2O_5 . The FIB milled trenches have cut through antenna so that the expected location of the hotspot is accessible to the electron beam. The red dotted rectangle indicated regions over which STEM EELS is performed and each energy loss map is shown, with resonance energies given. Intensity line traces for each energy loss map are shown in blue, highlighting the decaying exponential field.*

To begin with, we compare the resonance energy with that of an isolated NFT. Figure 3.4 in chapter 3 shows the resonance energy for a number of NFT geometries. The dipole (lowest energy mode) of the middle stem length in this figure can be compared to the solid structure (bottom) NFT. There is a redshift in energy of 0.07 eV when the NFT is encapsulated in a dielectric material, which is expected. This will be explored further when we incorporate the simulation model in the analysis. The red dotted rectangles in figure 4.6 HAADF images indicate the regions over which STEM EELS was performed, and energy loss maps are given for each region (max energy of energy loss spectrum is given for map). For both energy loss maps we have taken a line trace, shown in blue, and plotted the energy loss intensity across this region given inset. Both intensity line traces show an exponentially decaying trend which is expected due to the nature of surface plasmon resonances described in section 1.2. It is worth noting that a peak is seen in each intensity plot due to the line trace taken just before the intense section of the maps. From both energy loss maps it is clear to see that we are able to resolve a plasmon resonance of the NFT using the aloof electron beam. In both results the intensity of the energy loss decays into the trench (a space of vacuum) and follows the exponential characteristics seen in reference [22] and described in section 1.2. In section 3 we compared the plasmonics of annular and solid structures, with energy decreasing when a hole is present in the centre of the disk. Here, however, we do not observe the same result. From solid to annular nanolollipop we see an increase in the energy of the mode, which does not corroborate results seen in figures 3.5, 3.10. Examining some features the HAADF images of figure 4.6 we can see a number of issues that show that this experimental procedure is non-ideal. In the HAADF images for the annular structure (top image) we can see a circular region of contrast at the

edge of the sample (between the stem of the lollipop and the edge of the sample). Since the particle is plasmonically active at this energy range we identify it as Au and deduce that this plasmonically active nanoparticle will effect the energy of the plasmon mode excited in the NFT. From solid to annular structures we would expect to see an energy shift of the order of roughly 0.1eV based on the work in chapter 3, but this is not the case in figure 4.6. The unwanted nanoparticle could explain some of the discrepancies between the results presented here, and the results of chapter 3. In reference [82] a comprehensive study was carried out comparing EBL and FIB sample preparation for plasmonic antennas. We have also discussed this in section 2.2, however in context of the work carried out here, the authors discuss the effect of Ga^+ ion contamination on the plasmonics of fabricated NFTs. The results shown in reference [82] indicate that the contamination from the milling process weakens the plasmonic response of FIB milled samples in comparison to EBL fabrication, but does not completely quench the plasmon resonances. Therefore we can assume the same effect is applied in this work for the FIB milled samples.

We created a complementary simulation model to compare to the experimental results, based on the schematic shown in figure 4.5(a), using the dielectric properties for Ta_2O_5 obtained through ellipsometry measurements. However a number of compromises had to be made due to the complexity of the encapsulated system. Warping of the sample near the trench edge, observed in figure 4.5, was not simulated due to the difficulty of implementing such a feature in the mode but is not expected this to have much of an effect on the plasmonics as the curvature of the sample insight. Another, more significant, aspect that could not be simulated is the cross-section of the NFT exposed to the atmosphere. Two simplifications had to be made in order to have a working model. The first

simplification was to exclude the Si_3N_4 layer from 4.5(a) due to the computational cost; the model consistently ran into memory issues when computing. The second simplification was to have a 1 nm gap between the edge of the Ta_2O_5 layer and the nodule of the NFT. This was required due to the model building method used here, where a design is created in 2D and extruded to 3D. Other model building methods were not explored due to time constraints, but could be part of some future work. We have previously shown and discussed the energy shifts of Au nanostructures with the presence of a substrate due to the coupling between the two boundary plasmons. The sample shown in figure 4.5(a) has three boundaries for plasmon generation, and we expect further energy shifts as a result of coupling between all three. Therefore the simplifications in the simulated model will not be a complete comparison but still provides insight into the experimental results. We also wanted to compare the results in figure 4.6 which show the simulated and experimental data obtained for nanolollipops of the same dimensions without the encapsulated layer. Here we examine the simulated and experimental data for a solid nanolollipop with and without and encapsulating Ta_2O_5 layer. We have labelled the structures without an encapsulated layer as 'isolated'. Figure 4.7 shows the experimental and simulated energy loss maps for encapsulated and isolated (no Ta_2O_5 layer) NFTs. The isolated simulation model was calculated without a Si_3N_4 substrate, reasons for which are given in section 2.1.

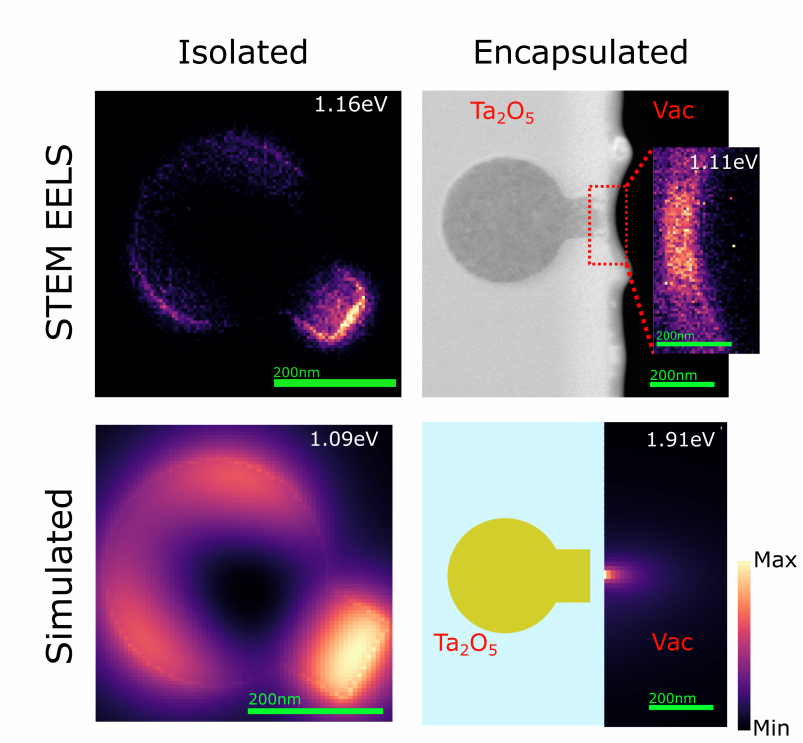

Figure 4.7: *Simulated (bottom row) and experimental (top) energy loss maps for nanolollipop geometry in isolation (left column) and encapsulated in* Ta_2O_5 *. Resonance energies for each of the maps are given.*

In figure 4.7 we show a comparison between simulated and experimental energy loss maps for encapsulated and isolated NFTs, with each resonance energy for the maps given for each figure. From each of these maps we immediately observe that a hotspot appears in the region we expected it to: the stem of the lollipop. By examining the isolated structures it is clear to see that the intensity distribution in each figure match very well. There is a difference of 0.07 eV in the peak position when comparing the simulated and STEM EELS results. From the work carried out in section 2.1 and in references [44, 45] we fully expect there to be a redshift of the mode with the inclusion of a Si_3N_4 substrate. This would

account for the differences of 0.07 eV. When examining the STEM EELS datasets for the isolated and encapsulated systems we see similarities in the energy loss maps with the region of highest intensity being observed at the stem of the structure. There is a decrease in energy by 0.05 eV when an encapsulating layer is present which is expected from the results shown in reference [49].

The outlier in figure 4.7 is the simulated results which include an encapsulating dielectric layer. When compared to the simulated-isolated lollipop we see a large difference in resonance energy, 0.82 eV. This is in contrast with the experimental results where a decrease in resonance energy is observed (and expect). Differences can be attributed to the two simplifications stated above. From the work carried out in section 2.1 we fully expect there to be a redshift of the mode with the inclusion of a Si_3N_4 substrate. The model presented here has plasmons generated at two boundaries: metal-vacuum (bottom of the NFT) and metal-Ta_2O_5 . The schematic shown in figure 4.5(a) has plasmons generated between metal-vacuum (nodule of the NFT exposed by the cross-sectioning), metal-Ta_2O_5 and metal-Si_3N_4. This would play a huge role in defining the plasmonic energy of the system and would account for opposing trend of resonance energy when compared to the STEM EELS results. Again, examining the resonance energies of the simulated and STEM EELS encapsulated results we see a trend opposed to that of the isolated systems - an increase of 0.80 eV from STEM EELS to simulated compared to the decrease of 0.07 eV seen in the isolated results. In the simulated-encapsulated energy loss map we also observe that the resonance is highly localised to a 'hotspot' which is not seen in either the simulated-isolated structure or the STEM EELS-encapsulated results. We believe this to be a non-physical error in the model and indicates the need to redefine the simulated-

encapsulated model in order to address this issue, as well as other the aforementioned differences. Therefore the limitations in the current state of the model mean we cannot make a full and comprehensive comparison between the simulated and experimental data. However, what has been shown here is a preliminary exploration into the plasmonics of NFTs in more realistic HAMR systems using STEM EELS, which has yet to be seen in the literature.

4.4 Conclusion

We have illustrated the impact of environmental factors on plasmonic properties of our fabricated NFTs. We know that the operational temperature of HAMR is 723 K [21] which is above the softening point of Au. We therefore have annealed our samples at this temperature and above it, in order to understand the effect on structure and the plasmonics. Annealing allows for abnormal grain growth [118, 120] in our NFTs which in turn effects the plasmonics by *increasing* the quality factor for plasmon modes below the threshold energy of 1.7 eV [129], shown in figure 4.3. The quality factor for only the observable mode above this threshold energy *decreases*. This is not a desirable attribute for HAMR applications as it could potentially decrease the coupling efficiency of the mode to the optical excitation. The structural integrity of the examined NFTs vastly exceeded expectations as the majority of the geometries did not deform well above the operational temperature. This is attributed to the Ti adhesion layer which increases the structural stability of the elements without quenching the plasmonic properties, and could potentially be very useful for applications like HAMR. We have also encapsulated our NFTs in a viable waveguide ma-

terial, Ta_2O_5 , in order to understand the plasmonic properties of NFTs in an environment more akin to HAMR devices. Using FIB milling and aloof-beam STEM EELS we were able to resolve one plasmonic mode for NFTs in a realistic HAMR environment. We show that we are able experimentally observe the exponential decaying nature of the decaying electric field, as described in secion 1.2, in the corresponding energy loss maps of these resolved modes. When compared to isolated structure (NFTs on Si_3N_4 membranes with no encapsulating layer) we see a redshift in energy, which is expected. The accompanying simulation model for both the isolated and encapsulated systems show some limitations in the model, which results in energetic discrepancies between the two.

CHAPTER 5

PLASMONIC PROPERTIES OF SIMULATED DIMPLE STRUCTURES

5.1 Abstract

In this chapter we move away from the HAMR application motivation and turn our attention onto devices used in biodetection. A theme running through much of plasmonics research is symmetry and the structures studied in previous chapters have had one or more mirror planes that produce mirror symmetries in both the charge distribution and in the plasmonic metamaterial's response to electromagnetic radiation. However, recent research has recognised the potential for chiral structures to support chiral plasmon resonances that are proposed to couple asymmetrically to the chiral structures of many biomaterials and have formed the basis of sensors [144]. Here we will examine the individual and combined

components of dimple shuriken structures shown in figure 5.1. Shuriken structures have sixfold rotational symmetric geometry but lack mirror planes, with 6 curved arms joined at the origin. The dimple structures examined here are depressions of geometries into a larger plane of material, and we will examine fully connected and disconnected systems, i.e. where the depression and larger plane are connected and disconnected. Shuriken geometries have been shown to successfully detect protein molecules, the results of which can be found in references [14,145,146]. Work carried out in reference [3] examines chiral shuriken dimple structures using optical excitations for the purposes of protein detection. These chiral dimples form the basis of the models discussed here, which we examined using simulated electron energy loss spectroscopy. This technique allowed us to examine further the plasmonics of the structure, observing optically bright and dark modes. We begin by calculating the plasmonic response of a simple rod geometry and breaking down the dimple structure into individual components (solid and aperture) and then the combined connected and disconnected dimple structures. In doing so, we examine the hybridisation between the solid and aperture in both the connected and disconnected dimple structures. We then apply the same systematic breakdown of the dimple structure for the shuriken geometry.

5.2 Solid, Aperture & Dimple Structures

Plasmonic properties of shuriken chiral geometries have been studied using optical excitations in references [14, 146]. These are highly complex plasmonic structures that have been utilised successfully in biosensing, where such nanostructures have been employed

to detect protein molecules [14, 145]. Protein detection capabilities stem from the chiral nature of the molecule and the asymmetrically enhanced (superchiral) electric field of the nanostructure - generated from optical excitation of the surface plasmon resonances. These superchiral sensors are shown to be highly sensitive to protein molecules, highlighted in references [14,145,146]. Figure 5.1 shows a schematic of a chiral-shuriken metamateirals, where an indentation/dimple design can be seen. To facilitate the mass-fabrication of these nanostructures, Kairmullah et al [3] used nanoimprint lithography whereby a 'master' nanostructured stamp is pressed into a soft substrate to produce nanostructure depression, akin to the methods used to produce compact discs [147]. This process creates arrays of indentations (or dimples as they will be referred to throughout this chapter) over which Au is deposited.

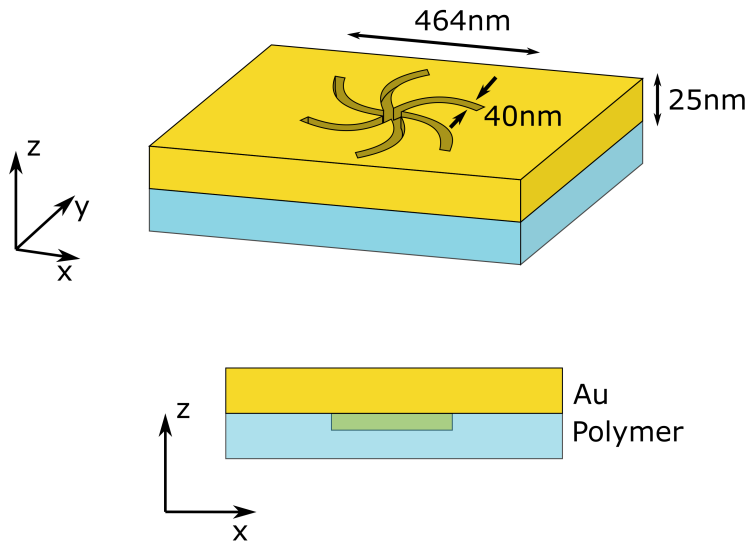

Figure 5.1: *Schematic of a dimple chiral structure adopted from [3]. A shuriken geometry indentation is made in a polycarbate substrate, over which Au is deposited, creating dimple structures. The dimensions in the x and y plane match that of the cited paper, however the thickness was reduced here. This is due to our STEM experimental methods and the requirement for thin samples (see section 2.3 for details).*

The mechanism used for molecule detection is based on self-coupling in the nanostructure. Self-coupling in the dimple device shown in figure 5.1 and in reference [3] relates to the upper and lower sections. Here we define the upper part as the large body with an aperture and the lower part as the depressed solid structure. It has been shown that molecular detection is possible as the optically dark modes (excited by the molecule) of the lower solid part of the device couple to the optically bright modes of the upper section. A justification for this coupling mechanism can be made from Babinet's principle. a description of which is given below. Here we employ a computational EELS study in order

to examine optically dark modes which are being excited in the dimple model and being coupled to by chiral bioparticles [145]. We employ a breakdown of the dimple model to observe the individual modes in an attempt to better understand the hybridisation capabilities of a combined model. We also expect to see some out-of-plane coupling between the vertically separated structures due to the work carried out in references [34, 48]. It is worth reiterating the requirements for hybridisation, set out by Prodan in reference [1] and described in section 1.2.2. For such an interaction to occur, two features must be present in the combined system: symmetry in the charge distribution and energy matching for the modes of the separate structures. In this chapter we examine whether or not we observe hybridisation in the system, or whether we are showing coupling between the two systems (i.e. one part of the model is responding to a mode generated in the corresponding structure).

In order to understand the nature of coupling in the dimple model depicted in figure 5.1, we first simplify the system by breaking down the model into individual components and simplifying the geometry. Figure 5.1 can be thought of as a fully connected system consisting of a solid shuriken structure and an aperture of the same geometry, separated in the z-axis. Here we have broken down this model into individual solid and aperture parts, and examined the plasmonic properties of both in order to understand the coupling capabilities. We recombined the individual components to form a disconnected and connected dimple structure. We also begin by simplifying the geometry of the chiral-shuriken structure by using a rod, in order to build a foundation of the plasmonics of the individual and combined systems. This has the advantage of producing considerably simpler spectra in which modes can be identified, and was also anticipated to help understand how the individual

arms of the shuriken might behave. We started by simulating a simple nanorod geometry, length 232 nm and width 40 nm (the same length and width as one arm of the shuriken shown in figure 5.1), in all 4 configurations. However some consideration was taken when building the aperture and dimple models, as we wanted to isolate the plasmonic properties of the inner geometry for the aperture and dimple structures. As mentioned above, we are examining the dimple structures of a geometry pressed into a large plane of material. Therefore testing of maximum size of the plane was carried out. However, due to the simulation package, we are limited by the amount of memory available to the software and hence the size of model and the nodal density of the mesh are hampered. Descriptions of the limitations are given in section 2.1 and reference [39]. The maximum size of plane was tested and found to be 700 nm diameter for a disk of thickness of 25 nm.

Babinet's Principle

Before we examine the simulated structures, we define an important concept in plasmonics when comparing solid and aperture (positive and negative) structures which will form the basis of our argument when discussing self-coupling in our model: Babinet's principle. Babinet's principle is an old concept formed by Jacques Babinet in the 19th century [148]. It states that the diffraction of light from an aperture would be the same as that of a solid structure of the same geometry [148, 149]. This is a consequence of the electric and magnetic fields interchanging in the positive and negative complimentary systems. Details of a theoretical derivation of Babinet's Principle can be found in references [149–151]. For plasmonics, this would imply that the resonances for a solid/aperture complementary system should be similar. Figure 5.2 shows a schematic of a solid/aperture disk structure

where the charge distributions match spatially. When both the solid and aperture components in figure 5.2 are physically overlapped, the charge distributions would match in a similar manner to that seen in the aforementioned hybridisation model (in the case of figure 5.2 this would be attributed to a bonding mode), and would therefore be a coupled system.

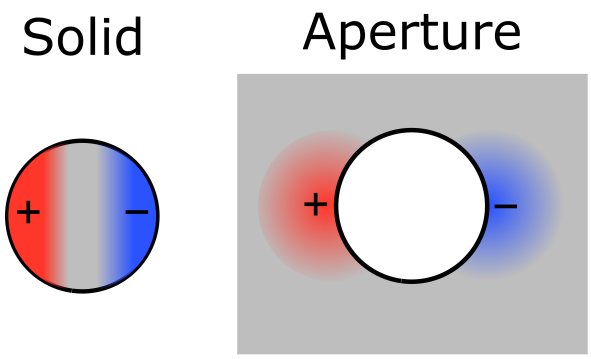

Figure 5.2: *Schematic of charge distributions for a solid and aperture nanodisk structure. Similarities in the distributions indicate the hybridisation possibilities of a combined system - this is one of the requirements set out by the model given in section 1.2.2.*

A number of studies have been carried out to examine the validity of Babinet's principle in the field of plasmonics. Simple nanodisk solid and apertures are studied in references [152, 153] in which the authors present a comprehensive comparison between the complementary systems. Work undertaken in reference [152] investigates the limitations of Babinet's principle for lithographically patterned, non-symmetric nanodisks. In this, the authors show that the resonance energies generated for both solid and aperture systems are in good agreement, and that Babinet's principle is still applicable in real samples with asymmetries created due to the non-idealistic fabrication process. The work shown

in reference [153] continues to study hole-disk structures in a now combined system, and also introduces an asymmetric factor; asymmetry in this work stems from misaligning the hole-disk pairing. Out-of-plane coupling for symmetrically positioned samples is observed for the upper and lower structures. As asymmetry is introduced a new distinct peak is observed in the transmission spectra. The authors hypothesise that the new mode in the optical transmission spectra is a result of the hybridisation between the quadrupole modes of the hole and disk. Work relevant to the results presented here was carried out by Hentschel *et. al.* in which coupling between rods and slits was studied [151]. The authors show that Babinet's principle for solid and aperture rod structures would not allow for a coupled system when combined - this expectation is also held here and is discussed below. Some of the work carried out in reference [151] was to examine the coupling between two rod apertures, in parallel, with a solid nanorod placed vertically above. The rod was displaced from the symmetric, central position along the parallel axis of the apertures, in order to facilitate out-of-plane coupling between the two components. Babinet's principle has been studied for more complex structures, such as the Sierpiński fractals [154]. Here, the authors build an argument of coupling, based on Babinet's principle, between nanotriangle holes and solids which determined the plasmon resonances generated in fabricated, first-order Sierpiński fractals. This work was then expanded to more complex plasmonic Sierpiński fractal systems [155]. Therefore, based on the work in the literature, we have simplified and de-constructed the dimple structure shown in figure 5.1 to examine coupling in such a system. We have then built a more complex (shuriken) model with insights generated from the simple rod system.

Simulated Results

Simulated energy loss spectra for a solid, aperture, connected and disconnect systems for a rod geometry are shown in figure 5.3(a), with cross-sectional schematics of each simulation model shown to the right of the appropriate spectrum. Each spectrum is a summed spectrum from a number of impact points across the entire geometry, as described in section 2.1 and consistent with the rest of the thesis. Corresponding energy loss maps and eigenmodes for each peak are shown in figure 5.3(b), in a similar manner presented throughout this thesis (see section 2.1 for details of calculations). Each plasmon mode in figure 5.3 is labelled $R_{X,Y}$ where X indicates the simulation model (solid (S), aperture (A), connected (C) and disconnected (D) dimple) and Y is a number ordering the modes energetically - R indicates the results for the rod geometry (to minimise confusion with the shuriken geometry modes given below). The spectrum from the solid rod structure, given in blue in figure 5.3(a), has 3 distinct peaks with energies at 1.54 eV, 2.15 eV and 2.34 eV, labelled $R_{S,1}$, $R_{S,2}$ and $R_{S,3}$ respectively. These three modes have clear resonances shown in the corresponding energy loss maps in figure 5.3(b). From the eigenmodes we understand that these modes are the 1st, 2nd and 3rd order rod modes consistent with the literature [92]. The resonances for the solid structure are generated across the length of the rod. This is a feature we will return to when we explore the coupling possibilities in the combined systems. Some pinning in the corners of modes $R_{S,2}$ and $R_{S,3}$ can be seen, which would possibly be alleviated by further rounding of the geometries edges.

In the aperture plasmon spectrum in figure 5.3(a) (orange spectrum) we identify 6 distinct modes. Figure 5.3(b) shows the energy loss maps and eigenmodes for the three the peaks. Energy loss maps and eigenmodes for $R_{A,1}$, $R_{A,1}$ and $R_{A,3}$ are not shown here

as they are plasmon resonances generated for the larger outer disk and offer no insight to the properties of the aperture. Modes $R_{A,4}$, $R_{A,5}$ and $R_{A,6}$, resonate at 1.88eV, 2.11eV and 2.34eV respectively, where there is a large amount of overlapping in the resonance peaks (a broad feature in the spectrum). From the eigenmodes we observe quite different distributions to that seen in the solid structure, where $R_{A,1}$, $R_{A,2}$ and $R_{A,3}$ are the 1st, 2nd and 3rd order rod aperture modes. Unlike the solid rod resonances, the plasmon modes are generated across the width of the aperture (validated by the work presented in [150]). For instance, comparing the eigenmode of $R_{A,1}$ to $R_{S,1}$ we can see that the charges to no overlap if they were combines (as they will be in the dimple structures). These results are consistent with Babinet's principle and with the work presented in reference [151], but do not meet the criteria set by the hybridisation model [1]. Therefore we expect a combined system would not form a coupled system based on the hybridisation model. This can also be assumed for the higher order modes of both structures.

We now examine the dimple structures in order to build a better understand the realistic model shown in figure 5.1. The connected structure, yellow spectrum in figure 5.3(a), looks similar to the aperture spectrum with 4 distinct peaks in this spectrum, as labelled. As this model is fully connected, we expect the results to act similarly to a disk (discussed below), however we expected to observe some out of plane coupling due to the closeness of the surfaces of the upper and lower boundaries. It was also imperative to examine this model as it replicates the devices shown in references [3, 14, 145, 146]. Modes $R_{C,1}$ and $R_{C,2}$, with resonance energies of 2.15 eV and 2.35 eV respectively, are purely edge modes for the outer disk similar to $R_{A,1}$, $R_{A,2}$ and $R_{A,3}$, and are not shown in figure 5.3(b). The energy loss map for mode $R_{C,3}$, of 2.10 eV, has an intensity distribution similar to that of

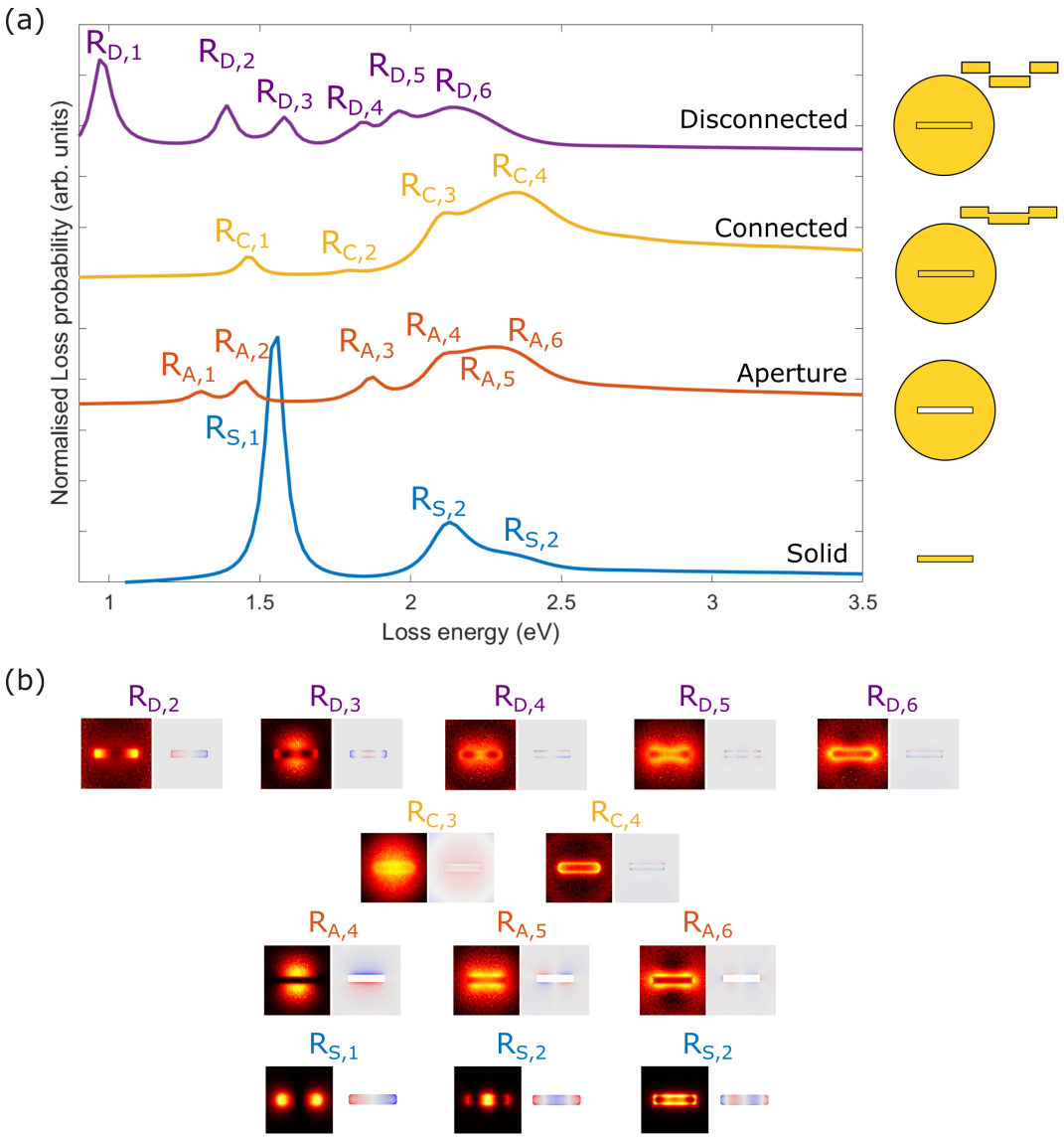

Figure 5.3: *(a) Simulated EEL spectra for a solid, aperture, disconnected and connected dimple structure using a rod geometry. Each spectrum is labelled with a schematic shown to the right hand side of the relevant spectrum, and each observable peak is numbered. (b) Corresponding energy loss maps and charge distributions for each peak in (a).*

a breathing mode, emanating from the centre outwards and is comparable to mode $R_{A,5}$. Mode $R_{C,4}$, of 2.41 eV, has an energy loss map with intensity around the perimeter of the dimple-rod structure. Its eigenmode reveals some inner charge distribution across the depression geometry, but does not show any hybridisation between the upper aperture and lower solid structure. We can infer that the connected dimple geometry behaves in a similar manner to a large disk, where the charges are free to move around it and no out-of-plane coupling is present for the surfaces of the dimple. The discrepancies between the work presented in the literature and the results shown here leads us to conclude that the dimple depths studied here are not severe enough to observe coupling between the surfaces, and that the disconnected structures is a more comparable model. We will explore depression depths and gap distances for the dimple models below.

Lastly we examine the fully disconnected dimple system, with a 2 nm gap between the upper aperture and the lower solid structure shown in the cross-sectional schematic in figure 5.3(a) (disconnected dimple spectrum is purple in this figure). Gap distance is discussed below. As mentioned previously, we expect to see out-of-plane coupling due to the out-of-plane interactions between upper and lower surfaces. We also expect to see more plasmonic activity in this system as they are separate entities. In comparison to the connected dimple system there is a larger number of distinct modes, with 6 resolvable peaks shown in the purple spectrum in figure 5.3(a) and corresponding energy loss maps are shown in 5.3(b). It is clear to see that each mode has some dependency on the aperture and solid geometry, unlike the connected system. This results in a larger number of plasmon modes observed for this system when we consider that the disconnected structure hosts both solid and aperture modes , and causes some shifts in energy for some of the

plasmon mode energies. To understand the coupling in this system, we first examine the plasmonics of the solid and aperture in order to see if our system fits the hybridisation model. From the appropriate spectra in figure 5.3(a) (blue and orange for solid and aperture respectively) we can see that there are some overlaps in energy between modes $R_{S,2}$ and $R_{S,3}$ for the solid structure, and modes $R_{A,4}$, $R_{A,5}$ and $R_{A,6}$ for the aperture. However we do not see any symmetry matching from these modes as can be seen in the charge distributions or the eigenmodes of each of these peaks. The modes shown in the disconnected system are a result of coupling between the solid and aperture: when modes are excited for the individual elements in the system (solid or aperture) we observe a response in the other element [156]. However, in the disconnected system we do observe a large amount of plasmonic activity which is explored below.

To examine the interaction between the upper (aperture) and lower (solid) parts of the disconnected model we show the energy loss maps and eigenmodes, and we also examine the charge distributions arising from a specific location for the incident electron beam. These are charge distributions generated by the incident beam and are dominated by the location of the excitation. We have chosen to look at these results as they offer insight into the localised coupling between the two structures that could be missed in the eigenmodes. Figure 5.4 shows the energy loss maps and eigenmodes (from figure 5.6) as well as the localised charge distributions. Modes $R_{D,2}$ - $R_{D,6}$ seen in figure 5.3 are shown here as the intensity of mode $R_{D,1}$ is not shown it is a purely outer-edge mode similar to $R_{A,2}$ and $R_{A,3}$ and is of no further use here. Charge distributions are created from an impact point which is indicated in each figure as a blue arrow. Both the energy loss maps and the charge distributions are then matched energetically to the calculated eigenmodes [41]. $R_{D,2}$, as

Figure 5.4: *Top - energy loss maps, middle - charge distributions calculated using the incident electron beam and bottom - eigenmodes of the peaks found for a disconnected dimple structure with a rod geometry shown in figure 5.3(a). Charge distributions are calculated using the impact position shown by the blue line in each corresponding map. These are localised charge distributions dominated by the impact location, but offer insight into the coupling between the upper and lower surfaces.*

one would expect from the charge distribution, is a dipole mode generated in the solid rod structure. The resonance is across the length of the solid rod structure and has very little interaction with the aperture, as seen in the charge distribution and eigenmode; this is an individual rod mode. Mode $R_{D,3}$ is a quadrupole mode generated in the solid structure which induces a coupled mode in the aperture. This is an interaction from one structure in response to the plasmon mode of the other and is shown by the charge distribution at the impact point of the electron beam. Mode $R_{D,4}$ and $R_{D,5}$ are quite similar in their energy loss maps, but the charge distributions show that these are another quadrupole configuration and a hexapole mode respectively. Similar to mode $R_{D,4}$, these resonances excite a coupling mode to the aperture. Mode $R_{D,6}$ is a dipole mode across the width of the rod, rather than the length as we saw in mode $R_{D,2}$. These results confirm the initial estimation that there is no hybridisation in this system, we only observe coupling of the individual modes between the solid and aperture as mentioned above. We will explore hybridisation again for the more complex shuriken geometry.

To finish off our initial study of the dimple rod systems we simulated the systems as a function of depression depth and gap distance. The energy loss spectrum for the connected dimple structure in figure 5.3(a) has two broad peaks at roughly 2.15 eV and 2.35 eV, where other modes may be degenerate in this energy range but are not resolvable [157]. We again set up the dimple simulation model with a rod indentation geometry but we have tested the plasmonic properties as a function of depression depth. We expected to see out-of-plane interactions between the upper and lower surfaces as the depression depths increases, and the surfaces are moved closer together [34]. We begin, just as above, with a fully connected system consisting of a 700 nm out diameter nanodisk, and a nanorod inner

geometry with dimensions of 200x40 nm; thickness 25 nm. The nanorod geometry is then shifted in the z-direction whilst still maintaining a fully connect structure - cross-sectional schematic of the tested model shown in the right hand side of figure 5.5(a). Depression depths tested here range from 0 nm to 24 nm. For the largest depression depth, there is a 1 nm gap between the upper-inner surface and outer-lower surface - this is due to the limitations in the calculation method (boundary surfaces too close will produce erroneous results). Shown in figure 5.5(a) are the resulting energy loss spectra for each dimple depth with the simulation model shown as an insert. In examining each spectrum, we observe that there is no drastic change in the plasmonics of the system, even when the simulation is push to limits we are physically incapable of achieving (1 nm distance between the upper and lower surfaces would be near-impossible to control). We see a red shift in energy for the 3rd peak as the depression depth is increased, and a new peak is observed for the spectrum with the largest depression depth. However due to the non-physical nature of this model (distance between the upper and lower layers would be impossible to control when fabricating such a device) this was not used as the connected dimple model set-up. From these simulations we can deduce that the depression depths examined here show no severe changes to the plasmonics, only some mode splitting is observed at the extremes of the simulations.

The energy loss spectra as a function of increasing gap distance for the fully disconnected model is shown in figure 5.5(b). The separation distance ranges from 2 nm to 54 nm, which is an adequate range to explore the coupling between the two systems. 2 nm is the minimum distance possible in this model as this is the limits of the simulation software. Smaller gaps were tested but the resulting energy loss spectrum contained negative energy

loss probabilities - which is non-physical. Each spectrum in figure 5.5(b) hosts 6 peaks, but there are energy shifts with some peaks as a function of gap distance. The blueshift in energies for the peaks below 2 eV is observed as a function of increasing gap distance; no significant change in energy in modes greater than 2 eV is observed. Mode splitting and increased degeneracy for modes below 2 eV is also observed, the reason being that the coupled system with a small gap is becoming a separate solid-aperture composite with no interaction between the two. Therefore the resulting spectrum is a linear combination of the individual spectra for the components of the model. The results presented in figure 5.5(b) validate the choices made for the model shown in figure 5.3.

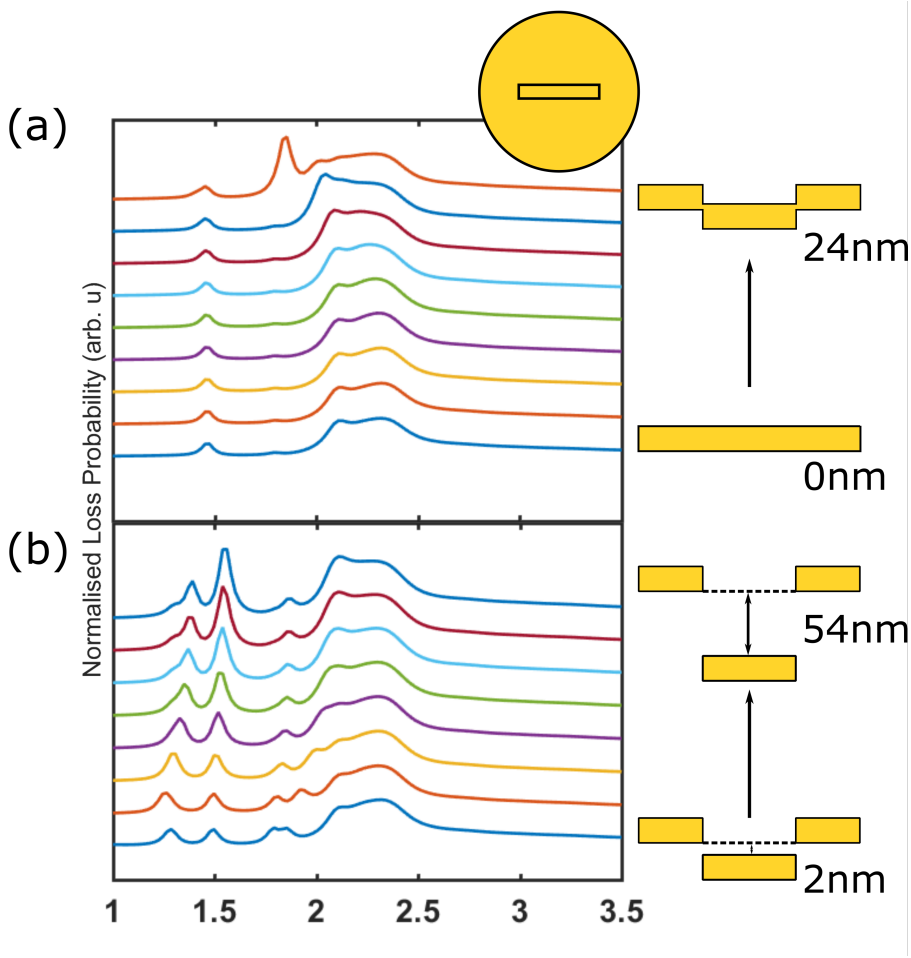

Figure 5.5: *(a) Simulated EEL spectra for a connected dimple structure using a rod geometry. Depression depths ranges from* 0 *nm to* 24 *nm, where the latter has a* 1 *nm gap between the upper-inner layer and lower-outer layer. (b) Spectra for a disconnected system with increasing gap distance, ranging from* 2 *nm to* 54 *nm. Cross-sectional schematic of the simulation model is shown as an inset.*

The results presented above gives us a 'rule of thumb' as to what to expect with more complex geometries. We have seen that the interaction between the solid and aperture modes in a disconnected dimple system are responses to individual modes excited by the separate parts. We can then expect to see no hybridisation in the similar shuriken systems.

Plasmon resonances for the solid nanorod are generated across the length of the structure, as opposed to the aperture where they are generated across the width. We can expect a similar result for each arm of the shuriken.

5.3 Shuriken Geometry

Having derived simple rules of thumb from the rod geometry and gaining an understanding of the coupling in the simulated dimple models, we now turn to a more complex geometry. Shuriken chiral structures are of interest in biodetection applications [144], a schematic of such a device is shown in figure 5.5, adapted from [3]. We have expanded on the model shown in the previous section by applying the same systematic breakdown of the dimple structures into solid, aperture, and both connected and disconnected structures. The dimensions used in building this model are given in figure 5.1, however we examine thinner samples comparedto the samples in [3] due to STEM examination limitations (see section 2.3 for details). For the outer disk diameter we are limited by the size of the disk making up the structure - we will use a 700 nm diameter as before based on the testing mentioned above. Shown in figure 5.6(a) are the resulting energy loss spectra for a solid, aperture, connected and disconnected dimple structures with corresponding energy loss maps for each peak shown in figure 5.6(b). A simple schematic of each model is given in figure 5.6(a), aligned horizontally with the relevant spectrum. We identify each mode in a similar manner as before where each peak is given a label $S_{X,Y}$. X and Y are defined above, and S indicates the results for the shuriken geometry.

Solid and aperture shuriken structures have a lot more plasmonic modes compared to

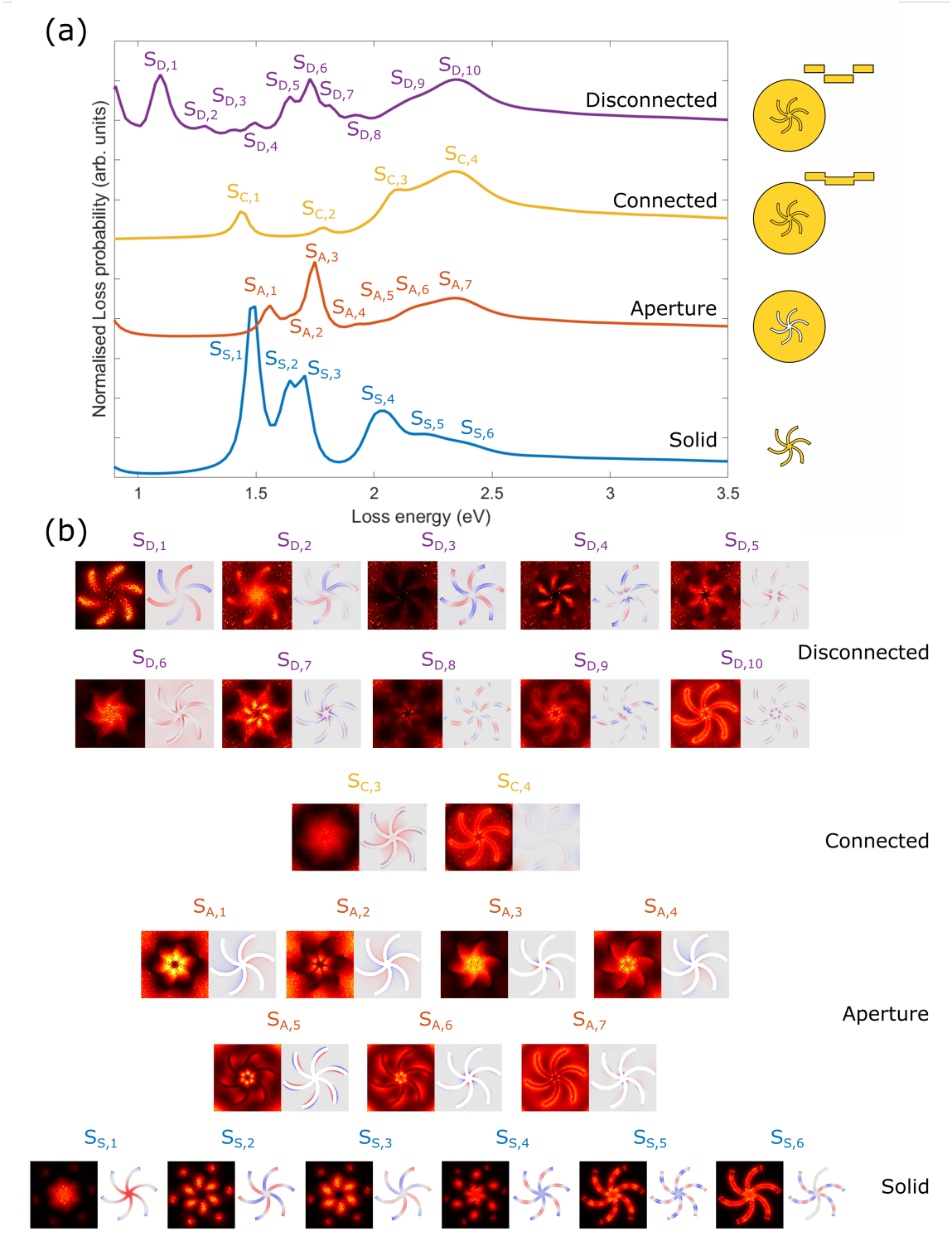

Figure 5.6: *Simulated EEL spectra (a) for a solid, aperture, connected and disconnected dimple structures using a shuriken geometry. Each observable peak in (a) is represented as energy loss map in (b), labelled accordingly.*

the rod geometry shown in figure 5.3(a), which underpins their use in practical devices. In the solid spectrum in figure 5.6(a), shown in blue, we observe 6 distinguishable peaks corresponding to the energy loss maps and eigenmodes in figure 5.6(b). Each of these maps are highly complex in their nature, but we will identify each plasmon resonance by the number of modes seen in each arm of the shuriken geometry. $S_{S,1}$, $S_{S,2}$ and $S_{S,3}$ in figure 5.6(b) have two modes in each arm in both the energy loss maps and eigenmodes. When we compare to the solid rod modes in figure 5.3(b) we see that each arm in modes $S_{S,1}$, $S_{S,2}$ and $S_{S,3}$ has a mode similar to $R_{S,1}$. We also understand that mode $S_{S,1}$ is a breathing mode,highlighted in the eigenmode (similar to that of a breathing mode of a disk, seen in section 2.1). $S_{S,2}$ and $S_{S,3}$ look very similar in their distributions, where the excitations only appear at the start and the end of the arm and not in the centre of the geometry. However the eigenmodes reveal that these are a second order hexapole mode and a second order dipole mode, respectively. Mode $S_{S,4}$ has three modes generated at the centre, middle and end of each arm, similar to the rod mode $R_{S,2}$. The final two peaks, $S_{S,5}$ and $S_{S,6}$, for the solid shuriken spectrum have highly complex energy loss maps, with a large number modes in each arm observed for both maps. Each plasmonically active arm in modes $S_{S,5}$ and $S_{S,6}$ are similar to the $R_{A,3}$ mode shown in figure 5.3(b). From the eigenmodes of both modes we understand that $S_{S,5}$ is a similar distribution to $S_{S,4}$, with an additional mode in each arm. $S_{S,6}$ eigenmode show activity in 4 out of the 6 of the arms, with four modes in each. A full symmetry analysis has been carried out on these solid shuriken structures, presented in reference [158], where the author provides insight into the available modes through a purely theoretical standpoint. The author shows that the C_{6h} symmetric shuriken structures can host a number of symmetric and anti-symmetric modes

using an argument based on geometry and group theory. When comparing the work shown in reference [158] to the solid shuriken dataset in figure 5.6 there is some corroboration in the modes. However, due to the differences in sizes (sample thickness in [158] is greater than the model shown here), we do not observe the lower order modes, namely the first order quadrupole and dipole modes.

The aperture results are shown in figure 5.6(a) as the orange spectrum where each peak is labelled. Corresponding energy loss maps and eigenmodes for each peak are shown in figure 5.6(b). Here we will define each plasmon resonance by the number of modes seen each region between the arms. $S_{A,1}$ and $S_{A,2}$ contain one mode in this region, as can be seen in the energy loss map and the eigenmodes. $S_{A,1}$ has resonances of a dipole mode shown in the corresponding eigenmode, where as $S_{A,2}$ is a hexapole mode with each adjacent arm having opposing charges. In comparing $S_{A,1}$ and $S_{A,2}$ to the aperture modes in figure 5.3(b) we can see that each arm behaves as a $R_{A,1}$ mode, i.e. the polarisation is across the aperture. $S_{A,3}$, $S_{A,4}$ and $S_{A,5}$ all contain two modes in each region between each arm. In the relevant energy loss maps shown in figure 5.6(b) we see that $S_{A,3}$ has intense regions on the tips of the arms. From the $S_{A,3}$ we understand that this mode is a second order hexapole mode, and in comparing to the complimentary rod aperture dataset we understand that each arm in the shuriken acts as a $R_{A,2}$ mode. $S_{A,4}$ eigenmodes shows that this is a second order dipole mode similar to $S_{A,1}$. $S_{A,5}$ eignemode has intense regions along the width of the arm which does not corroborate with the energy loss maps (intense regions in the tips of the arms). Both $S_{A,4}$ and $S_{A,5}$ modes contain a $R_{A,1}$ in each arm. $S_{A,6}$ and $S_{A,7}$ contain 3 modes in each region where both have regions of high intensity at the centre of the shuriken as seen in the corresponding maps and eigenmodes. Mode

$S_{A,7}$ is highly complex, where the energy loss map shows that the plasmon resonances is generated around the perimeter of the shuriken geometry. When comparing modes $S_{A,6}$ and $S_{A,7}$ to figure 5.3(b) we can see that $S_{A,6}$ behaves as a $R_{A,2}$, however the distribution in each arm of $S_{A,7}$ does not have a corresponding mode shown in the rod dataset.

Examining the connected dimple structures reveals similar results seen of the dimple-rod system. Only 4 modes are observed in yellow spectrum shown in figure 5.6(a), exactly as we seen in figures 5.3(a) and 5.5. The two lowest energy peaks, $S_{C,1}$ and $S_{C,2}$, correspond to plasmon resonances generated on the outer edge of the large disk structure. The energy loss maps and eigenmodes are not shown in figure 5.6(b). The remaining two higher energy modes, $S_{C,3}$ and $S_{C,4}$, are excited over broad, overlapping peaks which show resonances on the inner part of the geometry when examining the corresponding energy loss maps. The eigenmodes of these $S_{C,3}$ and $S_{C,4}$ show that these are resonances dominated by the outer disk - with some intensity for the inner dimple geometry. $S_{C,3}$ is a breathing mode very similar to $R_{C,3}$. $S_{C,4}$ is a disk mode with only slight, faint intensity in the corresponding eigenmode. When we come to examine the disconnected dimple structure, we will explore the concept of these modes potentially hybridising/out-of-plane coupling with the modes observed for the solid structure. Here, however, we observe little to no geometry-dependent plasmon energies when examining the simulated EELS data. The energies of the connected dimple energy loss spectrum shown in figure 5.6(a) is near identical to the spectrum seen in figure 5.3(a) of the similar connected model. Large discrepancies lie within the comparative simulation software capabilities. As explained in section 2.1, the MATLAB based simulation toolbox used throughout this thesis is MNPBEM. Due to the boundary elemental calculations and limitations in memory avail-

able to MATLAB, we are hindered by the number of faces/nodes able to be used in the calculations. Therefore the outer diameter for the aperture, connected and disconnect models is limited to 700 nm. The simulation work carried out in reference [3] use COMSOL Multiphysics, a finite element method calculation software [159]. COMSOL is unable to perform electron energy loss calculations (hence not considered in this work), however it is able to perform optical excitation calculations over much larger geometries. This would result in difference between the work shown here and that shown in reference [3]. Due to time constraints and unforeseen complications in the fabrication process, experimental comparison was not able to be made here but would be part of future projects.

Lastly, the purple spectrum shown in figure 5.6(a) is the disconnected dimple structures which has a vast amount of plasmon activity over this energy range. In the first instance, examining the number of distinct plasmon resonances provides insight into how applicable this structure could be in biodetection [14, 146]. A large number of distinct peaks could be used in detecting certain proteins of a given energy [145]. Ten distinct peaks are observed here, each of which corresponding to the appropriately labelled energy loss maps shown in figure 5.6(b). By employing the same technique used in section 5.2 to examine the disconnected dimple structure, we calculate the charge distributions created by the incoming incident electron beam, whilst energetically and spatially match these to the eigenmodes and energy loss maps given in figure 5.6(b). The resulting distributions are shown in figure 5.7, numbered in the same manner as shown above.

There is a large amount of information in the images of figure 5.7 which is necessary to understand the hybridisation and coupling model in the disconnected dimple system. Mode $S_{D,1}$ from examining the features in the charge distribution is a hexapole plasmon

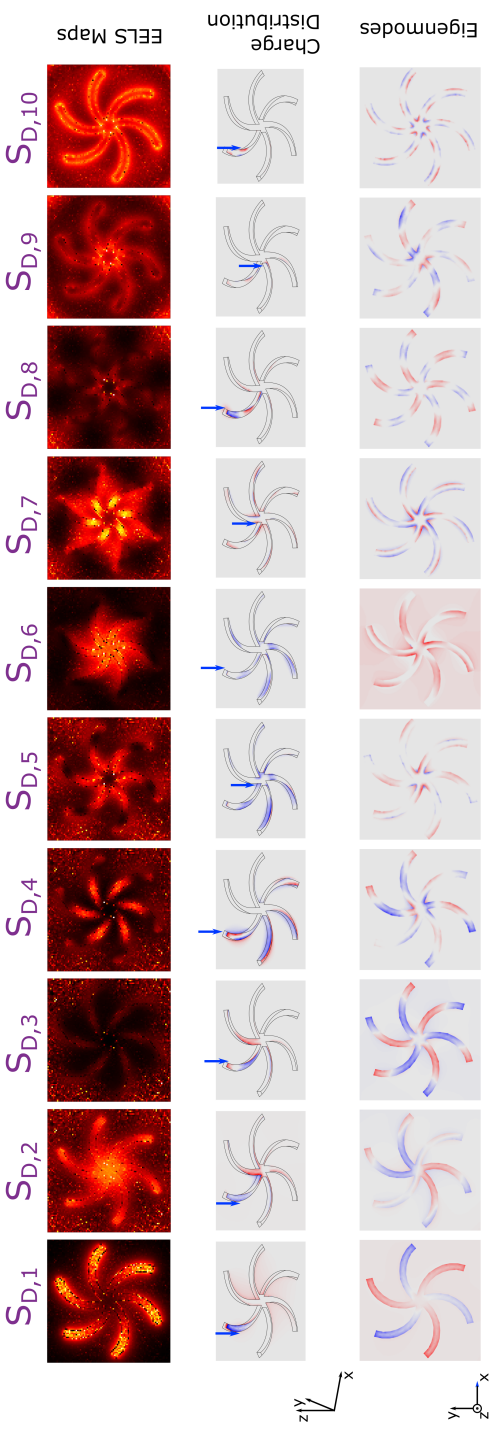

Figure 5.7: *Simulated EEL maps corresponding to the peaks observed in the shuriken-disconnected spectrum in figure 5.7(a). Each energy loss map has an associated charge distribution which is calculated using the electron impact given by the blue arrow in each figure. Eigenmodes are also calculated and matched energetically and spatially to the charge distributions and energy loss maps.*

resonance generated by the solid structure. This plasmon mode was not observed for the isolated solid structure seen in figure 5.6, but with the inclusion of the upper aperture it is now observable (due to a loss of degeneracy or energy shifting which can only be examined by simulating over a larger energy range or increasing the energy resolution). Modes $S_{D,2}$, $S_{D,3}$ and $S_{D,4}$ are similar in their number of resonances per arm of the solid structure, with two modes seen in each.

Eigenmodes of $S_{D,2}$ and $S_{D,4}$ show prominent modes for four of the arms, however the charge distribution for $S_{D,4}$ shows a clear coupling between the solid and aperture which is more prominent than in $S_{D,2}$. On closer inspection of $S_{D,2}$ we understand that this the coupling between the $S_{A,1}$ aperture mode with the $S_{S,3}$ solid mode (the aperture features in 5.6 are quite weak but this mode does exist). The eigenmode of $S_{D,3}$ shows that this mode is a second order hexapole mode in the solid component, $S_{S,2}$, coupled to a hexapole mode in the aperture component, $S_{A,2}$. However the energy loss map is quite weak in intensity (as is the corresponding peak shown in figure 5.6(a)) in comparison to the other maps shown here. Here, we observe coupling between the lower solid structure and the upper aperture in eigenmode of $S_{D,4}$. This mode is a $S_{S,3}$ mode in the solid structure coupled to a mode we did not observe in the aperture.

Mode $S_{D,5}$ is the lowest energy mode which shows charge distribution across the width of the arm (as opposed to the length of the arm which we have seen with the lower energy modes). From the eigenmode we also observe coupling between the solid and aperture seen in the centre of the structure. Mode $S_{D,6}$ is an outlier in the results which is due to a non-physical, highly-localised pinning of the mode not observable in this set of results. The charge distribution and eigenmode of $S_{D,6}$ show generally one charge (one colour)

throughout the entire structure; this is not correct. Further inspection revealed that the calculation was highly localised to one of the corners of the aperture, confirming the result as invalid. Mode $S_{D,7}$ contains four modes in each arm generated across the width of the arm seen in the eigenmodes, similar the resonances seen for $S_{D,5}$. Here, again, we observe some coupling between the upper and lower structures in the centre. $S_{D,8}$ is a third order hexapole mode with three modes generated in each arm. The energy loss maps show a highly localised intensity in the inner regions of the geometry. After examination this is due to the edges of the aperture structure. Modes $S_{D,9}$ and $S_{D,10}$ are highly complex, with both energy loss maps showing resonances around the perimeter of the shuriken geometry. From the respective eigenmodes and charge distributions we see that both of these maps show coupling between the upper and lower structures, again positioned in the centre as we have seen for modes $S_{D,4}$, $S_{D,5}$ and $S_{D,7}$.

The coupling shown here in the disconnected dimple structures, for both the shuriken and rod geometries, does not abide by the Prodan hybridisation model [1], described in section 1.2, formed using Babinet's principle. Coupling shown in figures 5.4 and 5.7 is generated by one component responding to the plasmon mode of the other. The coupling observed for the shuriken disconnected dimple structure between the upper and lower components alludes to the biodetection capabilities shown in references [14, 145, 146]; biodetection mechanism comes from coupling between optically bright and dark modes. We hypothesise that the coupling described above is the detection mechanisms shown in the biodetectors [14, 145, 146], however in order to confirm this, optical simulations must be carried out - omitted here due to time constraints. Experimental EELS is also needed to corroborate the findings presented here but again due to time constraints experimental

analysis was not able to be carried out.

5.4 Conclusion

In this work we have tested the plasmon resonances of highly complex systems using simulated electron energy loss spectroscopy. We looked at both rod and shuriken geometries in solid, aperture, connected and disconnected dimple structures in order to further examine the plasmonics of the models shown in references [3, 14, 146] where optical excitations are used as opposed to electrons here. Having broken down the dimple shuriken structure into solid and aperture components, and simplifying the geometry to a rod, we were able to create a rule-of-thumb for the plasmonics expected in the more complex structure. We were then able to conclude that the coupling for both the rod and shuriken structure is not based upon Prodan's hybridisation model using Babinet's principle, but rather it is an individual response to the plasmon mode generated in the counterpart of the system. We understand this as there is no symmetric coupling between the upper and lower components of the model seen in the charge distributions for both the rod and shuriken geometries as one would expect from Babinet's principle, a schematic of which is shown in figure 5.2. The work shown here indicates that the plasmon systems in references [3, 14, 146] behave more like our disconnected dimple model rather than the connected dimples. More importantly, we were able to show that coupling between that upper and lower parts of the disconnected dimple structure does occur, as hypothesised in the literature. This work has built the platform to study complex shuriken dimple structures using EELS, which will illuminate the plasmonic characteristics of these biodetection devices.

CHAPTER 6

CONCLUSION & OUTLOOK

In this thesis we have explored a number of avenues regarding plasmonic excitations of nanostructures using both experimental and simulated techniques. We have provided further insight into a number of areas in the field of plasmonic research whilst creating a platform for further work to be carried out. Chapter 3 was centred around examining prototypical NFT geometries in order to understand their plasmonic properties for near-field applications such as HAMR. The energetically and spatially resolved plasmon modes for two geometries, nanoraindrop and nanolollipop, provided insight into the advantages and disadvantages of both structures. We then studied the tuning capabilities of the proposed annular plasmonic model. This was tested using nanodisk and nanoraindrop geometries by looking at both the hole diameter and position within the NFT. We showed that this model had a tunable energetic window of 0.3eV for both geometries, as we change the hole diameter. Accentuation of the plasmon resonances was also shown as we displaced the hole

from the centre of the NFT to the edge of a nanodisk, and to the apex of the nanoraindrop geometry. For the latter, we highlighted the usefulness of this model as a viable HAMR NFT design due to the increased resonance energy for the shifted annular nanoraindrops.

Chapter 4 carries on from the work in chapter 3 as we increased the complexity of the experimental system by encapsulating the nanostructures in a dielectric environment and studied the effect of annealing on the NFTs. For the dielectric examination we had to carry out an intricate sample preparation in order to examine the plasmonic properties of encapsulate NFTs and were able to resolve the dipole plasmon mode of the structures using STEM EELS. Annealing of the NFTs was carried out both in-situ and ex-situ to examine its effects on the plasmonic and structure of our fabricated samples. We showed that the change in granularity due to annealing caused slight changes in the plasmonic properties of our nanoraindrop structures. This could play some role in defining the efficiency and heating capability of the NFTs as the coupling efficiency between the laser light source and the nanostructure could decrease.

As illustrated in section 2.2, a large amount of work was carried out on fabrication of NFTs on top of dedicated heating chips that can be used in the DENS Solution Wildfire heating rod [57]. Due to time constraints the fabrication process was not optimised enough to allow for STEM EELS to be carried out. Annealing of NFTs in-situ whilst performing STEM EELS would offer great insight into the performance of NFTs when exposed to high temperatures (as they would be in HAMR applications) and would be the next step to the work presented in chapter 4, section 4.2.

In chapter 5 we examined the effect of coupling between solid and aperture nanostructures using the MNPBEM software package, and illustrated the interaction between

disconnected and connected dimple structures for rod and shuriken geometries. Using Babinet's principle as a basis for our argument, we revealed that the coupling between two separate solid and aperture structures was a reactionary interaction rather than a hybridised system, as previously thought. We also highlighter the possible protein detection mechanism in the disconnected dimple structure using the shuriken geometry, as the higher order modes of the solid nanostructure induce plasmon modes in the aperture. However, to confirm this as the biodetection mechanism we need to perform optical excitation simulations which would be a part for future work. Another area for further research would be the fabrication and examination of dimple structures to corroborate the results provided in this thesis. The work carried out in chapter 5 is the groundwork for further study into these chiral biodetectors.

BIBLIOGRAPHY

[1] E. Prodan, C. Radloff, N. J. Halas, and P. Nordlander. A Hybridization Model for the Plasmon Response of Complex Nanostructures. *Science*, 302(5644):419–422, 2003.

[2] M. Haruta, Y. Fujiyoshi, T. Nemoto, A. Ishizuka, K. Ishizuka, and H. Kurata. Extremely low count detection for EELS spectrum imaging by reducing CCD read-out noise. *Ultramicroscopy*, 207:112827, 2019.

[3] A. S. Karimullah, C. Jack, R. Tullius, V. M. Rotello, G. Cooke, L. D. Gadegaard, N.and Barron, and M. Kadodwala. Disposable Plasmonics: Plastic Templated Plasmonic Metamaterials with Tunable Chirality. *Advanced Materials*, 27(37):5610–5616, 2015.

[4] M. Aubert. *Les Vitraux de Notre-Dame et de la Sainte-Chapelle de Paris*. Caisse Nationale des Monuments Historiques, 1959.

[5] R.W. Wood. XLII. On a remarkable case of uneven distribution of light in a diffraction grating spectrum. *The London, Edinburgh, and Dublin Philosophical Magazine and Journal of Science*, 4(21):396–402, 1902.

[6] J. Zenneck. Über die fortpflanzung ebener elektromagnetischer wellen längs einer ebenen leiterfläche und ihre beziehung zur drahtlosen telegraphie. *Annalen der Physik*, 328(10):846–866, 1907.

[7] R. H. Ritchie. Plasma losses by fast electrons in thin films. *Phys. Rev.*, 106:874–881, Jun 1957.

[8] C. J. Powell and J. B. Swan. Origin of the characteristic electron energy losses in magnesium. *Phys. Rev.*, 116:81–83, Oct 1959.

[9] C. J. Powell and J. B. Swan. Effect of oxidation on the characteristic loss spectra of aluminum and magnesium. *Phys. Rev.*, 118:640–643, May 1960.

[10] F. J. García de Abajo. Optical excitations in electron microscopy. *Rev. Mod. Phys.*, 82:209–275, Feb 2010.

[11] R. F. Egerton. Electron energy-loss spectroscopy in the TEM. *Reports on Progress in Physics*, 72(1):016502, dec 2008.

[12] N. L. Rosi and C. A Mirkin. Nanostructures in biodiagnostics. *Chemical Reviews*, 105(4):1547–1562, 2005.

[13] A. J. Haes and R. P. Van Duyne. A nanoscale optical biosensor: Sensitivity and selectivity of an approach based on the localized surface plasmon resonance spectroscopy of triangular silver nanoparticles. *Journal of the American Chemical Society*, 124(35):10596–10604, 2002.

[14] R. Tullius, A. S. Karimullah, M. Rodier, B. Fitzpatrick, N. Gadegaard, L. D. Barron, V. M. Rotello, G. Cooke, A. Lapthorn, and M. Kadodwala. "Superchiral" Spectroscopy: Detection of Protein Higher Order Hierarchical Structure with Chiral Plasmonic Nanostructures. *Journal of the American Chemical Society*, 137(26):8380–8383, 2015.

[15] Y. H. Jang, Y. J. Jang, S. Kim, L. N. Quan, K. Chung, and D. H. Kim. Plasmonic Solar Cells: From Rational Design to Mechanism Overview. *Chemical Reviews*, 116(24):14982–15034, 2016.

[16] S. Mubeen, J. Lee, W. R. Lee, N. Singh, G. D. Stucky, and M. Moskovits. On the plasmonic photovoltaic. *ACS Nano*, 8(6):6066–6073, 2014.

[17] IDC: Data Age 2025 . Accessed: 20/04/2020.

[18] S. Iwasaki. Perpendicular magnetic recording–its development and realization. *Proceedings of the Japan Academy. Series B, Physical and biological sciences*, 85(2):37–54, 2009.

[19] S. Chikazumi. *Physics of Ferromagnetism*. Oxford Univ. Press, New York, 1997.

[20] W. A. Chandler et al. Heat-assisted magnetic recording by a near-field transducer with efficient optical energy transfer. *Nature Photonics*, 3:220–224, 2009.

[21] M. H. Kryder. Heat assisted magnetic recording. *Proc. IEEE*, 96:1810–1835, 2008.

[22] S. A. Maier. *Plasmonics: Fundamentals and Applications*. Springer, 2007.

[23] A. Derkachova, K. Kolwas, and I. Demchenko. Dielectric Function for Gold in Plasmonics Applications: Size Dependence of Plasmon Resonance Frequencies and Damping Rates for Nanospheres. *Plasmonics*, 11(3):941–951, 2016.

[24] M. R. Vogt. *Development of Physical Models for the Simulation of Optical Properties of Solar Cell Modules*. PhD thesis, 11 2015.

[25] C. Colliex and M. Kociak. Electron energy loss spectroscopy imaging of surface plasmons at the nanometer scale. *Ultramicroscopy*, 162:A1–A24, 2015.

[26] I. Schubert, W. Sigle, and P. A. van Aken. STEM-EELS analysis of multipole surface plasmon modes in symmetry-broken AuAg nanowire dimers. *Nanoscale*, 7:4935–4941, 2015.

[27] N. Geuquet and L. Henrard. EELS and optical response of a noble metal nanoparticle in the frame of a discrete dipole approximation. *Ultramicroscopy*, 110:1075–1080, 2010.

[28] X. Zhou et al. Effect of multipole excitations in electron energy-loss spectroscopy of surface plasmon modes in silver nanowires. *Journal of Applied Physics*, 116, 2014.

[29] A. Trügler. *Optical properties of metallic nanoparticles*. Springer, 2011.

[30] A. A. Maradudin, J. R. Sambles, and W. L. Barnes. *Modern Plasmonics*. Elsevier, 2014.

[31] M. Hentschel, M. Schäferling, X. Duan, H. Giessen, and N. Liu. Chiral plasmonics. 3(5), 2017.

[32] R. Winkler, F. P. Schmidt, U. Haselmann, J. D. Fowlkes, B. B. Lewis, G. Kothleitner, P. D. Rack, and H. Plank. Direct-Write 3D Nanoprinting of Plasmonic Structures. *ACS Applied Materials and Interfaces*, 9(9):8233–8240, 2017.

[33] J. S. Huang, J. Kern, P. Geisler, P. Weinmann, M.and Forchel Kamp, P. Biagioni, and B. Hecht. Mode imaging and selection in strongly coupled nanoantennas. *Nano Letters*, 10(6):2105–2110, 2010.

[34] A. B. Yankovich, R. Verre, E. Olsén, A. Persson, V. Trinh, G. Dovner, M. Käll, and E. Olsson. Multidimensional Hybridization of Dark Surface Plasmons. *ACS Nano*, 11(4):4265–4274, 2017.

[35] P. Nordlander. The ring: A leitmotif in plasmonics. *ACS Nano*, 3(3):488–492, 2009.

[36] M. M. Mirza, D. A. MacLaren, A. Samarelli, B. M. Holmes, H. Zhou, S. Thoms, D. MacIntyre, and D. J. Paul. Determining the electronic performance limitations in top-down-fabricated Si nanowires with mean widths down to 4 nm. *Nano Letters*, 14(11):6056–6060, 2014.

[37] U. Hohenester J. Waxenegger, A. Trügler. Plasmonics simulations with the MNPBEM toolbox: Consideration of substrates and layer structures. *Computer Physics Communications*, 193:138–150, 2015.

[38] U. Hohenester. Simulating electron energy loss spectroscopy with the MNPBEM toolbox. *Computer Physics Communications*, 185:1177–1187, 2014.

[39] U. Hohenester and A. Trügler. MNPBEM – a matlab toolbox for the simulation of plasmonic nanoparticles. *Computer Physics Communications*, 183(2):370 – 381, 2012.

[40] F. J. García de Abajo and A Howie. Retarded field calculation of electron energy loss in inhomogeneous dielectrics. *Physical Review B*, 65(11):115418, 2002.

[41] F. Hofer J. R. Krenn U. Hohenester F. P. Schmidt, H. Ditlbacher. Morphing a plasmonic nanodisk into a nanotriangle. *Nano Letters*, 14:4810–4815, 2014.

[42] D. Grieser, H. Uecker, S. A. Biehs, O. Huth, F. Rüting, and M. Holthaus. Perturbation theory for plasmonic eigenvalues. *Physical Review B - Condensed Matter and Materials Physics*, 80(24):1–8, 2009.

[43] G. Brockt and H. Lakner. Nanoscale EELS analysis of dielectric function and bandgap properties in GaN and related materials. *Micron*, 31(4):435–440, 2000.

[44] M. Valamanesh, Y. Borensztein, C. Langlois, and E. Lacaze. Substrate effect on the plasmon resonance of supported flat silver nanoparticles. *The Journal of Physical Chemistry C*, 115(7):2914–2922, 2011.

[45] S. Kadkhodazadeh, T. Christensen, M. Beleggia, N. A. Mortensen, and J. B. Wagner. The substrate effect in electron energy-loss spectroscopy of localized surface plasmons in gold and silver nanoparticles. *ACS Photonics*, 4(2):251–261, 2017.

[46] M. Duval Malinsky, K. L. Kelly, G. C. Schatz, and R. P. Van Duyne. Nanosphere lithography effect of substrate on the localized surface plasmon resonance spectrum of silver nanoparticles. *The Journal of Physical Chemistry B*, 105(12):2343–2350, 2001.

[47] A. P. Mousinho, R. D. Mansano, L. S. Zambom, and A. Passaro. Low temperature deposition of low stress silicon nitride by reactive magnetron sputtering. *Journal of Physics: Conference Series*, 370(1), 2012.

[48] O. Nicoletti and R. Leary F. de la Peña and. Three-dimensional imaging of localized surface plasmon resonances of metal nanoparticles. *Nature*, 502:80–84, 2013.

[49] M. A. Mahmoud, M. Chamanzar, A. Adibi, and M. A. El-Sayed. Effect of the dielectric constant of the surrounding medium and the substrate on the surface plasmon resonance spectrum and sensitivity factors of highly symmetric systems: Silver nanocubes. *Journal of the American Chemical Society*, 134(14):6434–6442, 2012.

[50] J. Lermé, H. Baida, C. Bonnet, M. Broyer, E. Cottancin, A. Crut, P. Maioli, N. Del Fatti, F. Vallée, and M. Pellarin. Size dependence of the surface plasmon resonance damping in metal nanospheres. *Journal of Physical Chemistry Letters*, 1(19):2922–2928, 2010.

[51] G. W. Paterson, A. S. Karimullah, S. G. Smith, M. Kadodwala, and D. A. MacLaren. Symmetry reduction and shape effects in concave chiral plasmonic structures. *The Journal of Physical Chemistry C*, 122(9):5049–5056, 2018.

[52] N. Pala and M. Karabiyik. *Electron Beam Lithography (EBL)*, pages 1033–1057. Springer Netherlands, Dordrecht, 2016.

[53] T. Kerdcharoen and C. Wongchoosuk. 11 - carbon nanotube and metal oxide hybrid materials for gas sensing. In Raivo Jaaniso and Ooi Kiang Tan, editors, *Semiconductor Gas Sensors*, Woodhead Publishing Series in Electronic and Optical Materials, pages 386 – 407. Woodhead Publishing, 2013.

[54] M. Todeschini, A. Bastos Da Silva Fanta, F. Jensen, J. B. Wagner, and A. Han. Influence of Ti and Cr Adhesion Layers on Ultrathin Au Films. *ACS Applied Materials and Interfaces*, 9(42):37374–37385, 2017.

[55] S. J. Madsen, M. Esfandyarpour, M. L. Brongersma, and R. Sinclair. Observing plasmon damping due to adhesion layers in gold nanostructures using electron energy loss spectroscopy. *ACS Photonics*, 4(2):268–274, 2017.

[56] T. P. Almeida, A. R. Muxworthy, A. Kovács, W. Williams, P. D. Brown, and R. E. Dunin-Borkowski. Direct visualization of the thermomagnetic behavior of pseudo–single-domain magnetite particles. *Science Advances*, 2(4), 2016.

[57] DENS Solutions - Wildfire . https://denssolutions.com/products/wildfire/.

[58] R. F. Egerton. *Electron Energy-Loss Spectroscopy in the Electron Microscope*. Springer, 1986.

[59] D. Richards. Near-field microscopy: Throwing light on the nanoworld. *Philosophical transactions. Series A, Mathematical, physical, and engineering sciences*, 361:2843–57, 01 2004.

[60] P. Klapetek. In *Quantitative Data Processing in Scanning Probe Microscopy, Chapter 12 - Optical Measurements*, Micro and Nano Technologies, pages 265 – 293. 2013.

[61] C. B. Carter D. B. Williams. *Transmission Electron Microscopy*. Springer, 1996.

[62] H. Kohl L. Reimer. *Transmission Electron Microscopy*. Springer, 2008.

[63] R. Shiloh, R. Remez, P. H. Lu, L. Jin, Y. Lereah, A. H. Tavabi, R. E. Dunin-Borkowski, and A. Arie. Spherical aberration correction in a scanning transmission electron microscope using a sculpted thin film. *Ultramicroscopy*, 189:46 – 53, 2018.

[64] C. Hetherington. Aberration correction for tem. *Materials Today*, 7(12):50 – 55, 2004.

[65] O. Scherzer. The theoretical resolution limit of the electron microscope. *Journal of Applied Physics*, 20(1):20–29, 1949.

[66] P. D. Nellist. *The Principles of STEM Imaging. In: Pennycook S., Nellist P. (eds) Scanning Transmission Electron Microscopy*. Springer, 2011.

[67] N. D. Browning, M. F. Chisholm, and S. J. Pennycook. Atomic-resolution chemical analysis using a scanning transmission electron microscope. *Nature*, 366(6451):143–146, 1993.

[68] L. Giannuzzi and F. Stevie. *Introduction to Focused Ion Beams: Instrumentation, Theory, Techniques and Practice*. Springer, 2005.

[69] A. Gloter, V. Badjeck, L. Bocher, N. Brun, K. March, M. Marinova, M. Tencé, M. Walls, A. Zobelli, O. Stéphan, and C. Colliex. Atomically resolved mapping of EELS fine structures. *Materials Science in Semiconductor Processing*, 07 2016.

[70] J. Nelayah *et. al.* Mapping surface plasmons on a single metallic nanoparticle. *Nature Physics*, 3:348–353, 2007.

[71] J. L. Hart, A. C. Lang, A. C. Leff, P. Longo, C. Trevor, R. D. Twesten, and M. L. Taheri. Direct Detection Electron Energy-Loss Spectroscopy: A Method to Push the Limits of Resolution and Sensitivity. *Scientific Reports*, 7(1):1–14, 2017.

[72] D. A. Fish, A. M. Brinicombe, E. R. Pike, and J. G. Walker. Blind deconvolution by means of the richardson–lucy algorithm. *J. Opt. Soc. Am. A*, 12(1):58–65, Jan 1995.

[73] A. Gloter, A. Douiri, M. Tencé, and C. Colliex. Improving energy resolution of EELS spectra: an alternative to the monochromator solution. *Ultramicroscopy*, 96(3):385 – 400, 2003.

[74] J. E Krist. Deconvolution of hubble space telescope images using simulated point spread functions. *Astronomical Data Analysis Software and Systems*, 25:226, 1992.

[75] H. M. Adorf, R. N. Hook, and L. B. Lucy. Hst image restoration developments at the st-ecf. *International Journal of Imaging Systems and Technology*, 6(4):339–349, 1995.

[76] D. D. Lee and H. S. Seung. Learning the parts of objects by non-negative matrix factorization. *Nature*, 401(6755):788–791, 1999.

[77] R. Zhao and V. Y. F. Tan. Online nonnegative matrix factorization with outliers. *IEEE Transactions on Signal Processing*, 65(3):555–570, 2017.

[78] Michel Bosman, Enyi Ye, Shu Fen Tan, Christian A. Nijhuis, Joel K.W. Yang, Renaud Marty, Adnen Mlayah, Arnaud Arbouet, Christian Girard, and Ming Yong Han. Surface plasmon damping quantified with an electron nanoprobe. *Scientific Reports*, 3:1–7, 2013.

[79] Kumar Molugaram and G. Shanker Rao. Chapter 5 - curve fitting. In Kumar Molugaram and G. Shanker Rao, editors, *Statistical Techniques for Transportation Engineering*, pages 281 – 292. Butterworth-Heinemann, 2017.

[80] Miroslava Schaffer, Bernhard Schaffer, and Quentin Ramasse. Sample preparation for atomic-resolution STEM at low voltages by FIB. *Ultramicroscopy*, 114:62 – 71, 2012.

[81] L. Skoric, D. Sanz-Hernández, F. Meng, C. Donnelly, S. Merino-Aceituno, and A. Fernández-Pacheco. Layer-by-layer growth of complex-shaped three-dimensional nanostructures with focused electron beams. *Nano Letters*, 20(1):184–191, 2020.

[82] M. Horák, K. Bukvišová, V. Švarc, J. Jaskowiec, V. Křápek, and T. Šikola. Comparative study of plasmonic antennas fabricated by electron beam and focused ion beam lithography. *Scientific Reports*, 8(1):1–8, 2018.

[83] N. Zhou et al. Plasmonic near-field transducer for heat-assisted magnetic recording. *Nanophotonics*, 3:141–155, 2014.

[84] Pabitra Das, Hugo Lourenço-Martins, Luiz Henrique Galvão Tizei, Raphaël Weil, and Mathieu Kociak. Nanocross: A highly tunable plasmonic system. *The Journal of Physical Chemistry C*, 121(30):16521–16527, 2017.

[85] C. Peng and K. D. Ko. Lightning rod resonance of a plasmonic near-field transducer. *Opt. Express*, 25(13):14204–14209, Jun 2017.

[86] T. Zhao, M. C. Kautzky, W. C. Challener, and M. A. Seigler. HAMR NFT material with improved thermal stability, Aug 2011.

[87] X. Huang, E. Prairie, M. Kautzky, and Z. Jandric. Heat assisted magnetic recording devices. US 9,053,737 B2, 2015.

[88] K. Gao, X. Jin, and A. Goulakov. Write head with bevel structure and reverse NFT for HAMR, U.S. Patent 8,416,530 B2, Apr. 9 2013.

[89] K. Vossough, Xi. Zhang, A. Kirkakosian, J. Wang, T. Yuan, and Y. Hu. Method for providing a near-field transducer (NFT) for a heat assisted magnetic recording (HAMR) device, U.S. Patent 9,881,638 B1, Jan. 30 2018.

[90] F. P. Schmidt, H. Ditlbacher, U. Hohenester, A. Hohenau, F. Hofer, and J. R. Krenn. Dark plasmonic breathing modes in silver nanodisks. *Nano Letters*, 12(11):5780–5783, 2012.

[91] F. Hao, E. M. Larsson, T. A. Ali, D. S. Sutherland, and P. Nordlander. Shedding light on dark plasmons in gold nanorings. *Chemical Physics Letters*, 458(4):262 – 266, 2008.

[92] M. Kobylko *et. al.* Localized plasmonic resonances of prolate nanoparticles in a symmetric environment: Experimental verification of the accuracy of numerical and analytical models. *Physical Review Applied*, 9, 2018.

[93] J. Aizpurua, P. Hanarp, D. S. Sutherland, M. Kall, Garnett W. Bryant, and F. J. García de Abajo. Optical properties of gold nanorings. *Physical Review Letters*, 90(5):4, 2003.

[94] P. Liu, W.i Cai, L. Wang, X. Zhang, and J. Xu. Tunable terahertz optical antennas based on graphene ring structures. *Applied Physics Letters*, 100(15):153111, 2012.

[95] Léo Morel, Zhibin Yao, Pierre Cladé, and Saïda Guellati-Khélifa. Determination of the fine-structure constant with an accuracy of 81 parts per trillion. *Nature*, 588(7836):61–65, 2020.

[96] A. Colin Cameron and Frank A.G. Windmeijer. An r-squared measure of goodness of fit for some common nonlinear regression models. *Journal of Econometrics*, 77(2):329 – 342, 1997.

[97] P. F. Liao and A. Wokaun. Lightning rod effect in surface enhanced Raman scattering. *The Journal of Chemical Physics*, 76(1):751–752, 1982.

[98] Nicolas Geuquet and Luc Henrard. EELS and optical response of a noble metal nanoparticle in the frame of a discrete dipole approximation. *Ultramicroscopy*, 110(8):1075–1080, 2010.

[99] A. Aubry, D. Y. Lei, A. I. Fernández-Domínguez, Y. Sonnefraud, S. A. Maier, and J. B. Pendry. Plasmonic light-harvesting devices over the whole visible spectrum. *Nano Letters*, 10(7):2574–2579, 2010.

[100] E. Betzig *et. al.* Optical microscopy on a nanometric scale. *Science*, 251:1468–1470, 1991.

[101] B. Xu, Y. T. Toh, C. W. Chia, J. Li, J. Zhang, K. Ye, and C. An. Relationship between near field optical transducer laser absorption and its efficiency. *IEEE Transactions on Magnetics*, 48(5):1789–1793, 2012.

[102] P. Schlexer, A. B. Andersen, B. Sebok, I. Chorkendorff, J. Schiøtz, and T. W. Hansen. Size-Dependence of the Melting Temperature of Individual Au Nanoparticles. *Particle and Particle Systems Characterization*, 36(3):1–7, 2019.

[103] S. Inasawa, M. Sugiyama, and Y. Yamaguchi. Laser-induced shape transformation of gold nanoparticles below the melting point: The effect of surface melting. *Journal of Physical Chemistry B*, 109(8):3104–3111, 2005.

[104] U. Khan Jacek Gosciniak, J. J. and B. Corbett. Study of TiN nanodisks with regard to application for Heat-Assisted Magnetic Recording. *MRS Advances*, (January):1, 2016.

[105] A. A. Herzing, U. Guler, X. Zhou, V. Boltasseva, A.and Shalaev, and T. B. Norris. Electron energy loss spectroscopy of plasmon resonances in titanium nitride thin films. *Applied Physics Letters*, 108(17):171107, 2016.

[106] V Keast, R Barnett, and Michael Cortie. First principles calculations of the optical and plasmonic response of au alloys and intermetallic compounds. *Journal of physics. Condensed matter : an Institute of Physics journal*, 26:305501, 07 2014.

[107] A. S. Pavlovic. Some dielectric properties of tantalum pentoxide. *The Journal of Physical Chemistry*, 40(4), 1964.

[108] Z. Fei, A. S. Rodin, W. Gannett, S. Dai, W. Regan, M. Wagner, M. K. Liu, A. S. McLeod, G. Dominguez, M. Thiemens, Antonio H. Castro Neto, F. Keilmann, A. Zettl, R. Hillenbrand, M. M. Fogler, and D. N. Basov. Electronic and plasmonic phenomena at graphene grain boundaries. *Nature Nanotechnology*, 8(11):821–825, 2013.

[109] M. l. Bosman, L. Zhang, H. Duan, S. F. Tan, C. A. Nijhuis, C. W. Qiu, and J. Yang. Encapsulated annealing: Enhancing the plasmon quality factor in lithographically-defined nanostructures. *Scientific Reports*, 4:1–6, 2014.

[110] C. V. Thompson. Solid-State Dewetting of Thin Films. *Annual Review of Materials Research*, 42(1):399–434, 2012.

[111] Y. Erdogdu, T. Jian, G. V. Lopez, W. Li Li, and L. S. Wang. On the electronic structure and chemical bonding of titanium tetraauride: TiAu4 and TiAu4-. *Chemical Physics Letters*, 610-611:23–28, 2014.

[112] F. Leroy, Borowik, F. Cheynis, Y. Almadori, S. Curiotto, M. Trautmann, J. C. Barbé, and P. Müller. How to control solid state dewetting: A short review. *Surface Science Reports*, 71(2):391–409, 2016.

[113] W. M. Abbott, C. P. Murray, C. Zhong, C. Smith, C. McGuinness, E. Rezvani, C. Downing, D. Daly, A. K. Petford-Long, F. Bello, D. McCloskey, and J. F. Donegan. Less is more: Improved thermal stability and plasmonic response in Au films via the use of SubNanometer Ti Adhesion Layers. *ACS Applied Materials and Interfaces*, 11(7):7607–7614, 2019.

[114] M. Aliofkhazraei. Handbook of nanoparticles. pages 1–1426, 01 2015.

[115] E. Roduner. Size matters: Why nanomaterials are different. *Chemical Society Reviews*, 35(7):583–592, 2006.

[116] F. Niekiel, P. Schweizer, S. M. Kraschewski, B. Butz, and E. Spiecker. The process of solid-state dewetting of Au thin films studied by in situ scanning transmission electron microscopy. *Acta Materialia*, 90:118–132, 2015.

[117] W. D. Pyrz and D. J. Buttrey. Particle size determination using TEM: A discussion of image acquisition and analysis for the novice microscopist. *Langmuir*, 24(20):11350–11360, 2008.

[118] F. J. Humphreys and M. Harthley. *Recrystallization and related annealing phenomena.* Pergamon, 2004.

[119] J.E. Burke and D. Turnbull. Recrystallization and grain growth. *Progress in Metal Physics*, 3:220 – 292, 1952.

[120] F. Ruffino, M. G. Grimaldi, C. Bongiorno, F. Giannazzo, F. Roccaforte, V. Raineri, and C. Spinella. Normal and abnormal grain growth in nanostructured gold film. *Journal of Applied Physics*, 105(5):054311, 2009.

[121] W. Ostwald. Studien über die bildung und umwandlung fester körper. *Physikalische Chemie*, 22:289–330, 1897.

[122] I. M. Lifshitz and V. V. Slyozov. The kinetics of precipitation from supersaturated solid solutions. *Journal of Physics and Chemistry of Solids*, 19(1-2):35–50, 1961.

[123] C. J. Gommes. Ostwald ripening of confined nanoparticles: Chemomechanical coupling in nanopores. *Nanoscale*, 11(15):7386–7393, 2019.

[124] Tadao Sugimoto. Chapter 4 - recrystallization. pages 139 – 154. Elsevier, Amsterdam, 2001.

[125] F. Liebig, A. F. Thünemann, and J. Koetz. Ostwald Ripening Growth Mechanism of Gold Nanotriangles in Vesicular Template Phases. *Langmuir*, 32(42):10928–10935, 2016.

[126] K. E. MacArthur, N. P. Young, J. W. Critchell, and A. I. Kirkland. 'Ex-situ' annealing and structural transformations in gold nanoparticles. *Journal of Physics: Conference Series*, 371, 2012.

[127] A. L. Baudrion, F. de Leon-Perez, O. Mahboub, A. Hohenau, H. Ditlbacher, F. J. Garcia-Vidal, J. Dintinger, T. W. Ebbesen, L. Martin-Moreno, and J. R. Krenn. Coupling efficiency of light to surface plasmon polariton for single subwavelength holes in a gold film. *Optics Express*, 16(5):3420, 2008.

[128] Y. Jiang, S. Pillai, and M. A. Green. Grain boundary effects on the optical constants and Drude relaxation times of silver films. *Journal of Applied Physics*, 120(23), 2016.

[129] C. Sönnichsen, T. Franzl, T. Wilk, G. von Plessen, J. Feldmann, O. Wilson, and P. Mulvaney. Drastic reduction of plasmon damping in gold nanorods. *Physical Review Letters*, 88(7):774021–774024, 2002.

[130] P. T. Shen, S. W. Chu, Y. Sivan, C. W. Lin, H. Lin Liu, and C. W. Chang. Temperature- and roughness- dependent permittivity of annealed/unannealed gold films. *Optics Express*, 24(17):19254–19263, 2016.

[131] P. B. Johnson and R. W. Christy. Optical Constants of Noble Metals. *Physical Review B*, 6:1–10, 1972.

[132] N E Christensen and B O Seraphin. Relativistic Band Calculation and the Optical Properties of Gold. 8:1221–1226, 1970.

[133] A. Goulakov, K. Gao, and X. Jin. Direct waveguide light delivery to NFT for heat assisted magnetic recording, U.S. Patent 8,649,245 B2, Feb. 11 2014.

[134] R. Hong, W. Shao, W. Sun, C. Deng, C. Tao, and D. Zhang. The influence of dielectric environment on the localized surface plasmon resonance of silver-based composite thin films. *Optical Materials*, 83(May):212–219, 2018.

[135] N. K. Pathak, A. Ji, and R. P. Sharma. Tunable Properties of Surface Plasmon Resonances: The Influence of Core-Shell Thickness and Dielectric Environment. *Plasmonics*, 9(3):651–657, 2014.

[136] R. Yu, T. Shibayama, J. Ishioka, X. Meng, Y. Lei, and S. Watanabe. Plasmonic surface nanostructuring of Au-dots@SiO2 via laser-irradiation induced dewetting. *Nanotechnology*, 28(27), 2017.

[137] G. A. Al-Jumaily and S. M. Edlou. Optical properties of tantalum pentoxide coatings deposited using ion beam processes. *Thin Solid Films*, 209(2):223–229, 1992.

[138] Y. Li, S. Sanna, K. Norrman, D. V. Christensen, C. S. Pedersen, J. M. G. Lastra, V. Traulsen, M. L.and Esposito, and N. Pryds. Tuning the stoichiometry and electrical properties of tantalum oxide thin films. *Applied Surface Science*, 470(November 2018):1071–1074, 2019.

[139] J. Gosciniak, M. Mooney, M. Gubbins, and B. Corbett. Novel droplet near-field transducer for heat-assisted magnetic recording. *Nanophotonics*, 4(1):503–510, 2015.

[140] V. Holy, J. Kubena, I. Ohlidal, K. Lischka, and W. Plotz. X-ray reflection from rough layered systems. *Phys. Rev. B*, 47:15896–15903, Jun 1993.

[141] Thin-film thickness and density determination from x-ray reflectivity data using a conventional power diffractometer. *Thin Solid Films*, 230(2):99 – 101, 1993.

[142] G K M Thutupalli and S G Tomlin. The optical properties of amorphous and crystalline silicon. *Journal of Physics C: Solid State Physics*, 10(3):467–477, feb 1977.

[143] T. J. Bright, J. I. Watjen, Z. M. Zhang, C. Muratore, A. A. Voevodin, D. I. Koukis, D. B. Tanner, and D. J. Arenas. Infrared optical properties of amorphous and nanocrystalline Ta 2O5 thin films. *Journal of Applied Physics*, 114(8), 2013.

[144] Vladimir E. Bochenkov and Tatyana I. Shabatina. Chiral plasmonic biosensors. *Biosensors*, 8(4), 2018.

[145] M. Rodier, C. Keijzer, J. Milner, A. S. Karimullah, A. W. Roszak, L. D. Barron, N. Gadegaard, A. J. Lapthorn, and M. Kadodwala. Biomacromolecular charge chirality detected using chiral plasmonic nanostructures. *Nanoscale Horizons*, 2020.

[146] C. Kelly, R. Tullius, A. J. Lapthorn, N. Gadegaard, G. Cooke, L. D. Barron, A. S. Karimullah, V. M. Rotello, and M. Kadodwala. Chiral Plasmonic Fields Probe Structural Order of Biointerfaces. *Journal of the American Chemical Society*, 140(27):8509–8517, 2018.

[147] K. A. S. Immink. Compact disc story. *AES: Journal of the Audio Engineering Society*, 46(5):458–460, 462, 464, 1998.

[148] M. Born, E. Wolf, A. B. Bhatia, P. C. Clemmow, D. Gabor, A. R. Stokes, A. M. Taylor, P. A. Wayman, and W. L. Wilcock. *Principles of Optics: Electromagnetic Theory of Propagation, Interference and Diffraction of Light*. Cambridge University Press, 7 edition, 1999.

[149] F. Falcone, T. Lopetegi, M. A.G. Laso, J. D. Baena, J. Bonache, M. Beruete, R. Marques, F. Martín, and M. Sorolla. Babinet principle applied to the design of metasurfaces and metamaterials. *Physical Review Letters*, 93(19), 2004.

[150] Burcu Ögüt, Ralf Vogelgesang, Wilfried Sigle, Nahid Talebi, Christoph T. Koch, and Peter A. Van Aken. Hybridized metal slit eigenmodes as an illustration of Babinet's principle. *ACS Nano*, 5(8):6701–6706, 2011.

[151] Mario Hentschel, Thomas Weiss, Shahin Bagheri, and Harald Giessen. Babinet to the half: Coupling of solid and inverse plasmonic structures. *Nano Letters*, 13(9):4428–4433, 2013.

[152] M. Horák, V. Křápek, M. Hrtoň, A. Konečná, F. Ligmajer, M. Stöger-Pollach, T. Šamořil, A. Paták, Z. Édes, O. Metelka, J. Babocký, and T. Šikola. Limits of Babinet's principle for solid and hollow plasmonic antennas. *Scientific Reports*, 9(1):1–11, 2019.

[153] R. Mohammadi, M. Ochs, A. Andrieu-Brunsen, and N. Vogel. Effect of Asymmetry on Plasmon Hybridization and Sensing Capacities of Hole-Disk Arrays. *Journal of Physical Chemistry C*, 124(4):2609–2618, 2020.

[154] I. C. Bicket, E. P. Bellido, D. M. McRae, F. Lagugné-Labarthet, and G. A. Botton. Carving Plasmon Modes in Silver Sierpiński Fractals. 6(11):2974–2984, 2019.

[155] I. C. Bicket, E. P. Bellido, D. M. McRae, F. Lagugné-Labarthet, and G. A. Botton. Hierarchical Plasmon Resonances in Fractal Structures. *ACS Photonics*, 7(5):1246–1254, 2020.

[156] K.J. Zhang, B. Da, and Z.J. Ding. Effect of asymmetric morphology on coupling surface plasmon modes and generalized plasmon ruler. *Ultramicroscopy*, 185:55–64, 2018.

[157] C. Colliex, M. Kociak, and O. Stéphan. Electron Energy Loss Spectroscopy imaging of surface plasmons at the nanometer scale. *Ultramicroscopy*, 162:A1–A24, 2015.

[158] S. G. Smith. *Electrons as Probes of Chiral Materials*. PhD thesis, 11 2017.

[159] COMSOL Inc. www.comsol.com. COMSOL Multiphysics.